UNCONVENTIONAL SURFACE TREATMENTS
FOR
HIGH-STRENGTH STEELS

by

Kankanange Jagath Ananda Mawella
Hughes Hall
Cambridge

A dissertation submitted for the degree of Doctor of Philosophy in the University of Cambridge.

February 1983

Dedicated to

my brother Nihal

and

sister-in-law Anoja

PREFACE

This dissertation, which is submitted for the degree of Doctor of Philosophy in the University of Cambridge, describes research work carried out in the Department of Metallurgy and Materials Science under the supervision of Professor R.W.K. Honeycombe between October 1979 and October 1982. Except where due acknowledgement is made to previous work, this work is to the best of my knowledge original and has been performed without collaboration. No part of this dissertation has been or is currently being submitted for any other qualification at this or any other university. This dissertation contains less than sixty thousand words.

KJAMawella

K.J.A. Mawella

February 1983.

Summary

The possibility of altering the physical nature of the surface layer of high-strength steel by electron beam rapid quenching has been investigated. After initial studies on steel itself, changes in the nature of the surface layers were made using surface coatings of $Fe_{80}P_{13}C_7$ alloy, in order to induce the formation of metallic glass. Sputtering and plasma spraying methods and the combination of each process with electron beam rapid quenching have also been investigated as alternative means of producing amorphous layers.

The published work on rapid quenching with the main emphasis on the surface quenching processes is reviewed and the experimental techniques used are described. A theoretical heat flow analysis has also been carried out to investigate the influence of process parameters.

The structure of the electron beam quenched steel was examined and compared with the structures of the solid-state quenched steel and melt spun steel. The results indicate, that rapid quenching leads to a higher grain refinement and increases the amount of retained austenite, the solid solubility and the microhardness. The surface tension gradients, counteracted by the force of gravity lead to the formation of the ripples on the electron beam quenched surface. However, the surface roughness is reduced by an increase in traverse speed.

The electron beam rapid quenching process has been used to obtain metallic glass layers at the surface of $Fe_{80}P_{13}C_7$ alloy and a few other alloys. Amorphous layers of $Fe_{80}P_{13}C_7$ alloy were clad to the steel substrate by the application of the alloy powder followed by electron beam rapid quenching. The process parameters were controlled to obtain a minimal dilution at the interface between the substrate and the amorphous layer. The sputtering seems to be the best coating method used in this work to produce uniform amorphous layers on a substrate with a different composition. By sputtering, amorphous $Fe_{80}P_{13}C_7$ layers have been obtained on the steel substrates. Finally suggestions are made to indicate directions that possible future work could follow.

ACKNOWLEDGEMENTS

I would like to express my gratitude to my supervisor, Professor R.W.K. Honeycombe for the provision of laboratory facilities and for his advice and encouragement throughout the course of the project. I am grateful to Dr. H.K.D.H. Bhadeshia for stimulating discussions and for assistance in computer programming. Dr. R. Somekh deserves a special mention for kindly providing me with his expertise of sputtering. I would also like to mention Dr. P.R. Howell, with whom I had many helpful discussions in my first year. It is also a pleasure to acknowledge Mr. J. Reich for looking after the electron beam equipment and Mr. J. Leader for technical assistance.

I would like to thank the Procurement Executive, Royal Armament Research and Development Establishment of the Ministry of Defence for the provision of a maintenance grant for the period of this research work. Mr. J.A. Sheward of RARDE is acknowledged for arranging the erosion wear tests and micro analysis of Fe-P-C alloy coatings. I also wish to thank Mrs. T. Read for carefully typing this dissertation.

Finally, I wish to express my deep appreciation to my brother Nihal and sister-in-law Anoja for their continued interest in my education and for their loving support. Were it not for their dedicated care, I might never have had the opportunity to pursue my studies this far.

K.J.A. Mawella.

February 1983.

Hughes Hall

Cambridge.

CONTENTS

Chapter One Introduction

Chapter Two Rapid Quenching of Metals

Chapter Three Experimental materials and techniques

Chapter Four Theoretical study of heat flow in electron beam quenching

Chapter Five Electron beam rapid quenching of metals

CHAPTER 1

INTRODUCTION

There is considerable interest in the development of wear resistant coatings and surface treatments used in service (Zemel 1980) under a variety of different conditions. These conditions include dry sliding applications, abrasive wear conditions, lubricated environments and solid, liquid and gaseous erosion environments.

In this introductory chapter, the problem of wear in tubes under explosive conditions are summarised. Potential wear resistant methods, at present being investigated by other workers and the scope of the present research work, which is directed towards improvement of reduction in erosion wear in gun barrels of ultra high-strength steels will be described briefly.

1.1. Process of Wear by Erosion in Explosive Conditions

The deterioration of the inner surface of steel tubes under explosive conditions (e.g. gun barrels) is a phenomenon caused by the interactions of hot gases and the projectile with the inner surface of the tube. At each firing the propellant burns and develops a localized very high temperature and an extremely high pressure, which causes the projectile to move at the necessary high velocity. It is now known that at each firing the surface of the bore is exposed to (Glue et al. 1981);

1. High pressures of about 700MPa.
2. High surface temperatures of about 2500 - 3700K.
3. Severe mechanical stresses caused by high temperature and pressure, and associated phase changes in the ultra high-strength steel.
4. Chemical reaction with hot gases, produced by the combustion of the propellant.

5. Abrasive action of the unburnt powder or loosened erosion products of the gas-metal reaction.

The amount of wear of the inner surface, varies along the length of the tube according to the variation of the erosive conditions described above. Maximum erosion usually occurs at or near the commencement of rifling, as this area coincides with maximum exposure to the hot gases at high pressure. At each firing the hot gases of high velocity heat the surface in a very short time and remove the softened or molten material away from the surface of the bore. Alternating thermal stresses caused by the successive firings result in tensile rupture. During subsequent firings these cracks increase the tendency to remove material. The hot gases also soften the copper driving band of the shell and some copper particles may remain in cracks leading in time to intergranular penetration, accelerating crack propagation.

1.2. Potential Coating Processes.

A number of processes are being investigated to increase the wear resistance. It has been assumed that the thermal effects on the surface, dominate the wear process and there has been much effort to reduce the transfer of the heat input to the bore surface. Methods used include:

1. Use of wear reducing additions to the propellant.
2. Use of cooler propellant.
3. Application of liquid capsules to reduce the heat transfer to the surface.

Although these methods have received attention, the choice is limited by the constraints imposed due to the cyclindrical configuration and the performance requirements of the weapon. In recent years, efforts have been concentrated on improvements to the inner surface. Most of these approaches are based on the deposition of some material with a high melting point which is chemically inert with respect to the propellant gases. The methods which are at present under investigation by other workers are:

1. Electrodeposition.

Chromium electrodeposition is being investigated. It has been found that the coatings obtained by electrodeposition are highly stressed and that the resulting micro-cracks lead to spalling in service. The possibility of producing a coating with a reduced inherent stress is being investigated while deposition of other metals using fused salts, (Sethi 1978) such as boriding has also been examined.

2. Physical Vapour Deposition Methods.

Methods such as vacuum evaporation (Dugdale 1976), sputtering, ion plating (Teer 1978), and ion nitriding (Bell 1978) are used to apply coatings of a range of refractory metals (e.g. tungsten and titanium) as well as refractory carbides and nitrides. All these processes have their own advantages and disadvantages (Glue et al. 1981) in obtaining uniform coatings, adherence and resistance to the thermally erosive conditions during firing. Recently there have been many improvements in these processes but the work is still in progress.

3. Chemical Vapour Deposition

This method (Yee 1978) uses a volatile metallic compound and produces coatings on heated substrates. The deposition of tungsten has been studied by Bryant (1978) but the high temperatures required seem to cause problems such as tempering of the substrate.

4. Plasma Spraying

Plasma spraying using powder or wire guns is being tried to deposit refractory materials. The porous nature of the layer, which is a problem has yet to be overcome, possibly by plasma spraying in vacuum. This method as applied in the present work will be discussed in Chapter 6.

1.3. The Scope of Present Research

In the search of wear resistant improvements to the inner surfaces of cylinders subjected to explosive conditions, it was suggested that technique of rapid quenching be applied to the surfaces using electron beams. The present work adopts this approach and in addition, sputtering and plasma spraying methods have been investigated as alternative means of producing amorphous layers as wear resistant metallurgical coatings. The combination of sputtering or plasma spraying with electron beam surface melting was also studied in order to obtain amorphous layers.

The technique of rapid quenching using laser or electron beams, (Breinan et al. 1976) shows that interesting alloy structures and properties can be produced by this method. The structural changes, which occur by surface quenching, range from the refinement of the solidification micro-structure to the enhancement of solubility and the formation of metastable phases, and in the most extreme cases, complete suppression of crystallisation with the formation of metallic glasses. The production of amorphous layers at the surface, seems attractive as this extremely homogeneous metallurgical micro-structure is free of grain boundaries, and should lead to good mechanical strength and wear resistant properties.

Chapter 2 reviews the rapid solidification processing and includes previous work on both amorphous and crystalline structures. The interest in the production of amorphous layers on steel substrates has led to the processes of plasma spraying and sputtering, so brief descriptions of these methods are also included in the same chapter. Chapter 3 describes the experimental details of the electron beam rapid quenching process. It also includes the specimen preparation techniques for optical, scanning and electron microscopy, energy dispersive X-ray analysis and micro-hardness measurements. A discussion of the theory of heat flow in materials subjected to a moving point heat source, effects of beam power and speed on the melt depth, melt width and the cooling rate and finally a comparison of experimental and theoretical results to justify the application of this theory are included in chapter 4. In chapter 5, electron beam surface melting of ultra high-strength alloy, $Fe_{80}P_{13}C_7$ alloy and other alloys is investigated by structural and surface morphology studies. Similarities of the rapidly quenched micro-structure of the same steel obtained by another rapid quenching method, melt spinning, are also described and the products of both these rapidly quenched methods are compared with the conventionally solid state quenched steel. The results of the applications of surface layers on steel, by cladding and alloying are presented and discussed in chapter 6. Microhardnesses of surface layers are discussed in both chapter 5 and 6, while a practical assessment of the surface layers by the results of thermal erosion experiments are included in chapter 6. Chapter 7 contains the main conclusions and indicates directions that possible future work could follow.

CHAPTER 2

2. Rapid Quenching of Metals

2.1. Introduction

The term quenching is usually defined as a process of cooling a metal or an alloy from a higher temperature by contact with liquids, gases or solids, with the main aim of cooling the material at a high enough rate, so the phases stable at higher temperatures are either partially retained, transformed into non-equilibrium phases or both. In the quenching of solid alloys, it is expected to cross the phases boundaries fast enough to completely or to at least partially avoid the equilibrium reactions from taking place. Basically, solid state diffusional transformations are suppressed. The technique of quenching metals and alloys at non-equilibrium cooling rates has been used in practice for a long time, to increase the strength of materials. Usual cooling rates achieved by quenching processes are of the order $10^4 Ks^{-1}$ or less, with the exception of the cooling rate of $10^5 Ks^{-1}$ which Mori and co-workers (1962) had achieved, for quenching very fine gold wires in brine.

Quenching from the liquid state is usually carried out with the same aim, but in this case the critical phase boundaries are the liquidus and the solidus of the particular alloy. The configuration of the atoms in a liquid is much different from that of a solid, and extensive re-arrangement of atoms must take place during the solidification from the liquid. There is a greater mobility of atoms in the liquid state than that in the solid state, therefore the rate of cooling required in quenching from the liquid state necessitates faster quench rates, compared with those necessary to suppress solid state diffusional transformations. Therefore rapid quenching techniques; more effective techniques to increase the cooling rates, which are based on cooling from the liquid by conduction as well as the techniques based on quenching from the vapour phase have been developed. By these methods, crystallization of liquid alloys are being modified and in some cases completely suppressed.

Historically, one may track the interest in production of rapidly quenched materials to the problems associated with alloy segregation during conventional processing of castings and ingots. The advantages of rapid quenching were first recognised by Falkenhagen and Hoffmann (1952), who used a refrigerated copper mould to rapidly quench aluminium based alloys, but there was not much work carried out on rapid quenching until Duwez, Willens and Klement (1960a) reported that a complete series of solid solutions were obtained in the usually binary eutectic Ag-Cu system. Their motive for achieving extreme rates of cooling, in liquid alloys, was to prevent the phase separation in binary alloy systems, which according to the Hume-Rothery rules, should form a complete series of solid solutions and yet an eutectic system was found under equilibrium conditions. Their extra-ordinary results were followed by a new crystalline, non-equilibrium phase in the Ag-Ge system (Duwez, Willens and Klement 1960b) and soon after Klement et al (1960) reported the achievement of a non-crystalline phase in Au-Si system. Since the initial work of Duwez, a large number of resourceful investigations of the rapid quenching process have ensued. As in many other fields, practice has preceded theory. The observation of unusual fine structures, increased solid solubility of alloying elements, non equilibrium phases and non-crystalline structures has stimulated the interests of scientists to develop theories explaining these phenomena.

2.2. Metallic Glass

2.2.1. Formation

On cooling below its melting temperature, T_m, a liquid either crystallizes or forms a glass, depending on the cooling rate. If crystallization occurs, properties such as viscosity, volume and internal energy change discontinuously, but if the crystallization can be bypassed these changes occur continuously, the liquid eventually solidifying into a glassy state. (Fig.2.1). Since the liquid has a higher free energy than its corresponding crystalline state at temperatures below T_m, there is a capacity for rapid crystal growth below this equilibrium temperature. Since nucleation becomes thermodynamically most favourable during further cooling, the crystallization rate exhibits a maximum. However if the cooling rate is very rapid for crystallization to be avoided, the liquid solidifies into a glass, within a narrow temperature range interval, which is known as the glass transition temperature, T_g. At T_g, the viscosity of the undercooled liquid increases up to about 10^{13} poise, and at such a high viscosity, atomic motions are much reduced, with no essential change in spatial atomic configuration occurring during the transition. Thus the formation of a glass occurs at a high enough cooling rate, which prevents detectable crystallization, so the glass formation does not depend only on the cooling rate but also on the kinetics of crystallization.

In the search for kinetic conditions which enhance the ease of glass formation, a simple parameter which is useful in expressing the glass forming tendency (GFT) has been found. Considering the conditions which have to be fulfilled by the crystal nucleation frequency and the cooling rate of the liquid for crystallization to be bypassed, Turnbull (1969) showed that the glass forming tendency should increase with increasing "reduced glass temperature" (T_{rg}), defined as the ratio T_g/T_m. It is in the temperature range T_m-T_g that crystallization can occur during cooling, so that a minimisation of this range should increase the chance of bypassing crystallization.

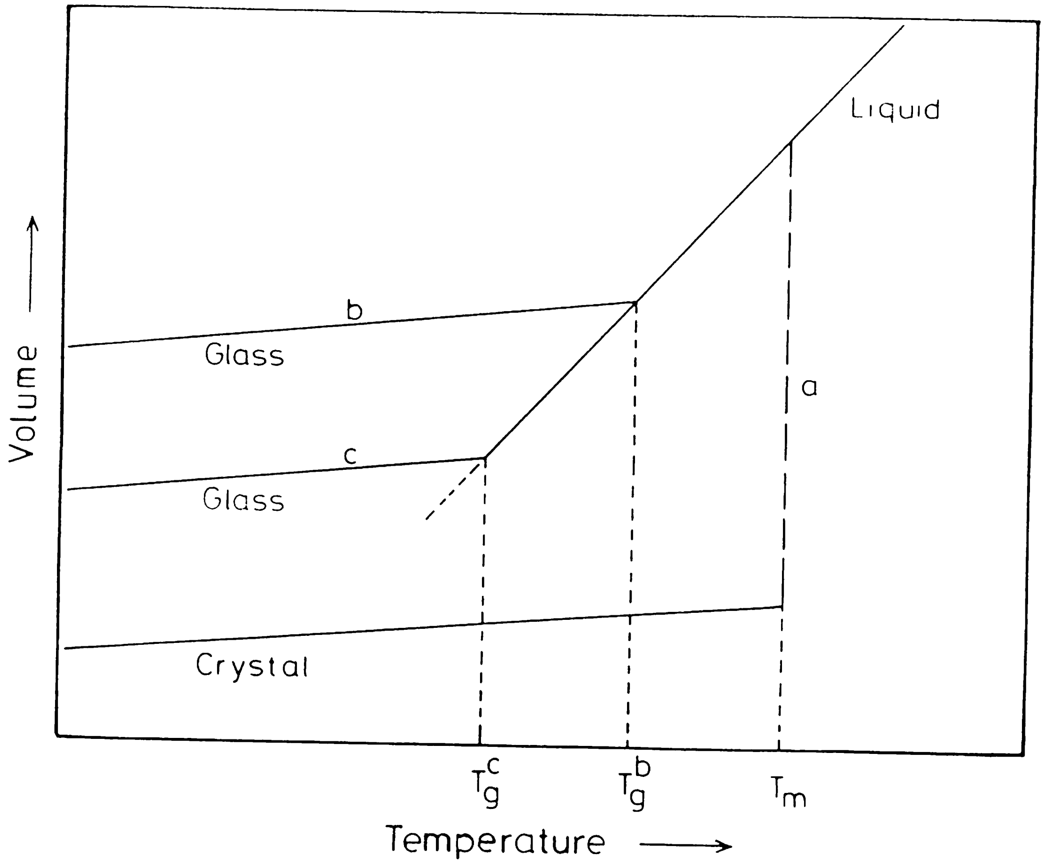

Fig. 2.1. Schematic representation of the variation of volume with temperature in a glass forming system. Faster cooling rate at b gives a higher Tg. (after Jones 1971).

Fox and Flory (1950) attributed the glass transition to the falling of the free volume of the material below some critical value. Considering the free volume again and based on the idea that molecular transport occurs by the movement of molecules into voids with a size greater than some critical value, Cohen and Turnbull (1959) predicted that all liquids if sufficiently undercooled would undergo a transition to glassy state. Theoretically these predictions may be true but practically it is not possible to obtain a metallic glass of every desired alloy composition, at least with the level of quenching rates achieved at present. However, since the original invention of metallic glass by Klement et al (1960), metallic glasses of a large number of suitable alloy compositions have been formed. Those compositions fall into three main categories.

A) Transition metals (Fe, Ni etc) or noble metals (Pd, Ag etc) based alloys containing about 15-25 at % metalloids.

B) Alloys between the late transition metals (Fe, Co, Ni, Pd etc) with early transition metals (Ti, Zr, Nb etc.).

C) Alloys based on group 2a metals (Mg Ca, Sr) generally, with 2b solutes (Zn etc.)

Metallic glasses of category A have attractive combinations of properties and have received the most attention to date, due to their higher technological potential. Alloys used in the present work also fall within this category. Most of the metallic glasses have eutectic or near eutectic compositions since the critical cooling rate is at a minimum at eutectic compositions. This effect can be easily described with reference to the reduced glass temperature. The lower the value of T_m and higher the T_g, the larger is T_{rg}, which increases the glass forming tendency. In the transition metal-metalloid alloys, at deep eutectic compositions, T_m is at its lowest but T_g remains high, due to the fact that T_g generally varies relatively slowly with composition, (Lewis and Davies 1977, Ray et al 1977) resulting in a higher glass forming tendency.

2.2.2. Mechanical Properties

Metallic glasses exhibit an interesting combination of mechanical properties. Most of the mechanical property measurements published to date have been carried out on ribbons produced by melt spinning. The ratio between the fracture stress (σ_f) and Young's modulus (E), E/σ_f is found to be ∿ 50 approaching the theoretical maximum. (Masumoto and Maddin 1975). Iron based glasses have a σ_f of about 3.5 GNm^{-2} (Davies et al. 1975), which is higher than that of the conventional highest strength steel; piano wire. This exceptionally high strength seems to be associated with localised deformation. Leamy et al (1972) found that glass metals deformed in tension, initially undergo localised shear along the direction of maximum shear stress. Thus plastic flow seems to occur in the form of highly localised shear deformation, the samples finally fracturing by decohesion within the locally deformed material leaving a vein pattern of ridges on the fracture surface (e.g. Davies and Kavesh 1975).

An effective measure of the intrinsic strength of a material is also given by its microhardness. Very high values of hardness, in metallic glasses have been reported. As predicted by the two dimensional slip line field analysis of Hill (1967) for rigid plastic materials, the yield stress (σ_y) of metallic glass has been found to scale with the microhardness (Davies 1975). A hardness to yield strength ratio of ∿3 was reported by Davies (1975). A direct proportionality between hardness and the shear modulus (G) for metal-metalloid glasses was also found by Chou et al. (1977). Naka et al. (1975) attributed the properties such as hardness to bonding between the transition metals and metalloids. They suggested that the bonds were formed by the overlap of s-p hybrid orbitals of metalloids and s-p-d orbitals of transition metals.

The increase of elements such as Cu and Ni, which would increase the d-electron concentration would reduce the hardness. It should also be noted that the effect of metal atoms on the properties of iron based metal-metalloid glasses are influenced by the type of metalloids present. For example, the substitution of chromium or vanadium for iron in $Fe_{80}P_{13}C_7$ glass resulted in an increase in hardness, whereas replacement of iron by cobalt lowered its hardness. (Naka et al. 1975). In comparison, when boron was the only metalloid present (in $Fe_{80}B_{20}$ glass), replacement of chromium, vanadium or cobalt by iron did not alter the hardness at all. (Ray and Tanner 1980). Naka et al. also showed that an increase in the metalloid content increased the micro hardness. Working on binary metallic glasses containing boron, Köster and Hillenbrand (1980) also showed this effect. This increase in hardness may be caused by the increase in metal-metalloid bonds and the decrease in free volume (Johnson and Williams 1979) due to the formation of stable phases (e.g. Co_2B in $Co_{80}B_{20}$ glass).

The behaviour of amorphous metals under cyclic loading have shown the fatigue stress (s) vs number of cycles (N) curves to be of the same general type as for crystalline metals (Masumoto and Maddin 1975). Fatigue fracture occurs at stress levels well below the maximum yield stress but the fatigue stresses may attain considerably high levels due to the inherently higher strength of amorphous metals.

Only a few workers have reported investigations of the behaviour of metallic glasses under service conditions, similar to those which may arise in potential applications. Although the materials were in the form of ribbons, Amuzu (1980) measured the coefficient of friction (μ) of some metallic glasses. These values were found to be in the range of 0.014–0.017. Since $\mu = \tau/p_o$, where τ is the shear strength and p_o is the effective main yield pressure, the coefficient of friction is related to the bulk properties of the material. Values of τ and p_o have been computed from hardness and yield strength values reported by Davies (1978) and it was observed that the measured values of coefficients of friction are a factor of about 30 smaller than the computed values. However metallic glasses turn out to be very low friction materials and when combined with their high resistance to wear, may find useful applications. Boswell (1979) measured the relative wear resistance of amorphous and partially crystalline specimens of liquid quenched Pd-Cu-Si alloy. Pin-on-disc wear tests were carried out on rods of metallic glasses, before and after heat treatments. The results showed that on heating, the wear rate initially decreased during the first crystallization stage MS-1, where the formation of small closely spaced crystals of a fcc phase occurs but the wear rate increased significantly during the subsequent MS- II crystallization stage. The decrease in the wear resistance during the second stage is attributed to easy crack nucleation within the brittle crystalline phases and to the subsequent crack propagation.

2.3. Fabrication Methods

In an effort to obtain higher cooling rates, Falkenhagen and Hoffmann (1952) devised a technique of heat removal by conduction. A molten aluminium based alloy was sucked into a refrigerated copper mould in order to chill it against the mould surface kept at liquid nitrogen temperature. After a gap of a few years Duwezs et al.'s invention (1960a, 1960b) of propelling a small liquid droplet onto the inner surface of a rotating copper cylinder, re-opened the field of rapid quenching of liquid metals by conduction. Since then, many rapid quenching methods have been developed, satisfying the following conditions, to obtain the full advantage of the principles of rapid quenching.

1) A good thermal contact between the liquid and the substrate during solidification and subsequent solid state cooling.

2) The liquid layer should be relatively thin. This is based on the assumption that non-equilibrium phases are likely to occur during the solidification of a material, if the solid-liquid interface can be forced to move at a sufficiently high velocity.

3) The time between the initial contact of liquid and substrate and the end of solidification must be as short as possible. This takes into account the fact that nucleation will start as soon as the liquid makes contact with the substrate and excessive time spent between the first contact and the complete solidification is likely to induce the growth of equilibrium phases.

Methods of rapid quenching by conduction can be broadly classified as follows.

1. Static quenching of droplets or vapour by a solid substrate.
2. Continuous quenching of liquid metal by a moving substrate.
3. In situ surface quenching process.

Since the present work is directly involved with the in situ surface melting process, that method will be fully reviewed but the other methods will be described only briefly.

2.3.1. Static Quenching of Droplets or Vapour by a Solid Substrate

a. Splat Quenching.

Splat quenching by a gun technique was first described by Duwez and Willens (1963). In this process, a droplet of molten metal is ejected with a high speed onto a stationary copper target which is bent in a circular form. The globule is aimed at a glancing angle to the target so the molten material is given a radial acceleration by the target which keeps it in good thermal contact with copper. Measuring the rate of cooling is a difficult problem due to the necessarily short time available during the quench. Using an analysis, which took into account the shape and the size of the splat, velocity and the heat transfer coefficient, Predecki et al. (1965) have calculated average cooling rates of 1.5 - 3.0 x 10^7 °C/s for a gold alloy containing 14 at.% antimony.

The splats obtained by gun technique were uneven and contained many holes. This non-uniformity caused problems in measuring mechanical properties although being ideal for TEM studies. In order to improve the morphology, Pietrokowasky (1963) developed the piston and anvil technique. The rapid spreading of the liquid globule against the surface of a metal having a high thermal conductivity is the basic principle, but in this case the globule is squeezed between two heat conducting surfaces brought into contact very rapidly. Thus actual quenching is achieved by allowing a liquid globule to fall in between a fixed anvil and a fast moving piston activated by high pressure. Since Pietrokowasky's invention, various modifications have been made to this technique, such as the use of electromagnetic drive instead of gas pressure to move the piston (Harbur et al. 1966) and the use of two pistons instead of a piston and an anvil (Harbur et al. 1969). Splats obtained by this method were quite uniform in thickness. Harbur et al. reported experimentally determined average cooling rates using iron and aluminium anvil plates as an intrinsic thermocouple which were connected to a storage oscilloscope. After the conversion of electromotive force to temperatures, they obtained cooling rates, in the range of 6.9 x 10^5 to 1.2 x 10^6 °C per second.

b) Plasma Spraying

Rapid quenching of liquid droplets using a plasma jet has been described by Moss et al. (1964). The powder of the alloy to be quenched has to be pre-prepared and is introduced into an inert gas plasma jet and the molten droplets moving at a high speed are rapidly quenched upon the impingement on a cold substrate. Moss et al. have reported non-equilibrium phases found in plasma sprayed Mo-Ru layers. This technique is currently used to obtain reasonably thick films of metals and alloys (Cahn 1977). This method as applied to present work will be discussed in chapter 6.

c) Sputter Deposition

Sputter deposition is another way of achieving fast quenching. In this process, an electric discharge is generated between two properly cleaned metals or alloys, the coating material being the cathode. Due to the bombardment of positive ions, atoms are ejected (sputtered) from the cathode, and are condensed on the other metal (substrate). Usually the substrate is kept cold. As soon as the atoms are deposited on the substrate, they are rapidly cooled. As long as the atoms striking the substrates have sufficiently low energy, a metallic glass will be formed. In d.c. sputtering a high gas pressure (∿0.1 Torr) is required to avoid arcs which can be present between the electrodes. At relatively high gas pressures sputtered particles collide with gas molecules resulting in a reduction in the deposition rate to just a few angstroms per second. Due to these colisions some energy of the sputter particles is transferred to gas molecules (thermalisation). By the time condensation occurs, the sputter particles may have substantially reduced momentum. In magnetron sputtering due to the crossed electrical and magnetic fields, electrons follow a curved path, resulting in an increase in the sputtered rate. Many workers have obtained rapidly quenched crystalline layers by direct current or magnetron sputtering (e.g. Hoffmann and Thornton 1977), but only a few have reported the formation of glassy layers (e.g. Allen et al 1976). A main advantage of sputter deposition is that this process can be used for coating specimens with complex geometries (Gibson 1981).

2.3.2. Continuous Quenching of Liquid Metal by a Moving Substrate

The technique of continuous wire production using free jet melt spinning was first reported by Pond (1961). Molten metal was ejected through an orifice in a crucible and the rapid heat removal was by the surrounding fluid medium. Using this technique with a refrigerated salt solution as the quenching medium, Kavesh (1978) obtained a cooling rate of about 10^4 K s^{-1}. The chill block melt spinning was based on the same principle but uses a solid substrate to remove heat. Originally this method was prepared by Strange and Pym (1908) but much later the production of wire by Pond (1961) re-started the interest in the continuous production of metal wires and ribbons. Bedell (1975) modified the process by ejecting the molten liquid onto the perimeter of a rotating copper disc. A schematic diagram of the melt spinning apparatus is shown in Fig.2.2. The spinning disc drags the molten metal onto the perimeter. Due to the rapid transfer of heat from the molten liquid to the disc, a rapidly quenched ribbon is produced. This technique,normally known as melt spinning has been used extensively to produce crystalline and amorphous ribbons and has now become the standard method of rapid quenching. This method was used in the present work to produce rapidly quenched crystalline and amorphouse ribbons.

2.3.3. In-Situ Surface Quenching Process

This technique involves the use of power available from a laser or an electron beam in conjunction with a short beam-specimen inter-

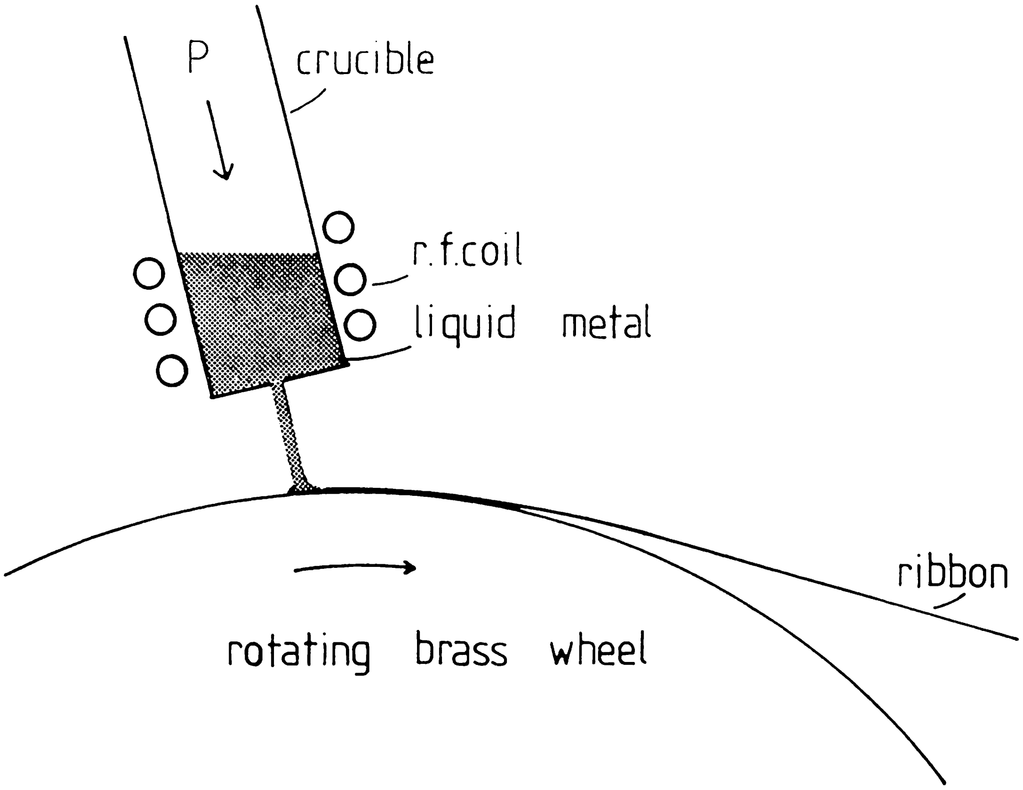

Fig. 2.2. Schematic diagram of the melt spinning apparatus.

action times to confine the thermal effects of the beam to a shallow surface layer of a material. The beam is pulsed or traversed on the surface of a material with a power level, which would give the required depth. Rapid surface melting occurs in a short time during which a negligible amount of thermal energy can be conducted into the bulk of the specimen, producing a steep temperature gradient between the bulk solid and the liquid layer. Hence rapid solidification follows and subsequent solid state cooling is also very fast. Both electron and laser beams can be used. Due to the high electron beam to material energy transfer efficiency, low power electron beams (relative to laser beams) can be used to melt the surfaces; on the other hand electron beam systems require a high vacuum environment. Laser systems are subject to some energy coupling in-efficiency, unless the reflectivity of the surface is reduced. In most cases, coatings have been used to increase the absorbtion of laser power. This rapid quenching process will be revived in detail in the next section.

2.4. Electron or Laser Beam Surface Quenching.

2.4.1. Progress of Surface Quenching Technique.

Techniques of producing rapidly solidified metals and alloys have made a good progress since the original invention. The advent of different kinds of melt spinning methods has improved both the controllability and reproducibility of the process. However all the above quenching techniques led to the formation of very thin ribbons, splats or powder material. The main limitation of these techniques, as far as maximum quench rate capability is concerned, is that heat flow from the liquid metal during solidification involves energy transfer across an interface layer at the contact surface with the heat sink. Since actual contact of liquid metal with the substrate occurs at isolated points over the nominal contact area, overall heat transfer is dominated by not only direct conduction from the liquid metal to substrate, but also by radiation across the intervening gaps, in which case a slower cooling rate can result. More intimate contact between the melt and the substrate could lead to higher cooling rates.

A method in which melting and solidification of a substrate in in-situ conditions was first reported by Jones (1969), subjecting an Al-Fe alloy to short high energy pulses by means of capa~~s~~citance discharge and laser beams in a method he described as surface pool freezing. This technique was meant to eliminate the effects dependent on the pressure applied in splat cooling, while retaining the comparable cooling rate by conduction. The control of power in melting these materials was not successful, resulting in the evaporation of a considerable amount of the material, but thin rapidly solidified areas were certainly obtained. (Fig.2.3). Phases obtained in this solidified region have also been found in the rapidly solidified splats of the same material. In fact in some earlier work Brekhovskhki and co-workers (1968) reported surface melting of steel by laser irradiation. Cavities were formed when high intensity beams were used and the cavity walls were relatively hardened. Microstructural details were not given but cooling rates of about 10^6 °C/sec were reported. Elliott, Gagliano and Krauss (1972) also reported results of a single pulse laser melt quenching experiment. A cooling rate of 3.7×10^6 °C s^{-1} was determined for a laser melted Al-4.5% Cu alloy by utilising an established relationship (Matyja et al. 1968) between dendrite spacing and cooling rate. In another study carried out by Elliott and co-workers (1973) to test the capability of laser melt quenching to retain non-equilibrium phases in the Ag-Cu system, it was found that within the laser melted area, the equilibrium structure of Ag-Cu alloys underwent complete melting with a suppression of

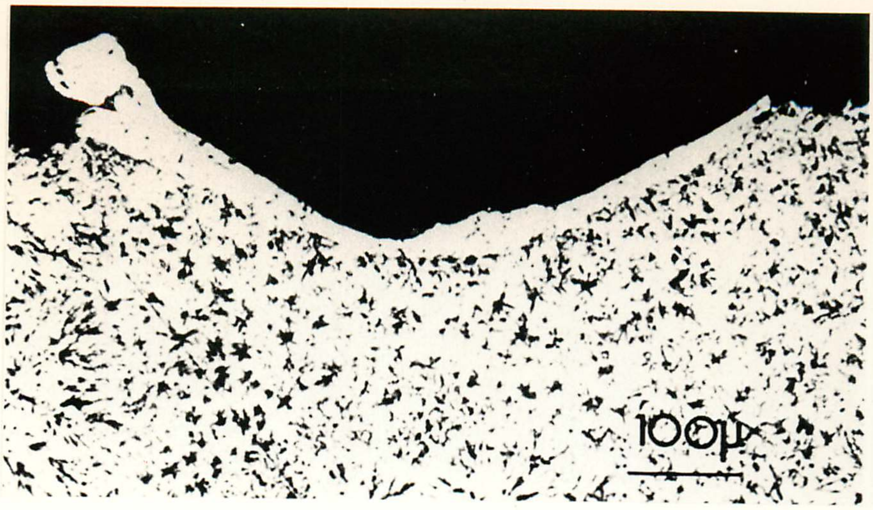

Fig.2.3. Light micrograph of a rapidly solidified pool of Al - 8%Fe alloy produced by laser. (After Jones 1969)

Fig. 2.4. Cross section of a laser irradiated silver - 21 at % germanium alloy (after Laridjani et al 1972)

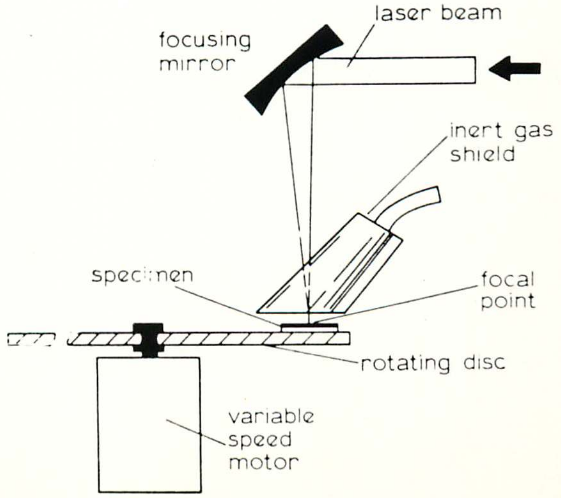

Fig.2.5. Schematic diagram of the surface melting of specimens using a laser beam. (After Breinan et al 1976.)

equilibrium microstructure upon solidification. It led to the formation of metastable solid solution phase (in addition to the non-equlibrium phases) and has caused a threefold increase in hardness within a well defined micro-region. Laridjani and co-workers (1972) studied Ag-21%Ge alloys subjected to high energy laser pulses. This resulted in the formation of craters (Fig.2.4) and X-ray analysis showed the formation of a hcp phase in the irradiated zone, the lattice parameters being in close agreement with the values given by Klement (1961) for metastable phases obtained by splat quenching the same material.

Although these workers have published their work on surface quenching, it seems that the work has not been continued, probably because the high energy pulses used in rapid quenching also lead to cavitation problems. In a study of the metallurgical response of some steels subjected to laser heating, Harth et al. (1976) traversed a laser beam on the surface of the specimen. The surface of the steel was coated with manganese phosphate to aid the absorbtion of energy from the beam but this did not prove successful due to pre-melting and the removal of the coating. The rapidly solidified areas of AISI 1045 steel consisted largely of martensite but in the melted region of 0-1 steel (0.9C, 1.0Mn, 0.5Cr, 0.5W) carbides were also present in addition to martensite. No non-equilibrium phases were found. In the same year Breinan and co-workers (1976) developed a technique of surface melting which involved the rapid traversing of the surface of a material with a laser beam focussed to a suitable power density. The apparatus used by them is shown in Fig.2.5. The specimens were placed on a rotating disc and were irradiated by a focussed laser beam of a high power density (in the range 10^4-10^7 W/cm^2). This procedure usually yields a thin rapidly quenched layer at the surface. There is practically no hindrance to heat transfer between the molten pool and the solid. Using the results of an analog computation (Cohen 1967), average quench rates in excess of 10^8 °C/ s seem to have been achieved with melt thicknesses in the 1-10 µm range.

An interface heat transfer coefficient of infinity only occurs at ideal thermal contact between the liquid metal and the solid substrate and is typical in electron or laser beam surface melting process. Using computerised calculations for a one dimensional heat flow and assuming ideal cooling of splats, Ruhl (1967) obtained average cooling rates in the order of 10^7 and 10^9 °C /s for splat thicknesses of 10 µm and 1 µm respectively. Thus it can be seen that whatever the method of calculation is, very high cooling rates can be obtained in ideal cooling. These high cooling rates can give rise to supercoolings of higher degrees prior to solidification resulting in non-equilibrium alloy phases and extended solid solubilities.

Breinan and co-workers (1976) used a slightly off eutectic base metal, an alloy of Pd-4.2 wt%. Cu - 5.1 wt%. Si, which is usually crystalline. By laser beam process, the melted area was re-solidified as a homogeneous single phase region. The amorphous nature of this melted region was confirmed by the diffuse ring pattern observed in electron diffraction, the veiny nature of the fracture surfaces revealed by SEM and the localised flow of material (intensive shear bands) surrounding the micro-hardness indentations. In another laser melted sample of an alloy of Ni with Co, Cr, Mo and B, the treated area was made homogeneous and appeared featureless, as compared with the multiphase inhomogeneous base alloy. Micro-hardness (DPH) values up to 1400 diamond pyramid hardness in the melted region were achieved compared with that of 650 DPH of the base alloy.

All the experiments have not resulted in metallic glass layers at the surface. As described earlier, the formation of metallic glass is not only based on the cooling rate but also on the composition. Breinan and co - workers have shown that in an alloy of Co, Ta and C, the rapidly quenched area had become a uniformly dendritic region with carbides distributed in a fine equiaxed network. Furthermore electron microscopy revealed two morphologies; a dendritic solid solution and a fine eutectic. The interdendritic regions contained homogeneous single phase solid solutions supersaturated with carbides. Experiments on a steel specimen, involving two superimposed beam passes also were reported by Breinan and co -workers. The initial pass was used to homogenise the surface layer composition and the second pass to obtain the real effects of rapid quenching. After the second pass, the rapidly quenched area showed a microhardness of 100 DPH more than that of the base metal and of about 30 DPH more than the microhardness of the area melted by the first pass.

After these initial successes of the surface melting process, the use of laser beams as well as electron beams in the processing of materials for the control of microstructure has spread widely.

Generally, the most of the power in a laser beam is absorbed at the surface of the material upon which it is incident. i.e. it is not transmitted, but the power in an electron beam is absorbed both at and beneath the surface. Therefore for the same power employed the transient temperature response of a material is different depending on whether the power came from a laser or an electron beam. Using a semi-infinite plate model presented by Greenwald et al. (1979), Strutt (1980) compared the theoretical values of the maximum melt depths with experimental values obtained by both laser and electron beams. On the basis of this comparison between prediction and observation, the energy coupling between the beam and the material is about 55% efficient for the electron beams and about 5.5%, for the

laser beams. Thus the surface melting efficiency of electron beams is about ten times greater than that of a laser beam. Greenwald (1975) compared the temperature profiles in a material, due to heating by both kinds of beams. An important conclusion was that if the electron energies are low enough, cooling rates in the material surface melted by an electron beam would be similar to those in a laser melted material.

On the basis of these discoveries, the use of electron beam surface quenching to achieve high cooling rates have been explored by a few workers (Bergmann and Mordike 1980, Strutt 1981, Ruff and Ives 1982). Since electron beam technology is well established, the required equipment is readily available or only a little effort is necessary for the modifications needed.

2,4.2. Crystalline Structures by Surface Quenching.

Except for the work of Breinan et al.(1976), most of the earlier studies of laser or electron beam quenching were on the production of crystalline structures. Surface melting of aluminium and titanium alloys was carried out by Weinmann and Kim (1977). Massive solidification cracks and surface porosity have been observed in commercial aluminium alloys but not in pure aluminium. The examination of fracture surfaces showed that the specimens fractured along an interfacial void line and through the surface solidification cracks. Gas seemed to have been expelled from the melt interface towards the free surface and has escaped through the surface pores. The micro-hardness of the commercial alloys had dropped slightly at the interface, probably due to the large amount of voids present, but Al-4%wt. Fe alloy specimens showed an increase of about

40 kg/ mm^2 after rapid quenching. A Ti alloy (Ti- 6Al - 2Cd - 1 Ta - 0.8Mo wt%), produced uncracked re-solidified regions. X-ray diffraction technique and TEM showed that the melt had completely transformed to α martensite.

Beck and co-workers (1977) investigated the microstructure produced by scanning a laser beam across single crystals of nickel base super-alloys. The microstructural features were found to vary with the crystal orientation, incident power and the scanning rate. Over a wide range of conditions, resolidification involved the growth of dendrites, which has resulted in the formation of surface grains. It was suggested that the surface grains were nucleated at surface ripples. These ripples were believed to be a result of the overflowing of the melt pool. Anthony and Cline (1977) studied these surface ripples and this will be discussed later in chapter 5.

The microstructures of nickel base superalloys were also studied by Breinan et al. (1976) and Narasimhan et al. (1979). They suggested that regrowth during solidification was epitaxial. Narasimhan et al (1979) showed that the solidification may involve the growth of misoriented grains along the centre line and near the surface of the melted region. A microstructural investigation into rapid solidification of Al-4.5% wt. Cu (Munitz 1980) also showed that the melted regions resolidify epitaxially onto the unmelted crystalline substrate. Numerous diffraction patterns taken from the melted area and regions near and far from the interface were identical, suggesting that all three regions had the same orientation, implying epitaxial growth.

Observation of laser melted Zircaloy - 4 (1.7Sn, 0.3Fe, 0.14Cr, Bal. Zr) (Snow and Breinan 1979) revealed that there was no crack formation over the entire range of parameters used (3-6 kW power with

14-127 cm s^{-1} speeds). Very fine martensite laths were found in the melted regions. Both the martensitic packet size and plate length decreased with increasing cooling rate. In the microstructures produced by slow traversing speeds, a few long internally twinned plates were infrequently observed but more rapidly solidified structures contained very fine ($\sim$ 0.3μm average width) internally twinned martensite laths. Whatever the method of production was, quite a few investigations revealed the presence of internally twinned martensite plates in rapidly quenched microstructures and this phenomenon will be discussed later in section 5.1.4.2.

There are quite a number of reported investigations of rapidly solidified layers of iron-based alloys produced by surface quenching technique. Tool steels have been subjected to laser beam quenching by several workers. Tuli and co-workers (1977) and Strutt and co-workers (1979) carried out microstructural analyses on tool steels. Working on alloy M-2 (0.85C, 0.25Mn, 0.3Si, 0.03P, 0.3S, 4.2Cr, 1.9V 5.0Mo, 6.3 W and balance Fe) they found out that the microstructure consisted of both δ-ferrite and austenite with residual amounts of carbides. At the maximum melt depth, the morphology in a narrow area resembled that of the chilled zone of a solidifying ingot on a very fine scale. The relatively long columnar dendrites grew into the melt and finally an equiaxed cellular structure was found in the upper melt region. A predominant feature is the formation of γ by peritectic reaction of δ-ferrite with liquid. The extent to which the reaction proceeds depends upon the position within the melted zone. The region near the surface was predominantly δ-ferrite. The fine elongated dendrites in the austenitic lower melt zone presumably formed as δ-ferrite which then transformed to austenite due

to a relatively slow velocity of the liquid solid interface. (Greenwald 1977). In the lower melt region, the peritectic reaction δ+ liquid→ γ + carbide, has gone to completion. The equiaxed structure in the upper zone formed by nucleation and growth of δ -ferrite, which later reacted with the carbon enriched liquid to form austenite and carbides but the very high cooling rate greatly reduced the re-distribution of the alloying elements by diffusion so this peritectic reaction was stopped.

The results of Tuli et al. and Strutt et al. are very similar to the observations of Sare and Honeycombe (1978) on splat quenching studies of tool steels and Fe-10%Mo-0.5%C alloy. They reported that the microstructure consisted of a carbide dispersion in a matrix with varying properties of a fcc phase and a bcc phase with no detectable tetragonality.

Steen and Courtney (1979) described the microstructure of laser melted En8 (0.36C, 0.22Si, 0.58Mn, 0.08Cr, 0.25Ni, 0.5Cu) steel. Two different metallurgical microstructures were observed depending on the process speed. At lower speeds microstructure of the melted En8 steel was mainly martensitic.However the material near the heat affected zone consisted of pro-eutectoid ferrite and martensite, which demonstrated the fact that the material in this region had been heated above the eutectoid temperature but not into the austenite single-phase field. In high speed runs, the microstructure consisted of a large amount of a dark etching phase, which was thought to be a different morphology of austenite which had turned into martensite. It is possible that the pro-eutectoid ferrite transformed to austenite by a diffusionless shear transformation, since the diffusion of carbon was limited by a higher freezing rate.

More recently Molian (1981) carried out a microstructural study of laser melted AISI 4340 steel (0.4C, 0.69Mn, 0.32Si, 0.69Cr, 1.87Ni, 0.2Mo). The microstructure consisted of packets of parallel laths and internally twinned plate martensites. The presence of twinned martensite plates in rapidly quenched steels and other ferrous alloys were earlier reported by Inokuti and Cantor (1976) and Sare and Honeycombe (1978), although the methods used were different. Molian found substantial amounts of thin films of retained austenite in the laser treated steel and the comparison with the conventionally heat treated steel showed an enhancement of retained austenite in the rapidly quenched structures. Surface treated regions were also found to contain a homogenous dispersion of cementite particles, both at the lath boundaries and along the internal twins. The formation of twinned martensites (Messler et al. 1969, Thomas 1971) and the difference in the amount of retained austenite for different heat treatments (Webster 1968, Donachie and Ansell 1975) have been attributed to various causes by different investigators and will be discussed in detail in chapter five, with the experimental results of the present work.

2.4.3. Amorphous Structures by Surface Quenching.

As described earlier the main advantage of the use of laser or electron beams for rapid quenching is that there is a perfect contact between the liquid metal and the solid, allowing ideal cooling situation to exist. If the material has a glass forming composition or in other words a high GFT and if the cooling rate exceeds 10^6 °C/sec, liquid metal becomes an amorphous solid during solidification. Since Breinan and co-workers (1976) produced amorphous layers at the surface, (section 2.4.1) some research workers have shown interest in using this method to produce metallic glasses. Becker, Sepold and Ryder (1980)

produced about 10μm thick amorphous layers at the surface of $Fe_{40}Ni_{40}P_{14}B_6$ alloy by means of a laser beam. Yatsuya and Massalaski (1982) produced amorphous layers on the same ternary alloy Pd-Cu-Si which Breinan et al. studied. They observed cracks, which were originated at the sharp demarcation boundary adjoining the amorphous phase. Some cracks extended into the unmelted substrate. Fine cracks which were normal to the interface were found in the intermediate zone between the amorphous phase and the substrate. An increase in the free volume during the formation of amorphous phase (free volume of an amorphous phase > free volume of crystalline solid) leads to tensile stresses at the boundary between the amorphous and intermediate zones. The eutectic mixture consists of brittle phases, and the tensile stresses lead to cracks in the intermediate zone and the substrate, but the crack free amorphous layer itself shows the increase in properties, such as strength and plasticity.

2.4.4. Surface Cladding.

The method of coating a material on a different substrate material followed by surface quenching is used in surface cladding and surface alloying. (Fig.2.6). This method can be very useful in applications involving wear, impact, erosion, corrosion and abrasion resistance. In cladding the power source can be used to melt, resolidify and densify the pre-applied coating on the substrate. Application of the coating can be carried out by plasma spraying, sputtering, electro-deposition or by spreading loose powder on a substrate. The laser or the electron beam also melts a very thin layer of the workpiece. This thin liquid layer mixes with the liquid cladding alloy and subsequently freezes to form a metallurgical bonding between the cladding alloy

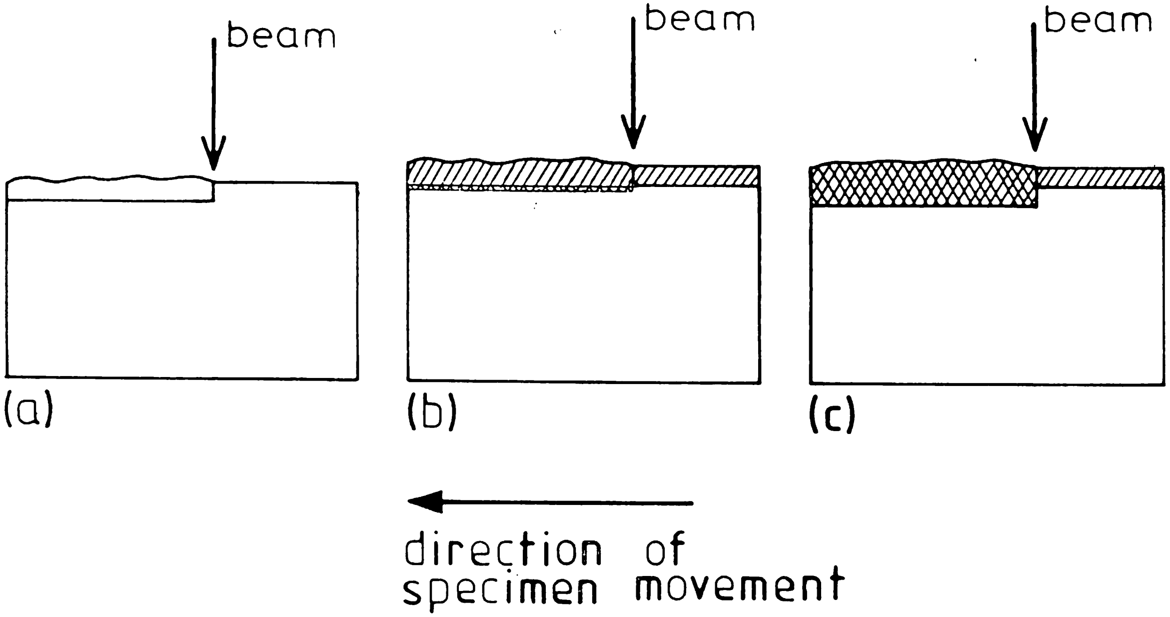

Fig.2.6. Schematic diagrams of

(a) surface melting
(b) surface cladding
(c) surface alloying
using electron or laser beams.

and the substrate. The control of the heat input is critical during cladding because excessive heat can locally melt the base metal resulting in undesirable dilution of the cladding material, which leads to substantial loss of properties of the clad surface.

Bergmann and Mordike (1980 , 1981) produced Ni_xNb_{100-x} metallic glass layers by prior application of a 20-40 μm thick $Ni_{60}Nb_{40}$ powder on the surface of a niobium single crystal, followed by electron beam melting. The melting of the substrate crystal underneath was controlled by varying the process parameters, so that nickel concentration necessary for the metallic glass formation was not unduly diluted. By this method, amorphous beads on single crystals were obtained. It seems that the complete surface layer was made by the rotation and translation of the specimens while the beam was scanned. These amorphous layers were reported to be crack free. No cracks have been found even in the boundary areas between the amorphous region and the substrate. It is interesting to note that they have reported obtaining a complete amorphous layer covering the surface. It was reported that no evidence of crystallization of the beads by subsequent passes has been detected although no proof has been shown.

This method was also used by Tucker and Ayers (1981) to produce amorphous layers of a brazing alloy (Ni-7Cr-2.8B-4.5Si - 3Fe) on a steel substrate. After the application of the powder, the specimens were vacuum sintered to provide sufficient bonding and both electron and laser beams were used as the source of melting. By scanning the beam and moving the specimen, complete surface areas were rapidly quenched. There was a tendency for the coatings to crack during the solidification but it was controlled by scanning the beam at low speeds (less than

2cm/s). However, although reducing the beam speed gave better results in this case, it should be noted that the speed relates to the interaction time of the beam at any point, which in turn relates to the cooling rate. For every power used, they found a certain critical speed, which should be exceeded in order to obtain amorphous phases. Individual laser melt passes at high sample translation speeds were found to be structureless and have been confirmed to be amorphous by electron diffraction. The areas, covered by multiple passes of different speed levels were subjected to X-ray examination and the diffraction patterns showed that overlapping melted regions remain amorphous only when rapidly quenched with a sufficient high speed; that is at very low interaction times. These results are more acceptable than the results of Bergmann and Mordike (1981) and show that a solidification rate higher than that needed to produce an amorphous structure in a single melt pass is necessary to avoid surface cracking or crystallization, when overlapping melt passes are employed.

The concept of the 'layerglaze' process described by Breinan and Kear (1977) is the sequential build up of bulk rapidly chilled structures on a substrate by surface cladding using laser beams. In this process a mandrel is rotated and traversed (Fig. 2.7) in a controlled helium atmosphere and the alloy to be clad is continuously fed to the laser beam interaction point in order to deposit material on the circumference of the mandrel. Breinan and Kear reported the deposition of 0.23 and 0.51 cm thick 304 stainless steel (72Fe, 18Cr,8Ni,1.5Mn,0.5Si) layers by this method. The layerglazing of Ni and Co base alloys were also carried out and the specimens with Co-Ta-C alloy cladding have exhibited a higher yield strength than that of hot isotatically pressed

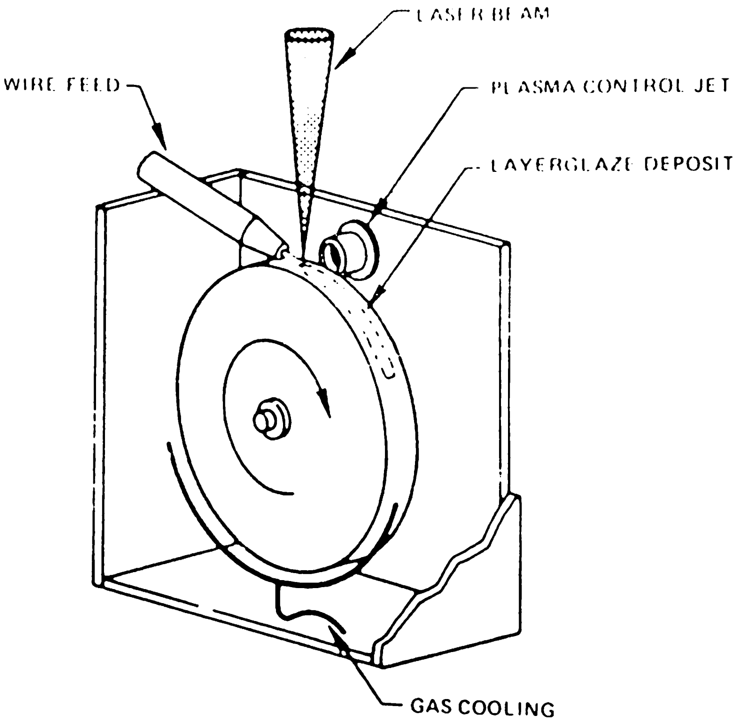

Fig.2.7. Schematic diagram of the layerglaze process (After Breinan and Kear 1977)

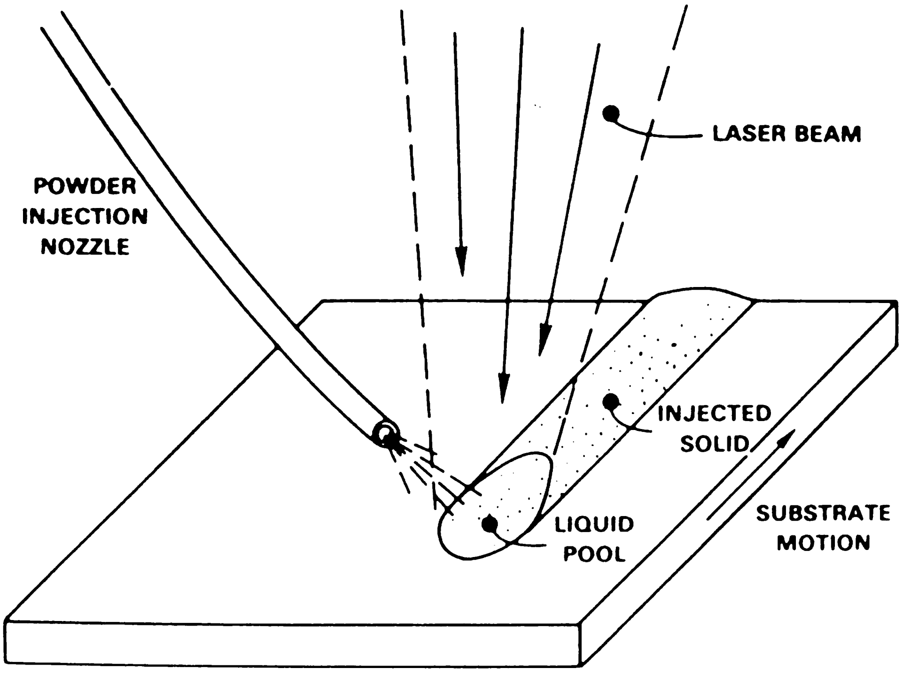

Fig.2.8. Schematic diagram showing injection of particles into a melt zone established by a laser beam. (After Ayers, Tucker and Schaffer 1980)

Co-Ta-C alloy.

Gnanamuthu (1979) successfully clad several alloys on different substrates using laser beams. A cobalt base alloy was clad to a steel containing 2.25%Cr and 1%Mo. Cladding thicknesses of 6-7mm and widths of nearly 10mm were reported to be achieved by a single sweep. Cast rods of an alloy containing M_7C_3 and M_6C carbides in an austenitic cobalt matrix also were clad to AISI 4815 (0.15C, 0.5Mn, 3.5Ni,0.2Mo). In both cases EPMA revealed that the compositions were constant across the cladding thickness and that the dilution of the cladding alloy with the substrate was less than 5%wt. Another important use of surface cladding is that a high melting point alloy can be clad to a low melting point substrate. Clad layers containing a high volume fraction of silicon particles in an Al-Si eutectic matrix were produced by Gnanamuthu, by applying silicon (m.p. of 1430°C) on aluminium alloys. (m.p. range 508-649°C). A harder clad layer on steel has also been produced by the application of a mixture of tungsten carbide particles ($\sim$ 0.5 mm size) and iron powder followed by laser beam melting.

A study by Montgomery (1979) involved the laser treatment of electrodeposited chromium plating. Chromium layer had a high hardness of 920-1140 Knoop Hardness Number but after the treatment it became softer with hardness values ranging from 150-280 KHN. Snavely and Faust (1950) found the same softening effect of electrodeposited chromium layers and attributed this effect to the recrystallization and grain growth. According to Sully and Brandes (1967), agglomeration of the oxide constituents which occur in the chromium layers upon heating contributes to the softening. Greco's (1981) laser beam quenching experiments on chromium and combined chromium-cobalt electrodeposited layers also confirmed this softening effect.

Steen and Courtney (1980) reported a study, in which lasers were used to clad Stellite 12 hardfacing alloy (Co-29 Cr-9 W - 1.8C) onto a Nimonic 75 (Ni-20Cr-0.4Ti - 5Fe) substrate. The cladding alloy powder was applied on the substrate by levelling off a pile of powder and the surface was transversed across a laser beam. Depending on the process parameters used, extensively melted areas of the substrate, well adhered continuous layers and discontinuous poorly adhered layers were obtained. The onset of the non-wetting region of the solid by a liquid cladding alloy was characterised by a particular value of the average energy per unit area. It was shown that a critical value of the average energy per unit area should be exceeded, to achieve wetting and that critical value varies with the thickness of coating.

2.4.5. Surface Alloying

Surface alloying using an electron beam or a laser beam is a similar process to surface cladding, except that the alloys or the elements added are expected to mix completely and diffuse into a thin layer of the substrate. This process is carried out either by the application of a coating on a substrate, followed by surface melting treatment or injecting the alloy particles simultaneously with the surface melting. (Fig.2.8). However the latter method is difficult to carry out when the electron beams are used since the process has to be carried out in a vacuum. During melting, alloying elements diffuse into the liquid substrate and on freezing, form solid solutions and compounds. Superior chemical, physical and mechanical properties can be achieved by adding suitable elements. The depth of the alloying layer can be controlled by the control of power input and the traversing speed. Copley, Bass et al.(1978) and Copley, Beck et al. (1979) described the microstructure of laser alloyed Ag-Cu films. A

Ag-6.6%wtCu alloy with a 5 μm thick electroplated Cu layer has been subjected to laser quenching. In the transverse cross sections of re-solidified areas, regions of copper rich solid solutions surrounded by eutectic mixtures were observed at the edges, where copper electrodeposited layers had submerged onto the melt pool. Ag rich and Cu rich regions and eutectic areas were well observed. Although this alloy is a single phase solid solution at its melting point, after alloying with copper film, the copper concentration in the melted region exceeded the maximum solid solubility limit of copper in silver.

The manufacture of Cr-steel surface alloys on low carbon steel substrates has been described by Weinmann, De Vault and Moore (1979) and Moore and Weinmann (1979). Specimens of 1018 steel with 2 to 18μ m electrodeposited or sputter-deposited chromium layers were irradiated with laser beams. The resolidified regions showed no solidification cracking or porosity. With the same processing conditions the melt layers contained average Cr contents of 2-11 %wt, depending on the thickness of chromium layer.SEM examination of the surface of melted layers showed a dendritic structure and based upon these dendritic spacings cooling rates of 10^5 -10^7 °C s^{-1} during the solidification were estimated. Electron microprobe analysis demonstrated that chromium was uniformly distributed in the melted region. For large area coverage of the substrates, a series of overlapping passes have been employed. Due to the overlapping of passes, it is possible that some areas would contain less chromium, thus weakening those regions. To avoid this, they suggested to process the surface a second time, probably normal to the first set of passes, so that the mixing will be maximum and the composition variations will be reduced.

Plasma sprayed coatings of titanium and 316L stainless steel (18Cr, 12Ni, 0.03C, 2Mn) on steel substrates have been subjected to laser surface treatment by Ayers and Schaffer (1979). A difficult problem encountered in surface melting these layers was the expulsion of the gases entrapped in the layer. During melting, the trapped gases were expelled, sometimes blowing the material away. Due to this reason, the most successful consolidations were carried out with only very thin plasma sprayed coatings. (thickness <0.5 mm) in which the amounts of entrapped gases were minimum. Another problem which had arisen during the rapid solidification of plasma sprayed coatings was the frequent formation of cracks caused by thermal stresses and porosity. Due to these problems, so far the laser or electron beam surface melting of plasma sprayed layers has been unsatisfactory.

Another process involving laser surface melting was reported by Ayers, Tucker and Schaffer (1980), whereby carbide containing layers were produced at the surfaces of different metals. This method does not need a coating prior to surface melting. The added material retains its composition and in that respect, it is different even from the surface alloying, in which the added material is dissolved into the substrate melt. In this process a laser beam is used to melt a thin layer of the substrate. (Fig.2.8). Carbide powder particles are blown to the melt pool from a fixed nozzle, which is positioned near the interaction point. These powder particles are incorporated into the surface as the melt pool solidifies. Ayers et al. injected wear resistant particles (e.g. TiC and WC) onto different substrate materials. Measurements carried out in a Ti - 6Al-4V melt injected with TiC, showed that the volume fraction of carbide in the melt decreased as the laser power was increased. It was shown that about 7% of injected carbides had dissolved in the melt. The observation of localised clusters of dendritic titanium carbides in the solidified region, also showed that a few carbide particles have dissolved and resolidified. Although the injection of TiC particles was successful, the results of the injection of WC to stainless steel and Inconel x-750 superalloy substrates were unsatisfactory since WC particles partially dissolved and embrittled the matrix. This embrittlement, caused by the formation of brittle Fe-W or Ni-W carbides lead to cracks in the resolidified region.

2.4.6. Property Evaluation.

Most of the investigations on electron or laser beam surface quenching were restricted to microstructural studies and microhardness measurements. Property evaluation of the modified layer has been carried out only by a few workers. Anthony and Cline (1979) performed intergranular corrosion resistance tests and mechanical tests of laser beam surface treated 304 stainless steel (72Fe, 18Cr, 8Ni, 1.5Mn,0.5Si in %wt. The surfaces of sensitized (made susceptible to intergranular corrosion) specimens were rapidly quenched and were subjected to standard Strauss tests (in a boiling solution of 10%H_2SO_4 + 10% $CuSO_4$ for 72 hours). There was a complete grain boundary disintegration at the unprotected areas but a complete absence of attack was observed in the laser treated areas. The protective effect of laser surface melting is being illustrated by the observations of intergranular attack, which has spread through a gap which existed in the treated area. Mechanical tests showed that the yield strength of the laser treated sample was greater by about 6 x 10^7 Pa than either the normalised or sensitized samples. It has been estimated that the laser treated area has a yield strength about 10 times greater than that of the rest of the sample. Moore, Kim and Weinmann (1979a) tested the susceptibility of the laser quenched layers to stress corrosion crack initiation. The experiments carried out on titanium alloys showed that pitting occurred in the stressed areas of the untreated alloy. Microcracks propagated from many of the pits. Some of the pits were linked by these microcracks until there was a continuous crack. In the laser treated samples cracks were mainly found in the heat affected zone with only a few occasional cracks in the melted region. It seems that the residual stresses in the heat affected zone were sufficient to cause stress corrosion cracks. The results observed by both Moore et al and Anthony and Cline, show that the laser treated areas have a good corrosion resistance but incomplete coverage of complete surface areas would result in local areas highly susceptible to stress corrosion cracking.

Carbide injection to surfaces using laser or electron beams may prove valuable in applications involving dry sliding wear because the coefficient of friction of the surfaces can be reduced by this process. Ayers, Tucker and Bowers (1980) showed this effect by injecting titanium carbides to a Ti-6Al-4V alloy samples. The values of kinetic coefficients of friction (μ_k) of these samples were between 0.4 and 0.45, prior to the surface treatment but were reduced after the injection of TiC particles. The value of μ_k dropped with increasing volume fraction of TiC, achieving a minimum value of 0.16 at a volume fraction of about 0.5. Ayers, Schaffer and Robey (1981) carried out wear tests on surface treated specimens using dry sand/rubber wheel test and reported that the laser quenched samples performed substantially better than the untreated alloys. Wear rates of the treated surfaces were only a few percent of those of the untreated area. Ruff and Ives (1982) carried out wear tests of surface melted tool steel, under dry sliding conditions. The rapidly quenched surfaces showed a 25% reduction in the wear rate may have been caused by the high hardness of the layer and the finer microstructure produced by this process.

The feasibility of improving the cavitation erosion resistance of laser beam rapidly quenched 1040 steel (0.4C, 0.8Mn in %wt) and 303 stainless steel (18Cr, 9Ni, 0.15C, 2Mn, 0.6Mo) was examined by Preece and Draper (1981). The surfaces, which were completely laser beam treated were exposed to cavitation in deionized water. The mass loss data of the material, as a function of time of exposure to cavitation erosion, showed that despite the initial rough surface,laser treated samples were less eroded than the untreated samples. However, after the initial attack at some areas of the rapidly quenched layer, deep pits were produced due to the susceptibility of the untreated areas to erosion. Surface roughness, which results in rapidly quenched surfaces seems to be detrimental to erosion resistance. Mass loss can be increased due to the removal of the surface asperities by necking down due to the impact pressure or the fluid flow. Formation of surface ripples is certainly a disadvantage. This rough surface can also act as a surface with shallow cavities and accelerate corrosion than in a smooth surface. Formation of these ripples has been studied by Anthony and Cline (1977) and will be discussed in chapter five with the results of the present work.

CHAPTER 3.

3. Experimental Materials and Techniques

3.1. Experimental Materials

The materials used in this work mainly consisted of an ultra high-strength alloy steel and a few iron based alloys with high glass forming tendency. The ultra high-strength alloy steel was supplied by the RARDE, Fort Halstead and had the following composition in %wt.

0.38C, 2.9Ni, 0.23Si, 0.55Mn, 0.7Cr
0.57Mo, 0.2V and balance Fe.

This steel had been austenitised at 980°C for 1 hour before quenching in oil, then secondary hardened by keeping at 620°C for 6 hours and quenching again in oil. After secondary hardening, the steel had been kept at 400°C for 4 hours for stress relief to occur. In this as received condition it consisted of a tempered martensitic microstructure. All the rapid quenching experiments using this steel, were carried out in this as received condition.

Most of the alloys were made in the department but some of the $Fe_{80}P_{13}C_7$ alloys were cast at RARDE, Fort Halstead. Concentrations of the main alloying elements in the alloys used are given in Table 3.1. The alloys, prepared in the department were made by melting the alloys in an argon atmosphere either in a Balzer high-vacuum induction furnace or a Via-vac vacuum melting furnace. The tentative application requires an alloy with a high capability of glass formation as well as the retention of the amorphous nature, when subjected to rapid quenching repeatedly. Therefore these eutectic alloy compositions were chosen, because of their high glass forming tendencies. These alloys were prepared several times resulting in slightly different variations in composition. The range of compositions are given in Table 3.1. Glass forming ability is not affected by small composition variations, so the effect was not significant. Although all these alloys were used in the experiments, most of the work was carried out on $Fe_{80}P_{13}C_7$ alloy.

For the application of powder layers of $Fe_{80}P_{13}C_7$ alloy on steel for surface cladding, the alloy was powdered at Davy-Loewy Limited, Bedford. Powder of particle size less than 100 mesh were mixed with a binder; Collodion. When the powder was slightly wet, it was pressed between the cleaned surface of a specimen and a glass slide, both of known thicknesses. By clamping the whole unit together and pressing, the necessary thickness of coating was obtained. When the powder was dry, the glass slide was removed thus obtaining a powder layer on the specimen.

3.2. Electron Beam Rapid Quenching Process

A CVE 60 electron beam welder was used for rapid quenching of materials described in the present work. It mainly consists of a vacuum system, an electron gun and a working stage inside the vacuum chamber of 30 x 30 x 30cm dimensions. The electron gun is a triode, thermionic type, with a tungsten filament. There are three fixed voltages (40, 50 and 60 kV) and necessary power can be obtained by changing the emission current at a fixed voltage setting.
Fig.3.1 shows the front section of the electron beam welder. The vacuum chamber, gun column and the control unit are shown but the section containing the rotary pumps are not visible.

Using the rotary and diffusion pumps, the chamber was usually pumped down to a pressure below 10^{-4} Torr, before the emission of electrons. Focussing was done by adjusting the electromagnetic coils. An electro-

Table 3.1.

Compositions of alloys used in the experiments (in %wt.)

Alloy	C	P	Cr	Fe
$Fe_{80}P_{13}C_7$	1.6 - 1.8	8.0 - 8.5	-	89.0 - 91.0
$Fe_{70}Cr_{10}P_{13}C_7$	1.7 - 1.8	8.0 - 8.2	10.0 - 11.0	78.0 - 81.0
$Fe_{60}Cr_{20}P_{13}C_7$	1.6 - 1.8	8.0 - 8.3	21.0 - 22.0	67.0 - 69.0

Fig.3.1. Electron beam quenching equipment.
(a) gun column
(b) vacuum chamber
(c) control unit

Fig.3.2. Inside view of the vacuum chamber.
(a) specimen
(b) high speed rotating stage
(c) horizontal traverse stage

magnetic deflection of the beam up to 10 degrees from the vertical could be obtained in two orthogonal directions. The small interaction time (duration, which the beam was on a point of a material) necessary for a higher cooling rate in rapid quenching was obtained by traversing the specimen under the focussed beam. In this machine, there were no facilities for the high speed electromagnetic deflection or oscillation of the beam over a wide area.

The working stage could be moved linearly in two orthogonal directions at varying speeds with a maximum speed of 4.4cm s^{-1}. Electron beam welder also consisted of a 5cm diameter rotating stage, but rotating speed was too low for the use of rapid quenching process. Therefore a high speed rotating stage was designed and was made in the department. Fig.3.2. shows the linear and the rotating stages inside the vacuum chamber. For a certain rotating speed of the disc, traversing speed of the specimen was varied by changing the position of the specimen on the disc. With an increase in the distance between the position of the specimen on the disc and the centre of the disc, the traversing speed of the specimen under the beam was increased up to a maximum speed of 36.4cm s^{-1}. Prior to the interaction with beams, specimens were ground down to 180 grit size. No coatings were applied for the absorbtion of power, since electron beam to material energy transfer efficiency is high.

3.3. Melt Spinning Apparatus.

To obtain rapidly quenched material for the initial studies of micro-structural changes, which occur in rapid quenching, melt spinning was used. The melt spinning apparatus is described here briefly. A schematic diagram of the apparatus is shown in Fig. 2.2. The metal or alloy was kept in a silica crucible with a little orifice at the bottom, and was heated using radio frequency waves. On melting, the liquid metal was pressurised and a jet of molten metal was directed onto the surface of a brass disc, which was rotating with a

circumferential speed of 13.5 ms^{-1}. The liquid was thereby drawn into a thin rapidly quenched ribbon with an average thickness of ∿50μm and an average width of 2.8mm. To prevent oxidation and contamination during the heating and melting, this process was carried out in a helium atmosphere.

3.4. Sputter Deposition

The conventional high pressure direct current sputtering process was employed for sputter deposition. A 3 x 2 x 0.8cm solid of $Fe_{80}P_{13}C_7$ alloy was used as the cathode. The sputtered alloy was deposited on high strength alloy steel substrates. Usually flat specimens of 2 x 2 cm dimensions were used as the substrates but in the case of samples for the vented chamber erosion system (vide section 3.10) a curved segment was used. The flat specimens were ground and polished on diamond wheels to 1μm size. All the specimens which were used as substrates were ultrasonically cleaned prior to assembling. The substrates were placed directly opposite and as much as possible near the centre of the target (cathode), in order to obtain a uniform deposition profile. Different thicknesses of sputtered films were obtained by varying the distances between the substrates and the target. The average distance was about 2cm. It was highly desirable that the substrate temperature remains constant throughout the film growth in order to ensure the amorphous structure of the films and the adhesion of the film to the substrate. During sputtering, the temperature of the substrate increases substantially by bombardment of charge carriers. Therefore liquid nitrogen in contact with the anode assembly was used as a heat sink.

For better adhesion of the film to the substrate and for the development of a uniform film, the pre-cleaning of the substrate surface and the target was very important. At first the chamber was pumped down to about 10^{-9} Torr, in order to remove most of the gaseous contaminants to ensure that the outgassing by impurities during sputtering was minimal. Then, purified argon gas was introduced to the chamber. The target was cleaned first by pre-sputter cleaning for 2 hours, during which time the substrate was kept shielded. The substrate was also pre-sputter cleaned for 10-30 mins by temporarily making it the cathode and after that the target was pre-sputter cleaned again for about 10 minutes. After this cleaning procedure, the final sputter deposition was carried out.

Argon was used in sputtering with a gas pressure of about 0.3 Torr. Sputter deposition was carried out using different arc voltages, the average current and voltage being about 55mA and 580V respectively. The duration of sputtering was also varied in the range of 24-72 hours, in order to obtain films with different thicknesses. The sputtering rate was about 0.5 - 1.5 °A per second.

Sputter deposition by magnetron sputtering was also tried to increase the rate of deposition. In magnetron sputtering, a low gas pressure was used, but at low pressures, thermalisation of sputtered particles (vide section 2.3.1) is not efficient as at high pressures. Consequently the sputtered particles reach the substrate with higher energy. Sputtered films obtained by magnetron sputtering were not amorphous and the adhesion to the substrate was also poor probably due to the reasons given above. Therefore magnetron sputtering process was abandoned.

3.5. Metallography

3.5.1. Optical Metallography

For optical metallography, specimens were mounted in bakelite in hot mounting presses. Since crystallisation temperatures of the metallic glasses used were much higher than the temperatures used in hot mounting, it was safe enough to use without causing any structural damage to metallic glasses. The specimens, in which the edges were investigated were mounted in special edge-mount green bakelite. This resin has a higher hardness and during grinding and polishing, reduces the curving effect of the edges. The surfaces were ground down to 1200 grit size using silicon carbide abrasive papers and then were mechanically polished using diamond paste to 1μm. 2% Nital was suitable to etch all the specimens except Fe-Cr-P-C alloy specimens. Those specimens were etched using a solution of $CuSO_4$ (10 g) in 50% HCl.

3.5.2. Scanning Electron Microscopy

Scanning electron microscopy was used to study the surfaces of sputtered, plasma sprayed and electron beam quenched samples and in some cases to study the microstructure of the cross sections of electron beam quenched regions. A Cambridge Stereoscan II A and an International Scientific Instruments 100, scanning electron microscopes were used, operating at 40kV. Generally secondary electron imaging was used but X-ray imaging was also employed for the investigation of the distribution of certain elements in rapidly quenched regions.

3.5.3. Transmission Electron Microscopy

Transmission electron microscopy was carried out on JEM 200, Phillips 300 and Phillips 400 instruments operated at accelerating voltages of 200, 100 and 120kV respectively. In the cases, where the obtained thin areas were comparatively thicker to examine under these microscopes, a high voltage electron microscope was used at an accelerating voltage of 500kV. Bright field, centred dark field and diffraction modes were employed.

Thin foils for transmission electron microscopy were prepared either by ion-beam thinning or electrochemical thinning. In the case of melt spun ribbons, 3mm long pieces were cut and were mechanically ground prior to electrochemical or ion-beam thinning. Due to the thin nature of the ribbon, conventional grinding was not possible. Pieces of melt spun ribbons were adhered to a steel block with the use of double sided cellotape and were carefully ground. Obtaining the thin foils of electron beam rapidly quenched areas was also difficult and was a long process. The steps used in the preparation of thin foils are shown schematically in fig.3.3. After electron beam quenching, about 0.8mm thick surface layer was cut by spark erosion technique using a copper wire (Fig.3.3b). Then this layer was adhered to a brass plate using a conducting adhesive material; a mixture of Durofix glue and carbon powder. When the adhesive was dry, 3mm diameter discs were cut using the spark machine (fig.3.3c) in such a way that the electron beam treated area was across the disc (fig.3.3d). These discs were then thinned to a thickness of about three thousandths of an inch by mechanical grinding of the untreated side of the disc. (fig.3.3e). The electron beam treated regions of these thin discs were a little thicker than the untreated area due to the surface ripples present in that area. Consequently when the discs were thinned, the untreated areas were thinned relatively sooner. To avoid this problem, in the case of electrochemical thinning, Lacomit was used to cover the whole untreated area of the electron beam treated side of the disc. (fig.3.3.f). Thus only the rapidly quenched area was allowed to be thinned. When the ion beams were used, ion bombardment was carried out only from the untreated side. Tantulum plates with very small holes were used to hold the specimens, in order to expose only the rapidly quenched region to the ion bombardment.

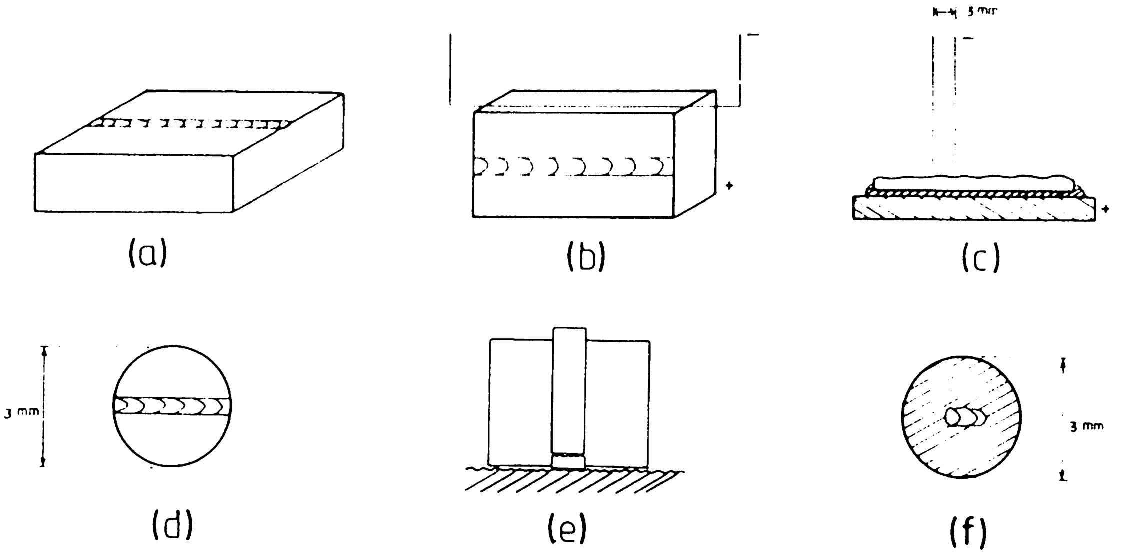

(a) (b) (c)

(d) (e) (f)

Fig. 3.3. Schematic representation of the steps used in the preparation of thin foils.

(a) Surface melted specimen
(b) spark erosion cutting of ∿ 0.8mm thick layer
(c) spark erosion cutting of 3mm diameter discs.
(d) 3 mm diameter but ∿0.8mm thick disc
(e) mechanical grinding
(f) ∿ 75µm disc, surface except the centre is covered with Lacomit.

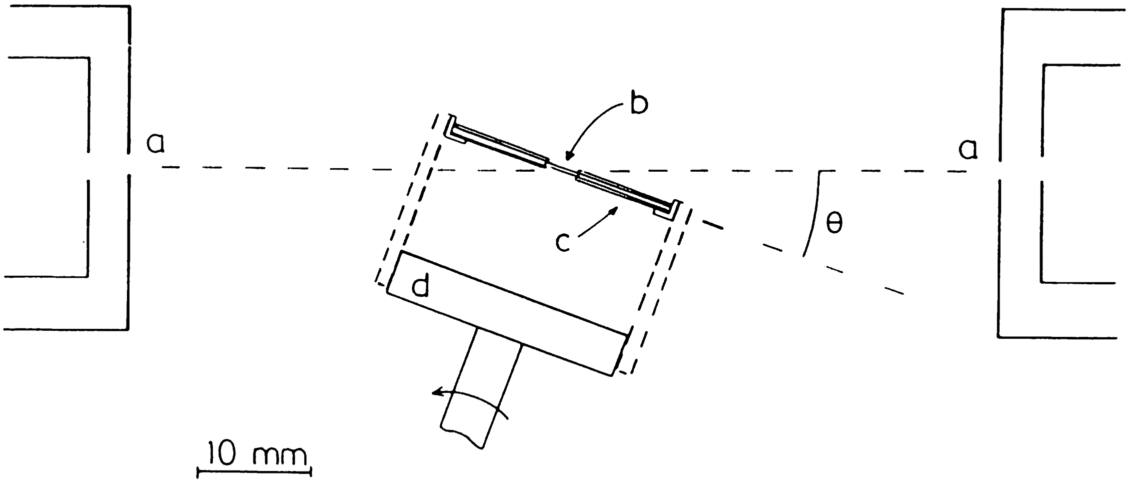

Fig.3.4. Schematic diagram of the arrangement in the vacuum chamber of ion beam thinning machine.

(a) Ion beam
(b) Specimen
(c) tantulum plates
(d) specimen holder
θ = grazing angle

The methods used for specimen thinning are described below.

a) Ion Beam Thinning - The principle of this technique is the use of ion bombardment on a material to remove atoms from the surface of the material. An Edwards ion beam thinning machine was used in this work. A schematic diagram of the arrangement in the vacuum chamber is illustrated in fig.3.4. The specimen was held between tantulum plates in the holder and was bombarded either from both sides or one side, as the case may be by argon ion beams. The specimen holder was rotated, so that the beam bombards a non-stationery surface giving a smooth thin area. The grazing angle could be varied. An angle of between 15-20° would give a suitable smooth surface at a reasonable thinning rate. Usually the thinning rate was slow. At 6kV and 60μA beam current, thinning rate was about 1μm per hour. Heating of the specimen during the ion bombardment (Greer 1979) was a disadvantage. Greer showed that the heat effects during the ion beam thinning affected the structure of the metallic glass. Hence, in the present work, this mode of thinning was only used for thinning crystalline materials.

b) Electrochemical thinning - A Fischione twin jet polisher was employed for electrochemical thinning using either 5% Perchloric acid in Butoxyethanol solution or 5% Perchloric acid, 25% Glycerol in Ethanol solution. Since the polishing, pitting or etching of the surface depends on the applied voltage (Hirsch et al 1965), the voltage was adjusted to get the best polishing effect. The solution was cooled to slower the reactions in order to obtain larger thinned areas. After polishing, the specimens were cleaned in a gentle stream of alcohol. Lacomit coated thin foils were washed in acetone to dissolve the coating.

Some of the thin areas obtained by these methods were not electron transparent for examination by transmission Electron microscopy even at an accelerating voltage of 200kV. Therefore a high voltage electron microscope was used at an accelerating voltage of 500kV. The techniques of thin foil preparation used for different materials are given in Table 3.2.

3.5.4. Micro-analysis

To investigate the compositional variations in sputtered, plasma sprayed and electron beam quenched samples, microanalysis was performed using a Cambridge Scientific Instruments Microscan 5 Electron Microprobe Analyser (EPMA) and an Energy Dispersive System (EDX) linked to ISI 100 Scanning electron microscope. EDX analysis was carried out at an accelerating voltage of 20kV and the specimen was tilted at an angle of 45° to the beam enabling the X-rays to reach the silicon detector. Although a beam size of ∿1000A° was used, the beam instability may have caused a size variation. Obviously EDX analysis could not be employed to analyse elements such as carbon, but in all the analyses carried out, corrections for atomic number effect (Z), absorption (A), and fluorescence (F) were made. In some cases, the electron probe microanalyser with a Wavelength Dispersive Spectrometer (WDS) was used to obtain concentrations of elements including carbon. EPMA analysis was carried out at 16kV, with a spot of 1μm. Since the ZAF correction was not carried out on the EPMA analysis, these results were used only for qualitative assessments.

3.6. X-ray Diffraction Techniques

X-ray techniques were used to verify the amorphous nature of the metallic glass and to measure the lattice parameters of crystalline melt spun ribbons and electron beam rapidly quenched regions. A

Table 3.2

		Thinning Technique				
		Electrochemical				
	Material	solution*	Voltage V	Temp °C	Ion Beam	Comments
1.	As received ultra high-strength steel	B	55	Room temp.	not used	
2.	Melt spun crystalline materials	A	70	-10	used	Better thin areas by ion beam thinning
3.	Melt spun glassy materials	A	70	-10	not used	
4.	Electron beam quenched crystalline materials	A B	70 90	-10 -15 to -20	used	solution B was better
5.	Electron beam quenched metallic glass	A B	70 90	-10 -15 to -20	not used	solution B was better

* A - 5% perchloric acid in Butoxyethanol

B - 5% perchloric acid, 25% Glycerol in Ethanol.

Phillips PW 1390 vertical diffractometer was used with a standard proportional counter and conventional counting electronics.

In the case of melt spun ribbons, an aluminium plate with a 15 x 25 mm rectangular hole in the middle was used for mounting the ribbons. Flat plate specimens were constructed by mounting about 30mm length pieces of ribbons, side by side across the hole, using double sided cellotape on two sides of the hole to stick the ribbons evenly and flat. When placing these specimens, it was ensured that X-ray beam was incident only on ribbons. It was difficult to collimate the beam on the electron beam quenched regions of single passes, because these individual passes were too narrow. An effort was made to completely cover the untreated areas of the specimens with thin lead sheets, exposing only the treated areas to the X-ray beam. The lead peaks obtained in the results were ignored.

Either cobalt K_{α} ($\lambda = 1.7902$ Å) or copper K_{α} ($\lambda = 1.5417$ Å) was used from thermionic tubes operated at 40kV and 25mA. Intensity of k_{β} was reduced using iron filters. Step scanning of the materials were carried out. Results, in punched tape form were fed into the computer and computer drawn graphs of intensity vs 2θ were obtained. Since metallic glass has no long range order, when subjected to X-rays, no intensity peaks are given, instead, only a hump over a range of 2θ is shown. This lack of intensity peaks was used to check the amorphous nature of the materials. For crystalline materials angle θ was measured at the peaks. The Bragg equation was solved for these angles. Hence spacings of the atomic planes (d) and the lattice parameter (a) were obtained. The technique of weighted least mean square linear analysis of lattice parameter against the Nelson-Riley-Taylor-Sinclair function $\left(\frac{\cos^2\theta}{\sin\theta} + \frac{\cos^2\theta}{\theta}\right)$ gave an accurate lattice parameter (a_o) value when the above function reaches a value of zero.

3.7. Measurement of Crystallization Temperature of Metallic glass

The crystallization temperature of $Fe_{80}P_{13}C_7$ metallic glass ribbons was measured by differential scanning calorimetry (DSC). A Du Pont heat flux DSC system consisting of a model 910 calorimeter and a model 990 console was used in this work. The principle of the operation of heat flux type DSC systems has been described in detail by Baxter (1969). In DSC, the sample and the reference material are kept in similar environments and both are subject to identical heat treatments. The temperature difference between the materials is measured. The heat flux type DSC systems are made in such a way that the DSC curves give a plot of the rate of enthalpy change with time as a function of time or temperature. DSC systems can be employed to measure many physical properties of materials (Greer 1979), but in the present work, it was used only for the measurement of crystallization temperature. Crystallization of metallic glasses is an exothermic reaction and this reaction gives rise to a major DSC peak at the crystallization temperature.

Very small sample masses and heating rates were used in order to reduce the distortion of the DSC curve. 4mg samples were used with a heating rate of 10°C per minute. Since the sample mass was small, only the empty specimen container and lid were used on the reference side. Continuous heating was used. Heating was carried out in argon atmosphere at a flow rate of 40ml/minute and at ambient pressure. Temperature was plotted on the abscissa of the chart.

It is known that there is a temperature discrepancy (ΔT) between the recorded temperature and the real temperature of the sample. However, this difference in temperature is so small and not important in this case ,so it was assumed negligible. Greer (1979) using 37.8mg sample of nickel, measured the temperature differences between the sample and references for different heating rates. At a heating rate of 10°C/min, ΔT was about 0.3°C.

3.8. Measurement of Micro-hardness

The measurement of microhardness is a useful method of studying the properties of materials. Since the hardness to yield strength ratio is about 3.2 for metallic glasses and 3.0 for Crystalline materials, the strength of the materials can also be assessed approximately. A Leitz miniload micro-hardness tester, with a diamond pyramid indenter was used in these measurements. Generally 50 and 100g loads were employed. When the load is small, the dimensions of the diagonals are also small, resulting in a larger percentage error during the measurement of diagonals. Therefore the use of very small loads were avoided.

3.9. Measurement of Surface Roughness

Variations of the surface roughness of electron beam melted areas, with the process parameters were investigated. A Ferranti Surfcom 30B surface finish and roughness measuring system was used. This system employs a differential transformer type transducer to sense surface irregularities. A diamond stylus with a tip of 0.003μm radius detects very fine surface irregularities. The transducer is usually driven on the surface to be measured by a tracing driver. The tracing speed can be set to 0.3, 0.6 or 1.5mm s^{-1}. Transducer output is amplified and displayed by an amplifier and indication unit giving measurement normal to workpiece surface in a range from 0.1 to 50μm. The amplifier and the indication unit are connected to a pen recorder which provides a permanent record of the roughness profile.

Surface roughness of electron beam rapidly quenched high strength steel and $Fe_{80}P_{13}C_7$ alloy was measured using a tracing speed of 0.3 mm s^{-1}. The chart speed and the vertical sensitivity of the chart were changed in order to obtain clear profiles of surface irregularities.

3.10. Measurement of Erosion Wear

For the measurement of erosion wear, coated surfaces of steel samples were subjected to hot propellant gas erosion. These tests were carried out at RARDE, Fort Halstead, using a vented chamber erosion system. This system has been described in detail by Glue et al. (1981). A schematic diagram of the vented chamber erosion system developed at RARDE is shown in Fig.3.5a. It consists of a cylinder steel bomb chamber with part of the cylinder modified to hold the samples. These samples (cross sections are shown in Fig.3.5b and 3.5c) are made of ultra high-strength steel and consists of three 120° segments, (three split vent samples) which can be coated separately using external coating sources. These segments are assembled to form a standard nozzle shaped sample and are held in a tapered collar to prevent gas wash erosion of the segment cages during firing. Thus the coated areas resemble a coated inner surface of a gun barrel. This system consists of a vented chamber with the coated samples forming part of the vent. A propellant is ignited in the chamber and the resulting hot gas jet erodes the sample surface as it escapes through the vent. The burster disc helps to raise the pressure of the gas in the sample area before allowing the gas to escape at a critical pressure. Thus a hot pressurised propellant gas environment, approximately similar to which prevails in a gun bore environment is made. The conditions used; a charge weight of 130gm, a burster disc of 2mm thickness and a vent diameter of 12.5mm are known to produce a venting pressure of 150MPa with a venting time of 20ms and a thermal pulse length of 40ms. The erosion of the samples are usually measured by determining their mass loss during each firing.

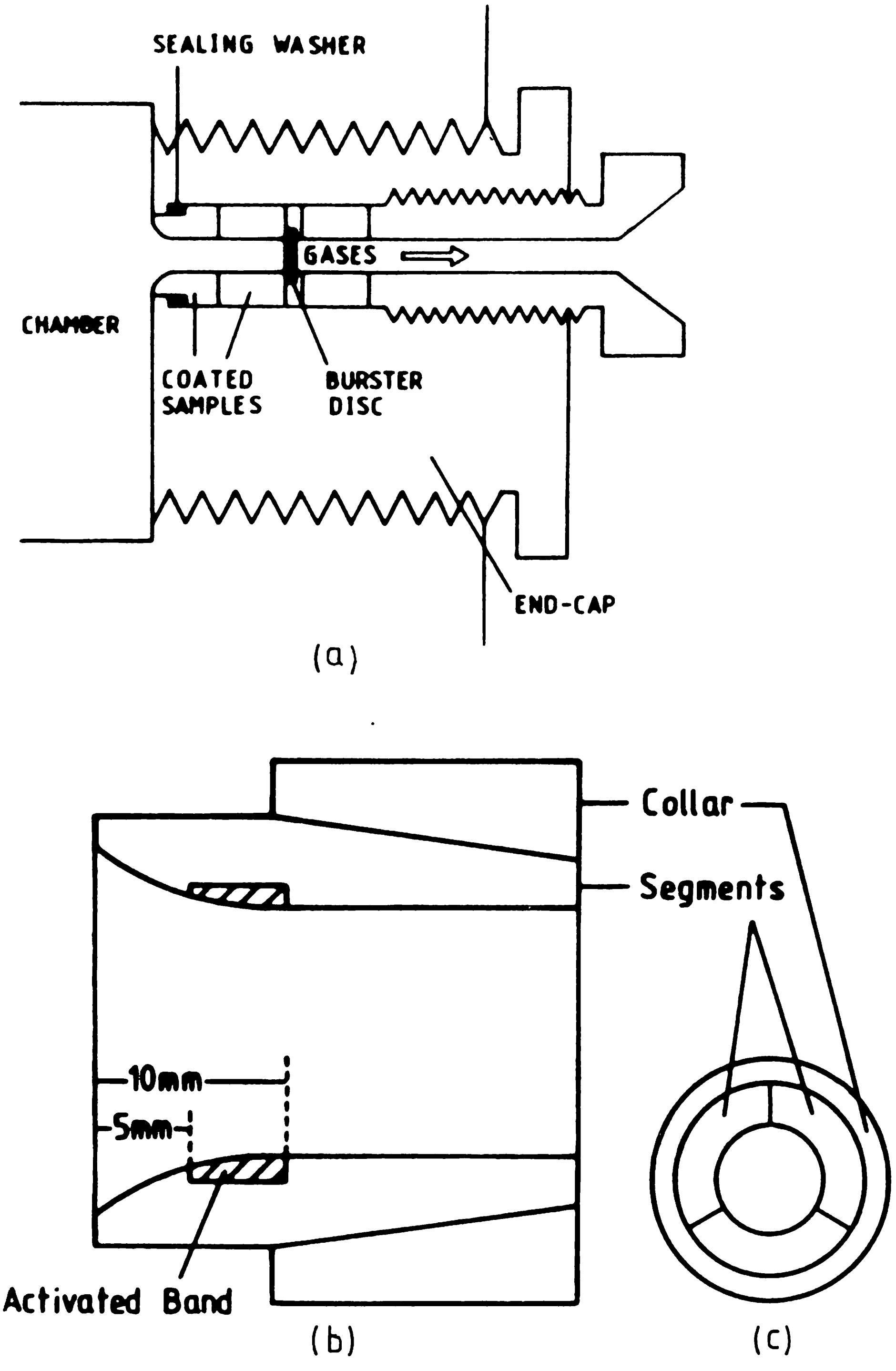

Fig.3.5.

(a) Schematic diagram of the vented chamber erosion system.

(b) Longitude cross section of a split vent sample and the collar.
(c) Transverse cross section of 3 split vent samples held together by the collar.
(After Gibson 1982)

CHAPTER 4.

4. Theoretical Study of Heat Flow in Electron Beam Quenching

4.1. Introduction

During the rapid melting and quenching of materials using electron or laser beams as heat sources, the heat flow distribution and the cooling rate depend on many process parameters, such as beam power and beam speed and the thermal properties of the material. For a better understanding of the process and to obtain optimum results, it is necessary to undertake both experimental and theoretical studies of the heat flow problem involved. This chapter is concerned with the theoretical modelling of the electron beam rapid quenching method used in the present work. One of the best known analytical solutions for the problem of heat flow involving moving point sources, was published by Rosenthal (1946), and has been extensively used in metallurgical applications. This solution was developed for the use in the field of welding, although it can be applied to other processes, which involve moving heat sources. Rosenthal's theory of three dimensional heat flow in a material subjected to a moving point heat source and the results obtained by applying that theory to the electron beam quenching of steels will be discussed in the next sections of this chapter.

4.2. Rosenthal's theory of Heat Flow.

Rosenthal's theory of heat flow involving a moving point source of heat is based upon the experimentally established principle of quasi - stationery state. (Bornfield 1933). Bornfield showed that if a heat source moved at a constant velocity on a sufficiently large body, the temperature distribution around the heat source soon becomes constant. In other words, an observer stationed at the point source, fails to notice any change in the temperature around him as the source moves on. This state of flow is called quasi - stationery. Rosenthal applied this theory to situations requiring the consideration of one, two and three dimensional heat flow. Since thick plates were used in electron beam surface melting, three dimensional heat flow is considered in the present work.

Following nomenclature will be used in this work.

q = rate of heat input Js^{-1}

ν = traversing speed of beam or specimen ms^{-1}

T = temperature °C

t = time s

k = heat conductivity of metal $J\ s^{-1}\ m^{-1}K^{-1}$

$½\ \lambda$ = thermal diffusivity of metal $cm^2\ s^{-1}$

$(\frac{1}{2\lambda} = \frac{c\rho}{k})$

c = specific heat $J\ kg^{-1}K^{-1}$

ρ = density $kg\ m^{-3}$

In using this theory the major assumptions made are as follows.

a) The physical characteristics of the metals, such as specific heat (c) and thermal diffusivity $(\frac{1}{2\lambda})$ are independent of the temperature.

b) The speed (ν) and the rate of heat input are constant.

c) The latent heat of melting is neglected.

d) Cooling is by conduction only.

Fig. 4.1 illustrates the moving point heat source. For the heat distribution, the differential equation of heat flow expressed in rectangular co-ordinates (x, y and z as shown in Fig.4.1) which are referred to a fixed origin in the solid is given in the form,

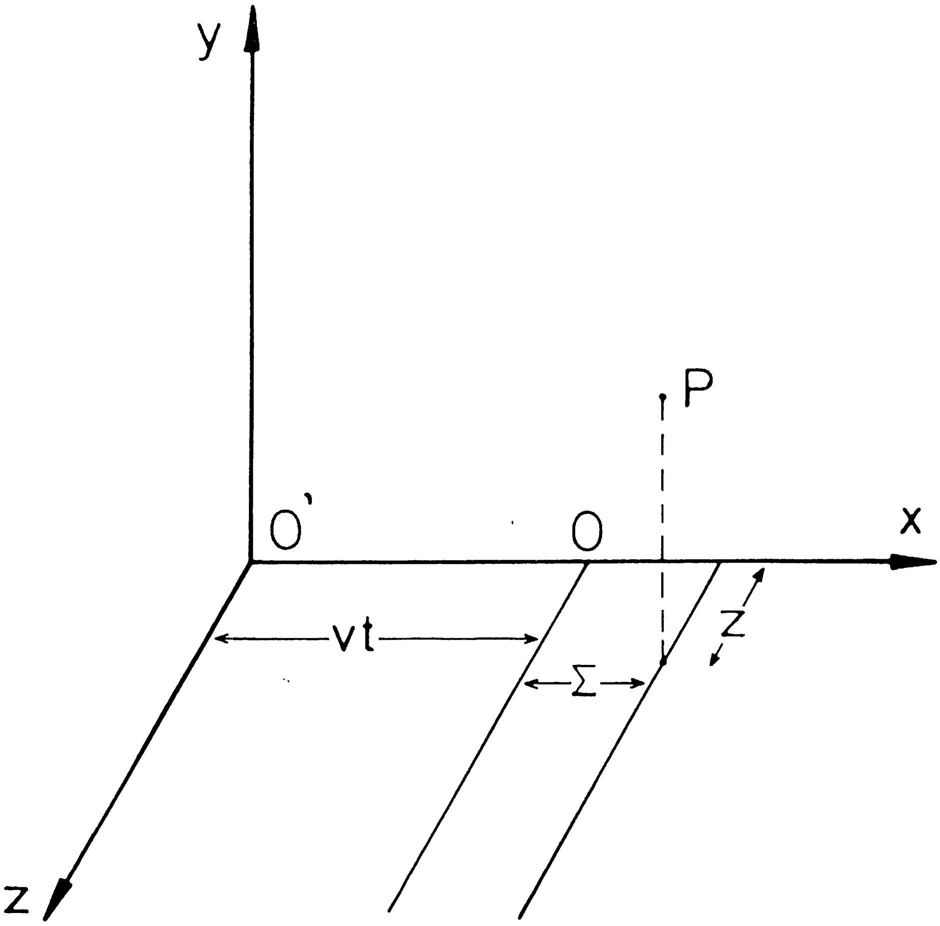

Fig.4.1. Denotations referring to a moving point source of heat.

$$\frac{\delta^2 T}{\delta x^2} + \frac{\delta^2 T}{\delta y^2} + \frac{\delta^2 T}{\delta z^2} = \frac{2\lambda}{} \frac{\delta T}{\delta t} \qquad 4.1$$

Assume that the rate of heat input, q, is supplied by a point source moving along the x axis with a constant speed ν. To determine the temperature distribution around the heat source, a moving system of co-ordinates will be used, with the origin at the point source, O'. After a time t has elapsed, the origin of the system will have been displaced from O' to O, a distance of νt. The coordinates of some point P may be x, y and z with respect to the fixed system and ε, y and z in the moving co-ordinate system, where $\varepsilon = x - \nu t$. Replacing x in equation 4.1 by ε, where ε is the distance of the point considered from the point source and by differentiating with respect to ε,

$$\frac{\delta^2 T}{\delta \varepsilon^2} + \frac{\delta^2 T}{\delta y^2} + \frac{\delta^2 T}{\delta z^2} = -2\lambda\nu \frac{\delta T}{\delta \varepsilon} + 2\lambda \frac{\delta T}{\delta t} \qquad 4.2$$

but, according to the definition of quasi-stationery state, $\frac{\delta T}{\delta t} = 0$

Therefore equation 4.2 becomes,

$$\frac{\delta^2 T}{\delta \varepsilon^2} + \frac{\delta^2 T}{\delta y^2} + \frac{\delta^2 T}{\delta z^2} = -2\lambda\nu \frac{\delta T}{\delta \varepsilon} \qquad 4.3$$

For the simplification of equation 4.3, T is given in terms of,

$$T = T_o + e^{-\lambda\nu\varepsilon} \phi(\varepsilon, y, z) \qquad 4.4$$

where T_o = initial temperature of the solid

ϕ = a function to be determined for various geometrical configurations.

substituting equation 4.4 in 4.3 and after the reduction of terms, the following equation is obtained.

$$\frac{\delta^2\phi}{\delta\varepsilon^2} + \frac{\delta^2\phi}{\delta y^2} + \frac{\delta^2\phi}{\delta z^2} - (\lambda\nu)^2\phi = 0 \qquad 4.5$$

In the case of three dimensional heat flow, if heat flows in ε, y and z directions from a point source at 0, moving in the direction x, the function ϕ depends only on a distance R, where $R^2 = \varepsilon^2 + y^2 + z^2$. Boundary conditions in the three dimensional case are

$$\frac{\delta T}{\delta\varepsilon} \to o \quad \text{for} \quad \varepsilon \to \infty$$

$$\frac{\delta T}{\delta y} \to o \quad \text{for} \quad y \to \infty \qquad 4.6$$

$$\frac{\delta T}{\delta z} \to o \quad \text{for} \quad z \to \infty$$

Also when a spherical surface $4\pi R^2$ is drawn around the heat source with radius R,

$$-\frac{\delta T}{\delta R} \cdot 4\pi R^2 K \to q \quad \text{for} \quad R \to o \qquad 4.7$$

Equation 4.5 has been rewritten as

$$\frac{d^2\phi}{dR^2} + \frac{2}{R}\frac{d\phi}{dR} - (\lambda\nu)^2\phi = o \qquad 4.8$$

Using $\frac{d^2\phi}{dR^2} + \frac{2\,d\phi}{R.dR} = \frac{1}{R}\frac{d^2(R\phi)}{dR^2}$

equation 4.8 becomes

$$\frac{d^2(R\phi)}{dR^2} - (\lambda\nu)^2 R\phi = o \qquad 4.9$$

A general solution of equation 4.9, satisfying boundary condition 4.6 is

$$R\,\phi = Me^{-\lambda\nu R} \qquad 4.10$$

by substituting for ϕ in equation 4.4

$$T - To = e^{-\lambda\nu\varepsilon}.\quad \frac{M\ e^{-\lambda\nu R}}{R} \qquad 4.11$$

This solution, also satisfies the boundary condition 4.7 since $-R^2\,\frac{\delta T}{\delta R}$ tends to a constant value M, when $R \to o$.

Therefore $M = \frac{q}{4\pi K}$

Hence, the temperature distribution

$$T-T_o = \frac{q}{4\pi K}\ e^{-\lambda\nu\varepsilon} \cdot \frac{e^{-\lambda\nu R}}{R} \qquad 4.12$$

That is, the temperature at a point in the melt zone is given by

$$T = \frac{q}{4\pi K}\ e^{-\lambda\nu\varepsilon} \cdot \frac{e^{-\lambda\nu R}}{R} + T_o \qquad 4.13$$

By differentiating equation 4.13 with respect to time, the cooling rate can be obtained.

$$\frac{\delta T}{\delta t} = \frac{q}{4\pi K}\ (\alpha\beta)\ \left(\frac{\varepsilon\nu}{R^2} + \frac{\lambda\varepsilon\nu^2}{R} + \nu^2\lambda\right) \qquad 4.14$$

where $\alpha = e^{-\lambda\nu\varepsilon}$

and $\beta = \frac{1}{R}\,(e^{-\lambda\nu R})$

According to equation 4.13, the temperature at the point of the heat source on the substrate surface (when $R = 0$) cannot be measured, since the answer will always be infinity. Therefore it is necessary to carry out the calculations, only at points away from the point source ($R > o$).

4.3. Analytical Results and Discussion

Computer programs were used in these theoretical calculations. All the calculations were carried out using approximate values of the physical properties of high strength steel, as given below.

$k = 42\ \mathrm{J\ s^{-1}\ m^{-1}\ K^{-1}}$

$c = 691.0\ \mathrm{J\ kg^{-1}K^{-1}}$

$\rho = 7874\ \mathrm{kg\ m^{-3}}$

$T_m = 1400\ °\mathrm{C}$

Since the electron beam to material energy transfer efficiency is very good (Strutt 1980), the reflectivity of the beam at the surface of the material was assumed to be negligible.

Fig. 4.2a shows the temperature variation at points, which are on the path of the beam but at different depths below the surface. Computer program 'Heat 1' (vide appendix 1) was used to obtain these curves. As the beam approaches the point, the temperature gradually increases, reaching a maximum when the beam is at the surface directly above the point. As soon as the beam moves away, the temperature rapidly drops with time due to the rapid cooling caused by the steep temperature gradient between the melted region and the solid substrate. For a constant power, the maximum temperature at points below the surface decreases with the increasing depth below the surface. In the particular heat flow centre shown in fig.4.2a, a 300W power beam input was used with a traverse speed of 4.4 cm s^{-1}. The depth being nearer to the surface, curve 1 shows a maximum temperature of 1998°C, which is well above the melting point of the material. The maximum temperature of curve 2 is 1400°C, which was considered as the melting point. Therefore at the beam power and speed used, maximum depth of the melt is $\sim 200\mu m$. Curve 3 shows that the process parameters used were not able to melt

400µm depth below the surface, the maximum temperature at that depth rising only to 668°C.

The approximate heating and cooling rates at those points are shown in fig.4.2b, the positive values being the heating rates and the negative values, the cooling rates. For the same power input, the points nearer to the surface reach higher temperatures, therefore the temperature gradients at those points are greater than at points well below the surface, resulting in a higher cooling rate near the surface. Fig.4.3 shows how the cooling rate at a point 0.01mm depth below the surface varies with the temperature. Each cooling rate was calculated using the program 'Heat 2', (vide appendix 1), at a value of time corresponding to the cooling part of the heat cycle, but very near the peak temperature, at which the cooling rate was to be determined.

The variation of the theoretical melt depth with power input is shown in fig.4.4a. Melt depths were determined as a function of power input using the program 'Heat 1'. The melt depth was taken as the distance along z direction (at y = o) from the surface to the point, at which the temperature was equal to the melting point of the metal. It can be seen that the melt depth increases as the power is increased. The variation of experimental melt depth with power is shown in fig.4.4b. Experimental results show the same tendency of increasing melt depth with power.

The difference in experimental melt depths for constant increments of power, gradually decreased as the beam power was increased. In the range of power from 900 - 1100 W, the melt depth changed very little. This tendency can be explained, in terms of an increasing amount of vapourisation at higher temperatures. Once the metal is melted, the melt depth is not affected by an increase of beam power in a small range, since the latent heat of vapourisation is absorbed for the

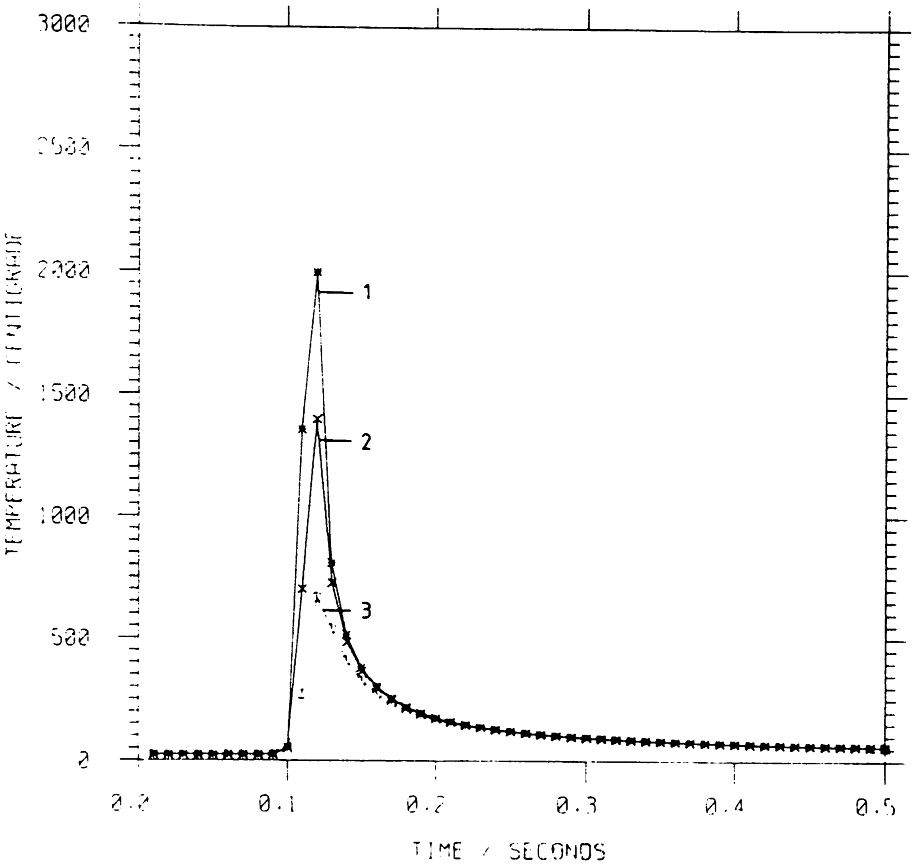

Fig.4.2 a.

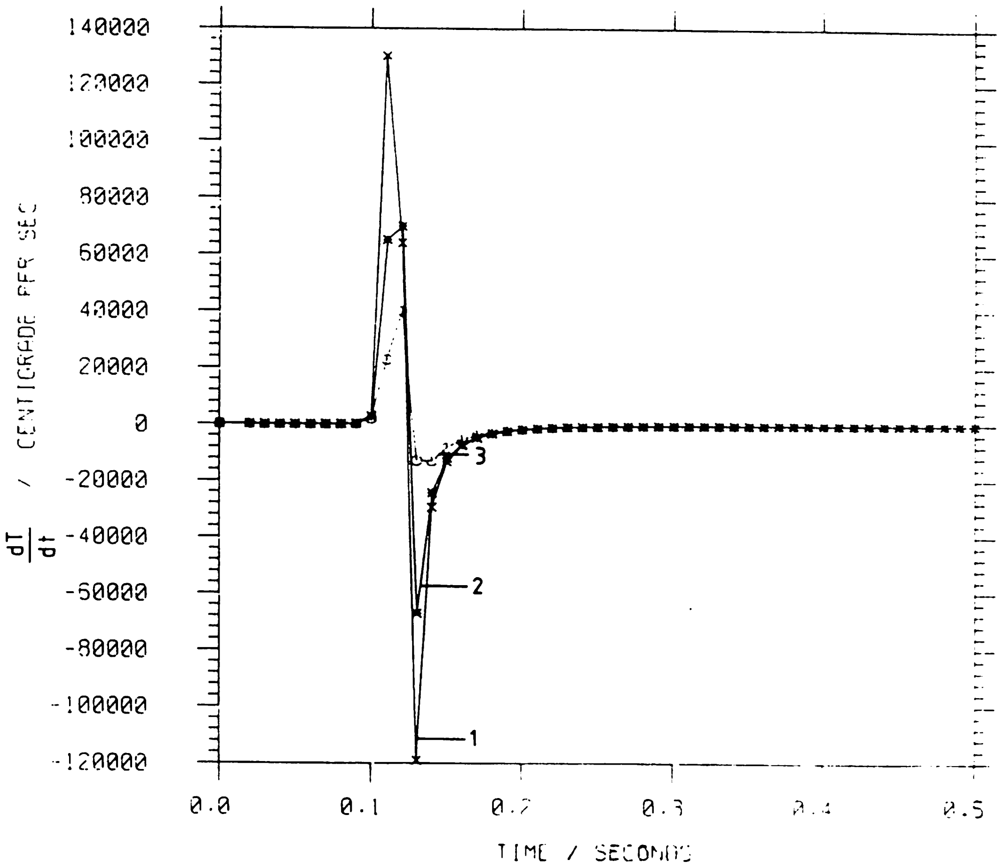

Fig.4.2b.

Fig.4.2. a) The temperature variation at points, which are on the path of the beam but at different depths below the surface.

1) 50 µm. 2) ~200 µm 3) 400 µm

b) The approximate heating and cooling rates at those points. (Beam power = 300 W, traverse speed = 4.4 cm s^{-1}).

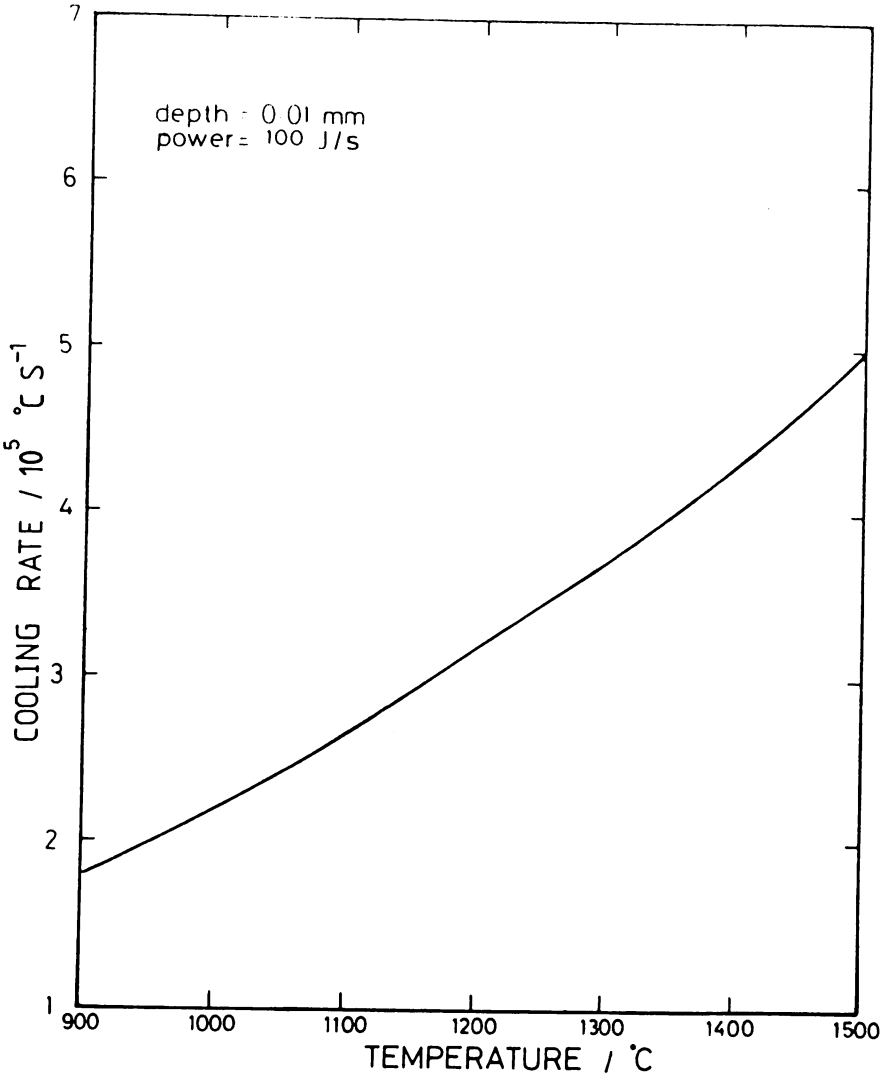

Fig.4.3. The variation of the cooling rate with the temperature, at which the cooling rate was determined.

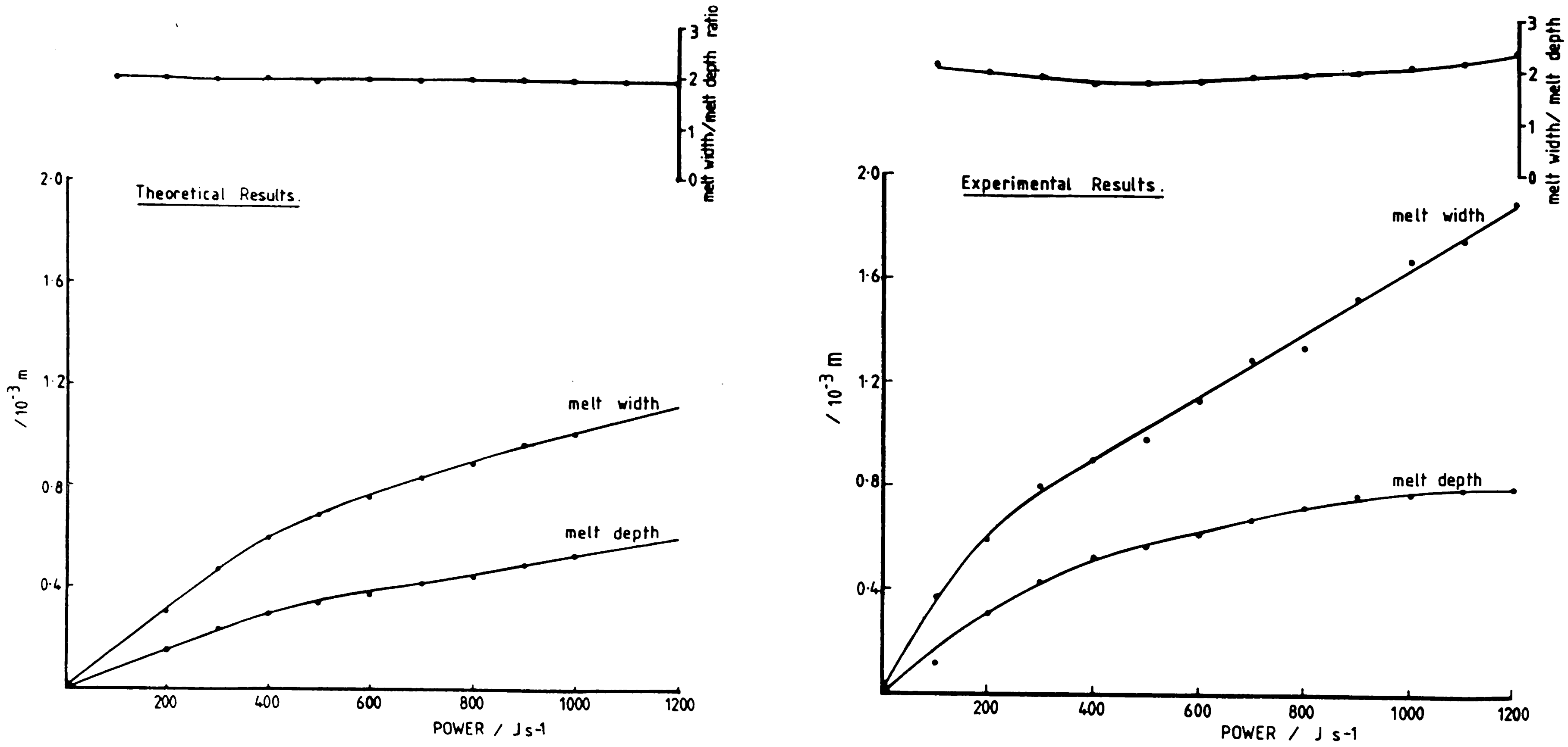

a.

b.

Fig.4.4. The variation of the melt depth, melt width and the melt width/melt depth ratio with increasing, a) theoretical and b) experimental power inputs.

vapourisation of the material at the surface. If the increase in power is sufficient enough to vapourise a considerable amount of material the melt depth will be increased (keyhole effect, Mazumdar and Steen 1980), but since the maximum power obtained by the modified electron beam welder is only 1200W, further experiments could not be carried out. No limit on the melt depth was observed theoretically due to the fact that the latent heat of boiling or vapourisation was not taken into consideration.

Fig.4.4a and b also show how the width of the melt pool increases with theoretical (P_{Th}) and experimental (P_{Ex}) power inputs. Computer program 'Heat 3' (vide appendix 1) was used to calculate the widths theoretically. The tendency of increase in power to give an increasing width of the melt pool is similar for both P_{Th} and P_{Ex}. The difference between the theoretical and experimental values of melt depths and widths are due to the assumptions, such as constant thermal characteristics of the material, made in the theoretical calculations. Since a point source has a constant area, when the power is increased theoretically the effect is similar to an increase in power density. However, since the beam diameter was not measured at different power levels, it was not possible to determine the power density experimentally. Fig. 4.5 shows how the strength of the point source (P_{Th}) and experimental power input (P_{Ex}) increase to give an increasing width of the melt pool. Fig. 4.6 shows the relation between P_{Th} and P_{Ex} needed to produce the same melt width (x). The values of x (variable), P_{Th} and P_{Ex} for the graph 4.6 were obtained from the curves of fig.4.5. Ideally, the values of P_{Th} and P_{Ex} to produce the same melt width should be the same and should have followed the dashed line in fig.4.6, but P_{Th} and P_{Ex} still show a direct linear relationship, confirming that an increase of P_{Ex} is actually an increase of the power density.

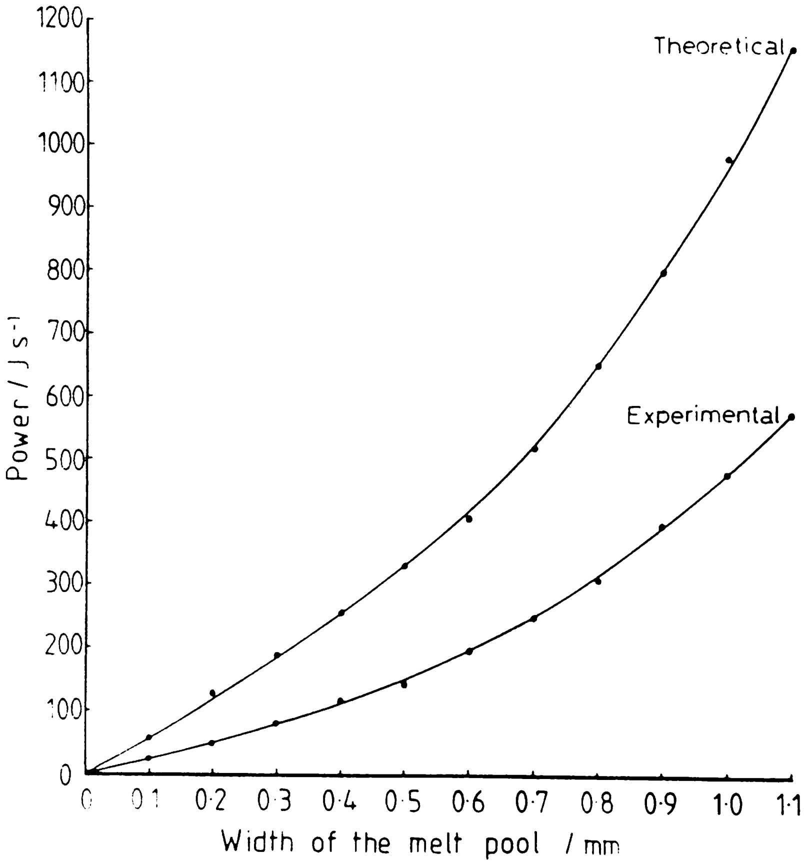

Fig.4.5. The variation of the width of the melt pool with theoretical (P_{Th}) and experimental (P_{EX}) inputs.

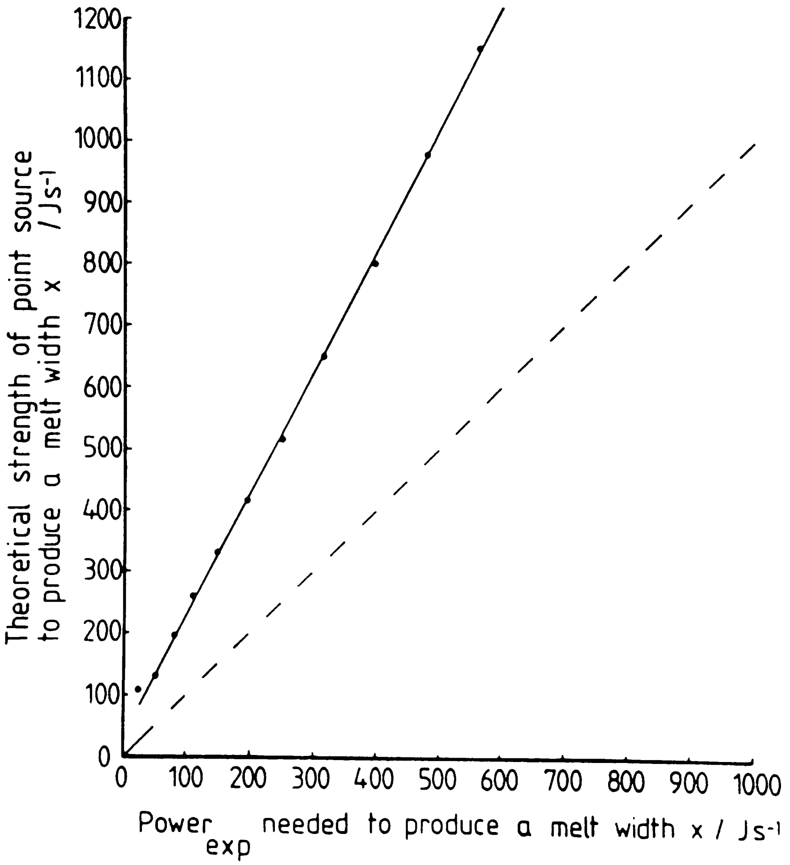

Fig.4.6. The relation between P_{Th} and P_{EX} needed to produce the same melt width x.

When the beams of very high energies are used, it is known that the melt depths increase considerably. The material at the surface vapourises rapidly resulting in an increase of the melt, just underneath the beam, downwards and thus makes a fine hole into the substrate. This effect is called the keyhole effect. (Mazumdar and Steen, 1980). Since only very thin surface layers were needed to be treated, rapid quenching experiments in the present work were carried out only with low power electron beams, thus avoiding the keyhole effect.

Since a point source of heat, used in Rosenthal's theory would give a semi-circular melt pool, there is a question of the validity of the application of this theory to rapid quenching. However, at the beam powers used in the experiments, the values of melt width to melt depth were about 2. Fig.4.4 shows the melt width to melt depth ratios obtained at different power inputs. In the range of power used, the experimental ratios were approximately the same as the theoretical ratios. The increase in the experimental ratio in the power range of 1000 - 1200 W was a result of the constant melt depth observed in that range, probably due to the onset of surface vapourization. Thus it was observed that at low powers, electron beam quenched areas were approximately semi-circular in shape. This observation confirmed that the use of Rosenthal's theory in the present work was justified.

Fig. 4.7 shows the variation of the theoretical cooling rate with depth below the surface as a function of the beam power. It should be noted that these curves were obtained using a constant traverse speed of 4.4 cm s^{-1} and that the cooling rate was measured at 1400°C, the melting temperature of the material. Computer program 'Heat 2' (vide appendix 1) was used to calculate the cooling rates. These curves show that at a certain power input of the beam, the cooling rate decreases as the depth below the surface increases. This characteristic was described earlier. (fig.4.2b). Another important observation is that at a constant traverse speed, the cooling rate at a certain depth below

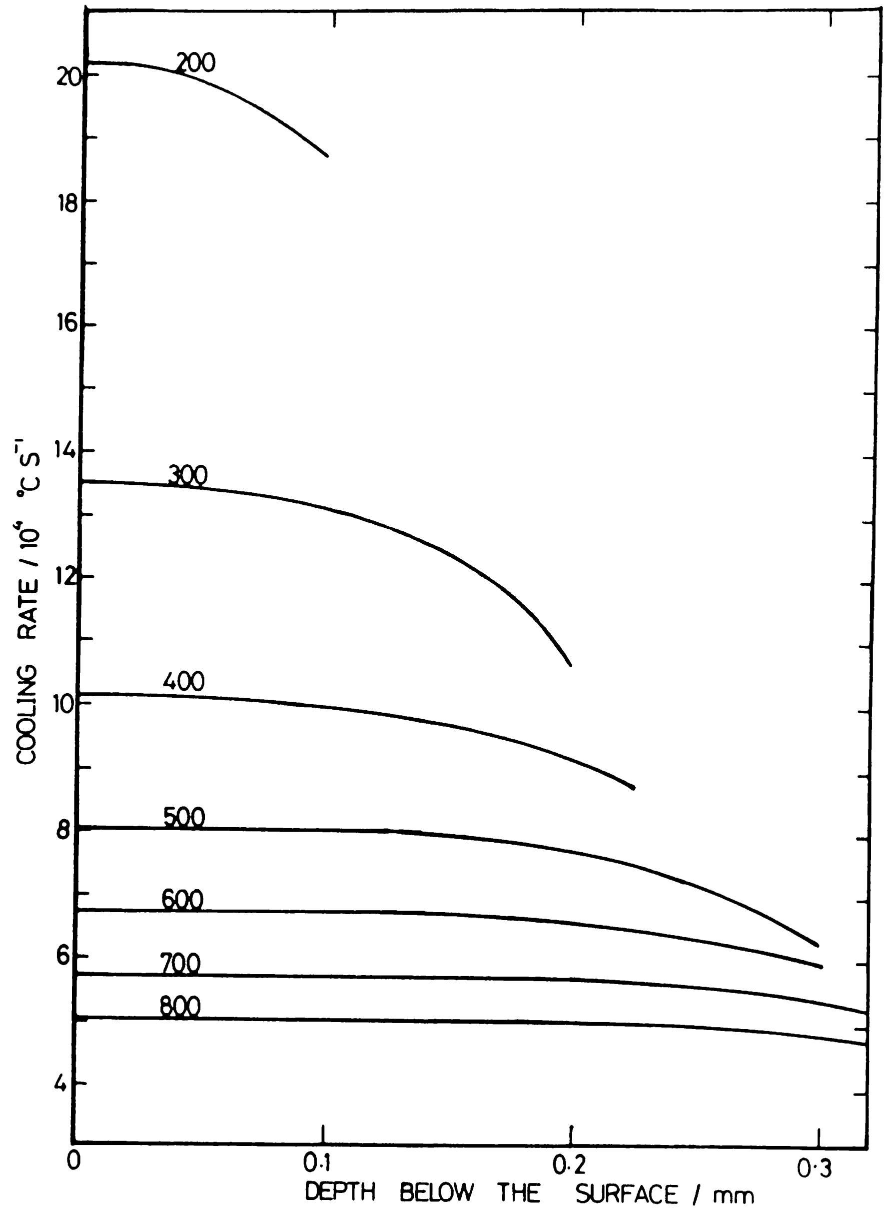

Fig.4.7. The variation of the theoretical cooling rate with depth below the surface, as a function of the beam power.

The cooling rate was measured at 1400 °C, the melting temperature of the material.

the surface decreases with increasing power. The increase in the amount of heat which should be transferred to the solid substrate causes this decrease in the cooling rate at higher power inputs. The experimental observations will be discussed in detail in chapter 5.

4.4. Conclusions

1. Heat flow distribution and cooling rate depend on process parameters such as beam power and beam or traverse speed.
2. For the same power input and traverse speed, cooling rates at points nearer to the surface are higher than those at points at greater depths.
3. At a constant traverse speed, melt depth increases with increasing beam power but at a constant power input, melt depth decreases with increasing traverse speed.
4. At a constant traverse speed, the cooling rate at a point below the surface increases as the power input decreases.
5. Despite the assumptions made for theoretical calculations, theoretical results were in good agreement with experimental results.
6. In the range of process parameters used in the present experiments, the application of Rosenthal's theory of heat flow to electron beam surface quenching process is valid.

CHAPTER 5.

5. Electron Beam Rapid Quenching of Metals.

5.1. Ultra High-Strength Steel

5.1.1. As Received Condition.

In the as received condition from RARDE, Fort Halstead (Vide section 3.1), the ultra high-strength steel consisted of a martensite microstructure formed by tempering at 620°C. Fig.5.1 shows an electron micrograph of a typical microstructure, which mainly consists of lath martensite with molybdenum carbides (Mo_2C). The relatively coarse cementite dispersions, which are formed during quenching and auto-tempering are usually replaced by a much finer alloy carbide dispersion as a result of the secondary hardening treatment at 620°C. Fig.5.2a is another bright field electron micrograph showing Mo_2C carbide in martensite. The corresponding centered dark field micrograph of the same area, illuminating the carbides is shown in fig.5.2b. Ultra high-strength steel in this as received condition had a microhardness of about 350 VPN.

5.1.2. The Dendritic Nature of the Surface Melted Region.

Samples of steel in as received condition were subjected to electron beam rapid quenching. The experimental details are described in chapter 3.

In the transverse and longitudanal cross sections of the electron beam rapidly quenched steel, the melt zone and the heat affected zone (HAZ) can be readily distinguished from the substrate (fig.5.3). The resolidified regions consist of a highly refined microstructure. Due

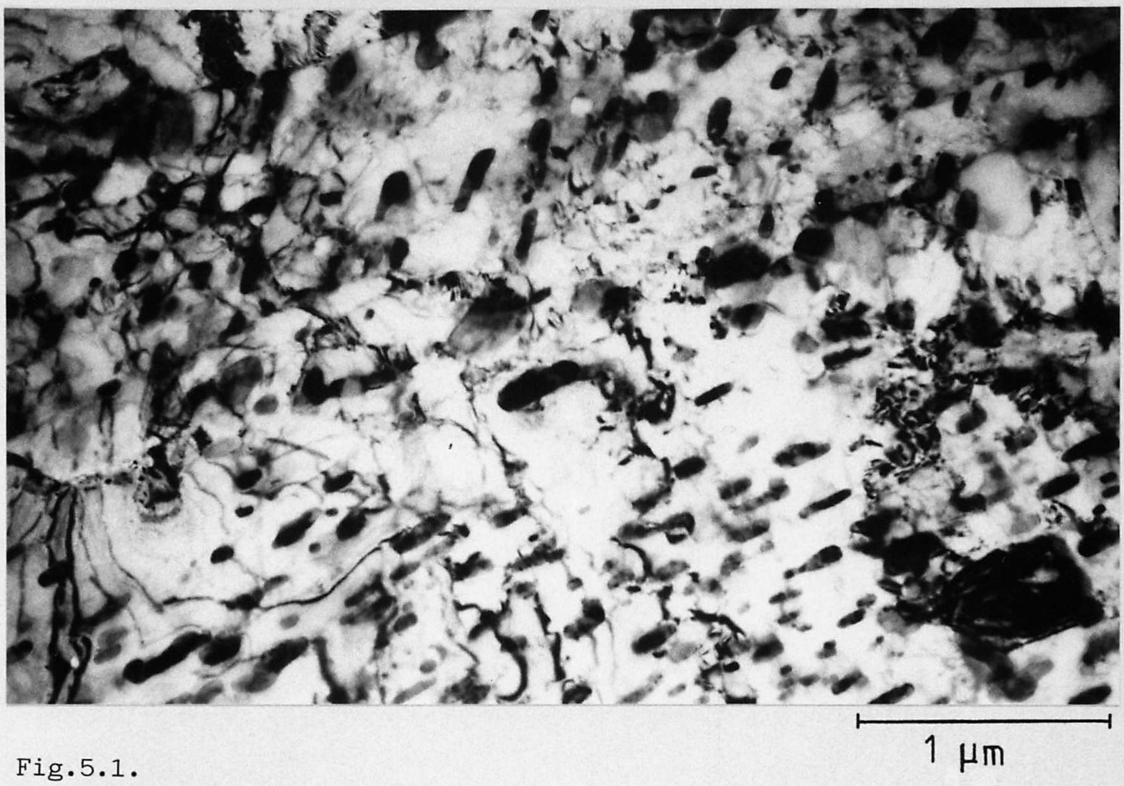

Fig.5.1.

Microstructure of the ultra high-strength steel in the as received condition, showing tempered martensite with Mo_2C carbides (TEM).

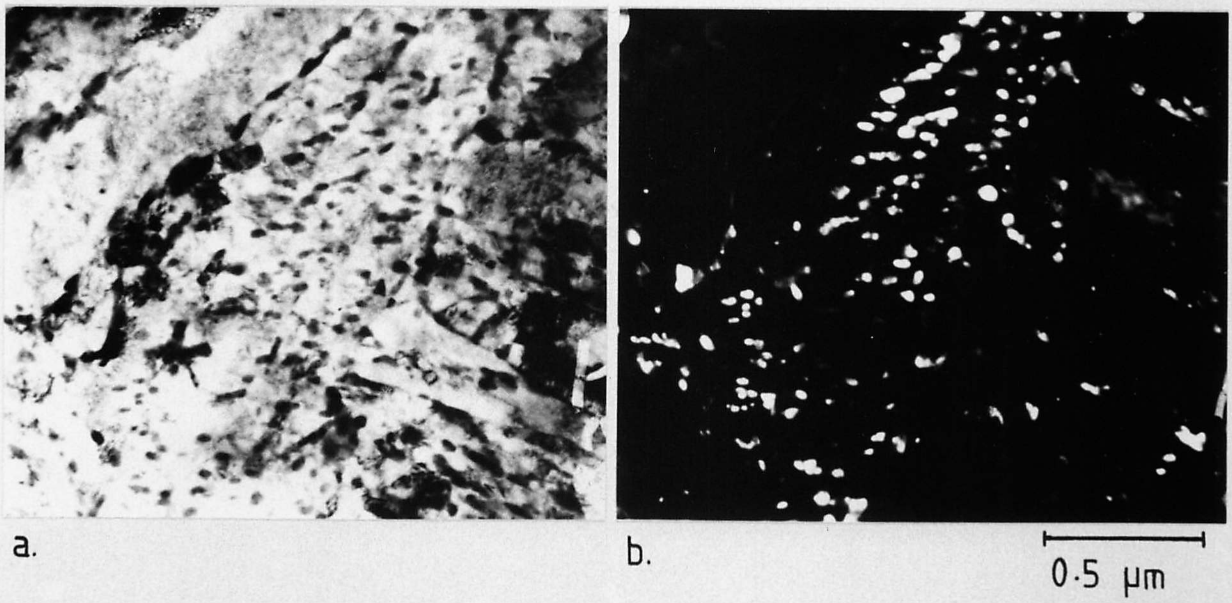

Fig.5.2. a) Bright field b) dark field pair of Mo_2C carbides in martensite observed in the as received microstructure (TEM).

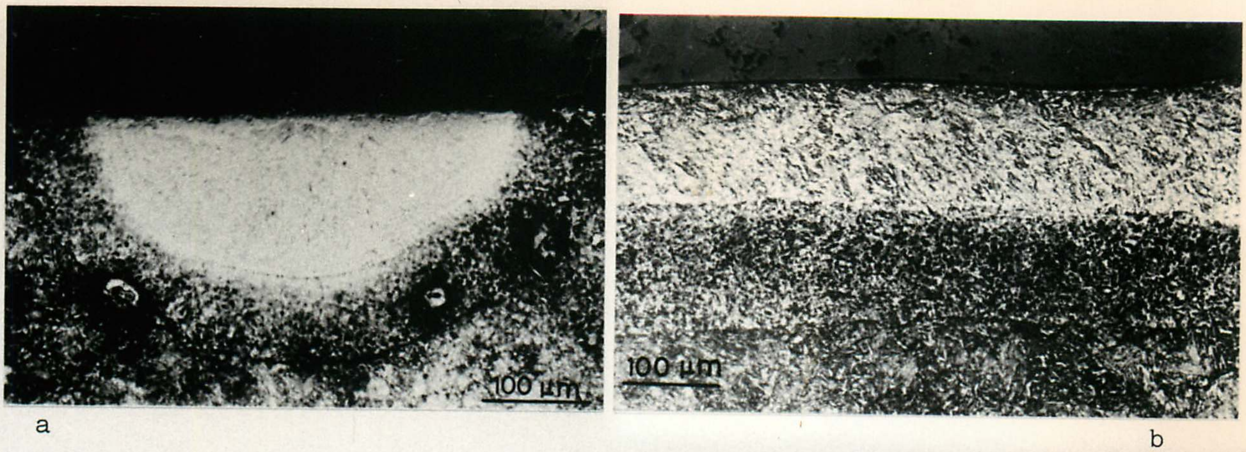

Fig.5.3. a) transverse and b) longitudinal cross sections of the electron beam rapidly quenched regions and the heat affected zones of steel. Beam power = 100W, Traverse speed = 4.4 cm s^{-1} (Optical micrographs)

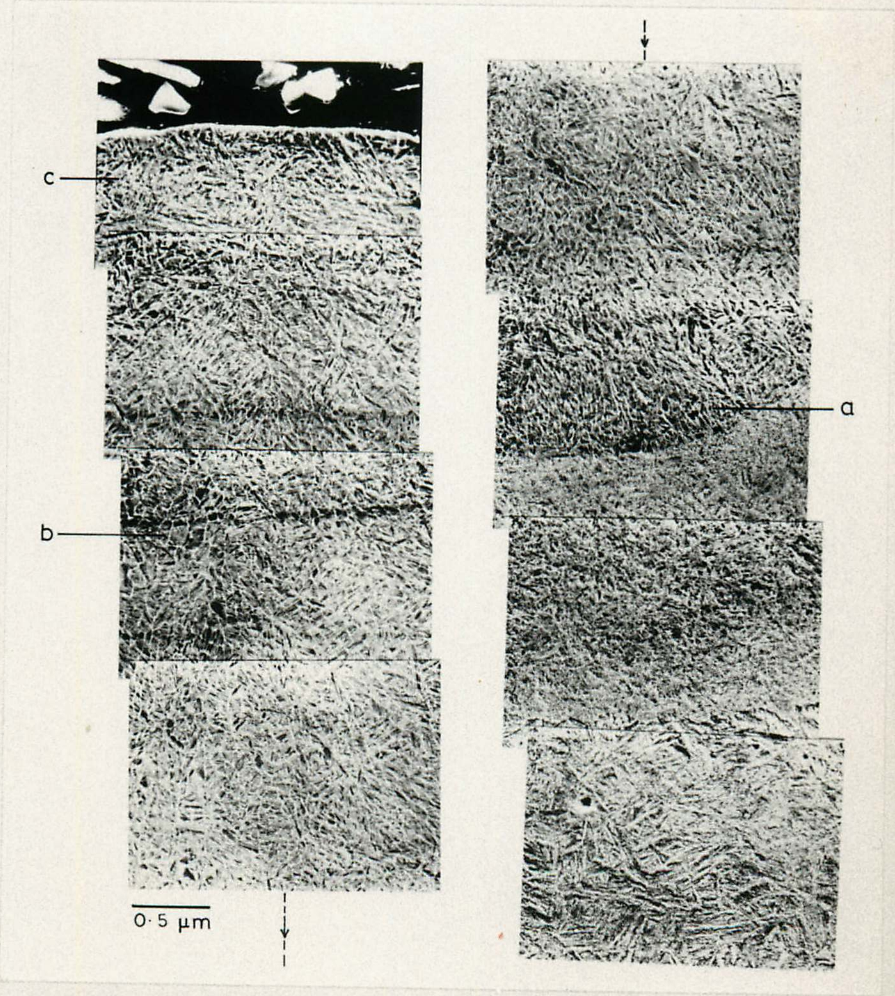

Fig.5.4. A transverse cross section of an alectron beam rapidly quenched region at a higher magnification. (Only a strip from the surface to the substrate is shown here).(Optical micrograph)beam power = 50W, Traverse speed = 29.6 cm s^{-1}.

to the very high quenching rate and low alloy content of the steel, the microstructure consists of very fine dendrites and it is difficult to clearly observe the dendrites by light microscopy (fig.5.3).

The martensitic nature of the steel after melting and re-solidifying is clearly distinguishable in the scanning electron micrograph of a melted region (50W beam power and 29.6 cm s^{-1} traverse speed) shown in fig.5.4. It was observed that a thin area (marked a in fig 5.4. adjacent to the heat affected zone was on a particularly refined scale, because the cooling rate in this region would be expected to be similar to that of a chilled zone of a solidifying ingot. From this region columnar dendrites grew into the melt. Apart from these columnar dendrites, the re-solidified region also consisted of cellular dendrites. The presence of cellular and columnar dendrites is typical of laser and electron beam melted zones and is very pronounced in eutectic alloys (Copley et al 1978) and nickal base superalloy single crystals (Narasimhan et al 1979).

5.1.3. Cooling Rate

A linear relation between dendrite arm spacing in the solidification structures and the solidification time has been reported by Flemings (1966). Working on aluminium-copper alloys he showed that

$$d = 7.5\ \theta_f^{0.39} \qquad 5.1$$

where, d = dendrite arm spacing in microns

and θ_f= freezing time in seconds

(the meaning of θ_f has not been clearly defined but it seems that it is the time taken to completely freeze a certain volume of liquid metal)

Dean and Spear (1966) related dendrite cell measurements to solidification rate (average rate of cooling from just above the liquidus to just below the liquidus) and showed that this relationship is independent of composition. Based on Flemings results, and dendritic cell sizes of 400 mesh aluminium-copper powder and aluminium splats, Dean and Spear suggested that a curve (dendrite cell size vs average cooling rate) based on data from normal cooling rate (200°C s^{-1}) solidification experiments could be extrapolated to deduce the quench rates involved in rapid quenching work. Matyja, Giessen and Grant (1968) measured the spacings of dendrites using electron microscopy based replica techniques. With the corresponding cooling rates deduced from previous measurements of Predecki et al. (1965) and calculated values of Ruhl (1967), Matyja et al showed that the data for the splat cooled aluminium based alloys fitted well on the extrapolated curve of Dean and Spear (1966). The relationship between dendrite spacing, a and cooling rate, r was thus given as

$$d.\ r^{a} = C \qquad 5.2$$

where $a = 0.32$

and C = constant.

This relationship is claimed to be valid over a span of 10 orders of magnitude.

In laser or electron beam melting of surfaces, experimental measurements of the cooling rate is extremely difficult due to the nature of the very thin melted region involved, but since the dendrite spacing can be measured without much difficulty, the above relationship is potentially useful in determining the cooling rates involved. In cross sections of laser melted tool steel, Kim et al. (1979) found that the mean cell diameter was ∿1-2 μm and on the basis of the above relationship, the cooling rate was estimated to be $\sim 10^5 °C s^{-1}$ which is approximately the same as the value deduced from a heat transfer analysis.

In the rapidly quenched ultra high strength steel of the present work, a variation of the dendrite spacing was observed within the melted regions. In the particular rapidly quenched region, shown in fig.5.4, the average diameter of cellular dendrites near the surface was about 0.4μm (area c), while that of the cellular dendrites below that layer (area b) was about 0.75μm. According to the relationship between the dendrite spacing and the cooling rate (see fig.5.5), these measured dendrite spacings correspond to cooling rates of $\sim 2 \times 10^6 °C\ s^{-1}$ at the surface and $2.4 \times 10^5 °C\ s^{-1}$ in the middle of the melt pool.

5.1.4. Microstructural Comparisons with Melt Spun and Solid State Quenched Steel.

Optical microscopy, electron microscopy and X-ray diffraction studies of electron beam quenched steel were carried out with the objective of defining the microstructure produced by this method of rapid quenching. The microstructure of conventionally solid state quenched (austenitised at 1200°C for 1 hour and quenched in iced brine) was also studied for comparison. The microstructure of the surface melted steel was also compared with that of the melt spun steel.

5.1.4.1. Grain refinement.

A major observation was the relative refinement of the rapidly quenched microstructure. The solid state quenched sample exhibited prior austenite grains which contained differently oriented packets of martensite laths. The average grain size was about 75μm. Figures 5.6,

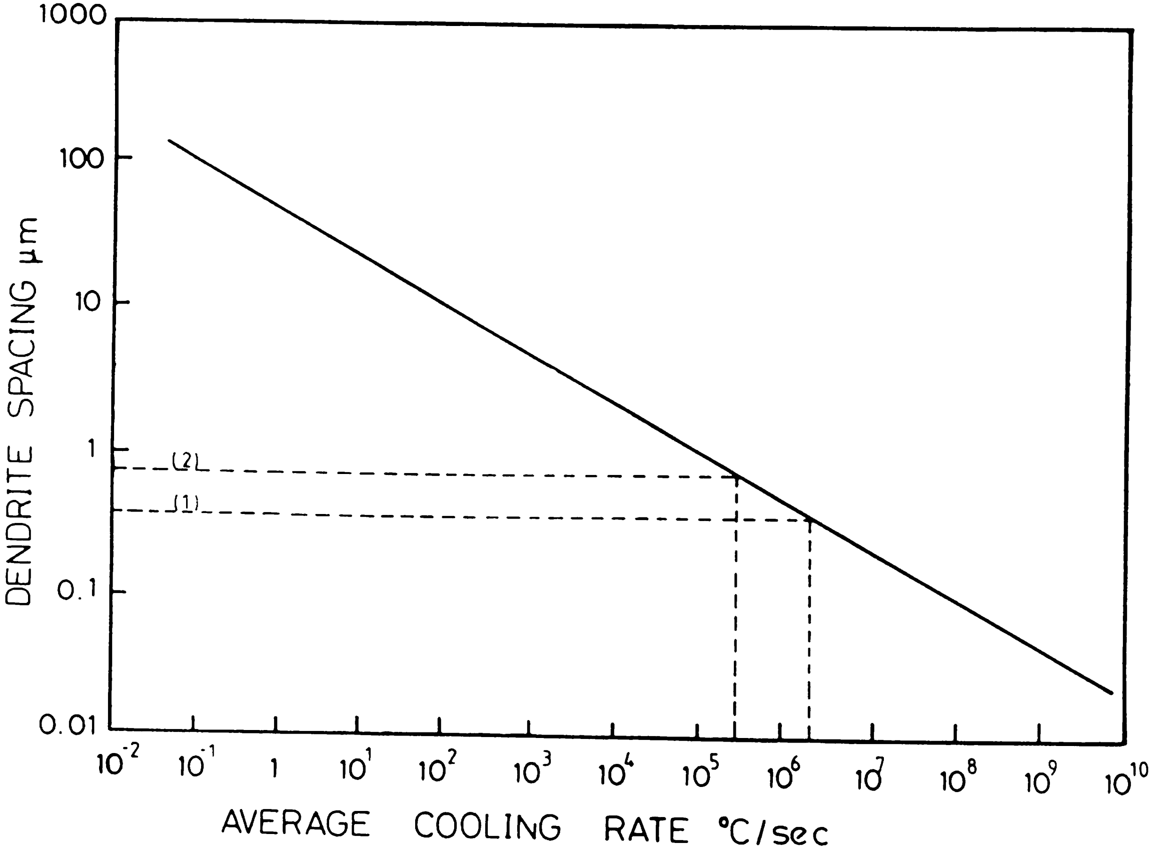

Fig.5.5. The relationship between the dendrite spacing and the average cooling rate. (After Matyja et al). Results of the present work are shown in dashed lines.

1. near the surface, up to ~ 0.1µm depth.
2. at about 3µm depth.

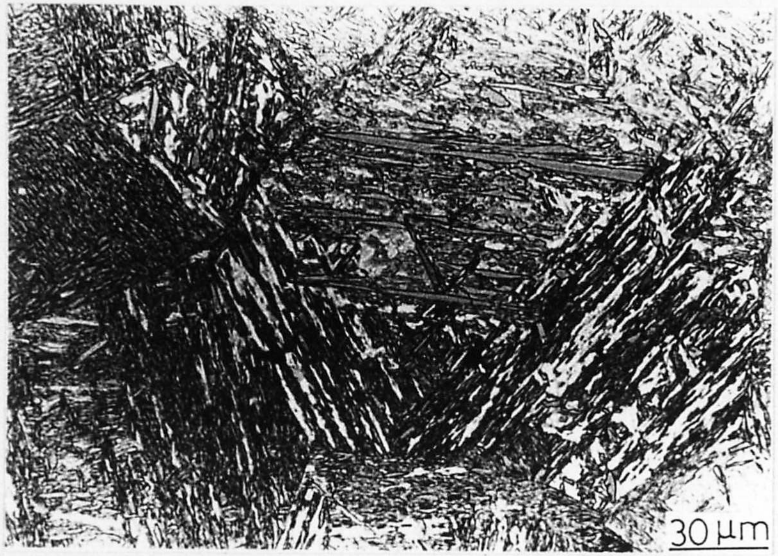

Fig.5.6. Microstructure of solid state quenched steel (optical micrograph)

Fig.5.8. Microstructure of melt spun steel (optical micrograph)

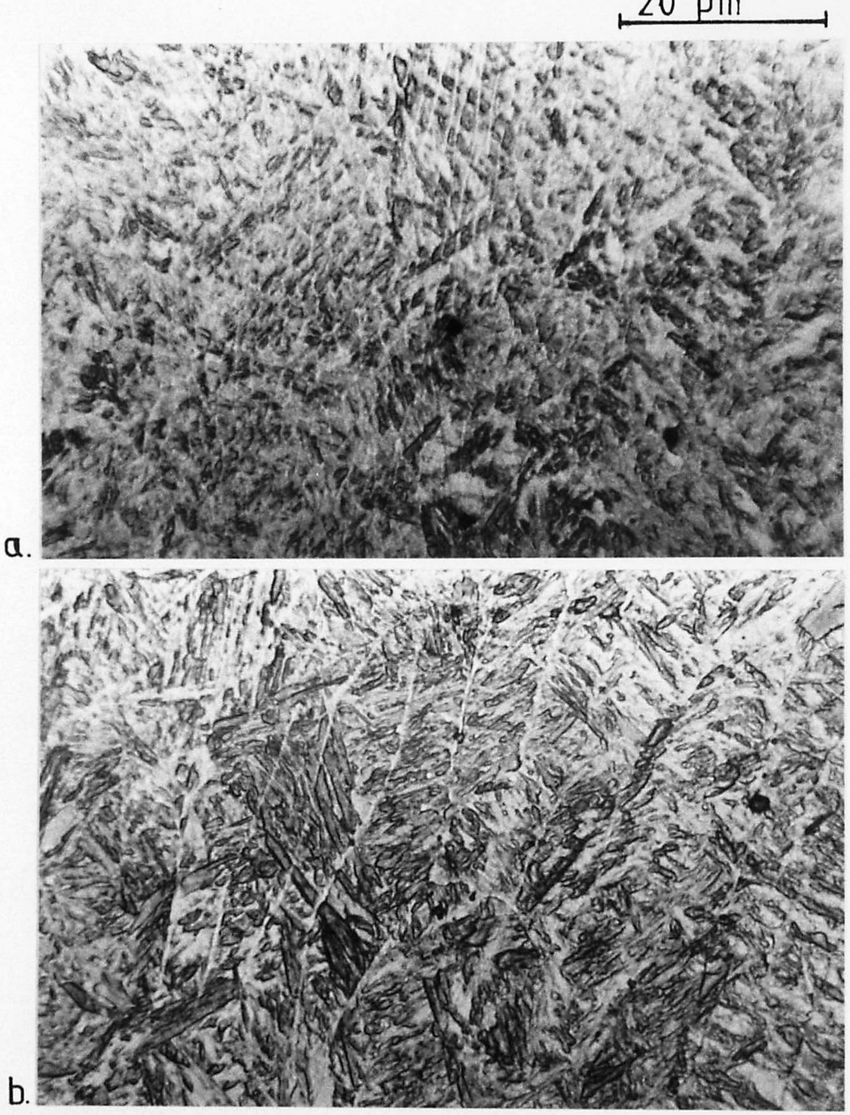

Fig.5.7. Microstructures of eletron beam rapidly quenched steel. Optical micrographs.
a) 100W beam power, 4.4. cm s^{-1} traverse speed.
b) 1200W beam power, 4.4. cm s^{-1} traverse speed.

5.7 and 5.8 are optical micrographs of solid-state quenched, electron beam quenched and melt spun steel structures respectively. At these magnifications, it is difficult to determine the exact nature of the martensite reaction products in rapidly quenched structures, although it appears to consist of martensite plates ∿1-3μm wide, together with a fine unresolved structure. It was not possible to determine the prior austenite grain sizes of the rapidly quenched structures but it is clear that the average size of the martensite units in the solid state quenched structure is larger than those in the rapidly quenched structures. Since the austenite grain size determines the maximum size of a martensite plate, it is reasonable to assume that the rapidly quenched structures consisted of a smaller prior austenite grains. Duflos and Cantor (1978) have considered the martensitic plate width itself as the effective grain size in martensitic structures, but the grain size is more likely to be larger than a plate width.

The grain refinement achieved in rapid quenching has been reported by many workers. Splat quenching techniques frequently produce mixed grain sizes but usually in the range of 0.1 to 10μm (Honeycombe 1978). Breinan and co-workers (1975) found that the microstructure of laser melted nickel base super alloys was highly refined, while Kim and co-workers (1979), Strutt and co-workers (1979) and Molian (1981) observed grain refinement in electron beam surface melted tool steels.

It is believed that the main reason for the fine grain size is the high quench rate involved. Based on a homogeneous nucleation solidification model, Boswell and Chadwick (1977) demonstrated a strong dependence of grain diameter $d_{'}$, on the cooling rate, R.

$$d_{'} = 1.75 \times 10^{7} . R^{-0.9} \qquad 5.3$$

The effect of cooling rate on the microstructure is also shown in fig. 5.7a and 5.7b, which are the microstructures of electron beam surface melted steel at a constant traverse speed but with beam powers of 100W and 1200W respectively. As described in chapter 4, increasing beam power at a constant speed decreases the cooling rate. It can be observed in fig.5.7 that the average size of martensite plates and the width of the columnar dendrites have decreased when a low power beam was used clearly showing the effect of increasing cooling rate.

Refinement of the grain size is one of the important strengthening mechanisms in the heat treatment of steels. According to the Hall-Petch relationship (Hall 1951, Petch 1953) the finer the grain size of a material, the higher the resulting yield stress.

$$\sigma_y = \sigma_o + K_y d^{-\frac{1}{2}} \qquad 5.4$$

where σ_y = yield stress

d = grain diameter

σ_o and K are constants

Apart from the prior austenite grain size, the fine structure of martensites also contributes to the strength. The small individual plates as well as the lath substructure are obstacles to dislocation movement contributing to overall strength (Honeycombe 1981). This increase in strength caused by rapid quenching was demonstrated by the fact that the microhardness of rapid quenched steel was nearly twice that of the solid state quenched steel. Microhardness will be discussed in detail in section 5.1.4.5.

5.1.4.2. Martensite morphology

By transmission electron microscopy studies, the rapidly quenched microstructures were found to consist mainly of dislocated martensites, and some of the martensite plates exhibited twinning. The microstructures observed in both electron beam treated and melt spun steels were similar. Figures 5.9 and 5.10 show bright field electron micrographs of the martensite structure observed in the surface melted steel. The apparent widths of these plates varied from 50nm to about 250nm. Thin foil preparation of surface melted steels was very complicated and difficult. High quality electron micrographs were obtained from the thinned melt spun steel ribbons. Figures 5.11 and 5.12 show the martensite units observed in melt spun microstructures. The apparent widths of these plates are in the range of 20 - 150nm.

The martensite plates in the surface melted steel were often twin oriented and a large amount of plates were internally twinned. These internal twins were very fine (apparent width of some of the twins <10nm). Figures 5.13 and 5.14 show the typical internal twins found in the surface melted steel. Although a few internal twins were found in solid state quenched steel, the presence of a large amount of twins in rapidly quenched structure indicated that rapid quenching of materials favoured the formation of twinned martensite plates. It seems that the martensite morphology does not depend on the process used for rapid quenching. The melt spun ribbons of ultra high-strength steel also contained internally twinned martensite plates. Fig. 5.15a is centred dark field micrograph of internal twins in a martensite plate found in melt spun structure and was typical of many such observations. These

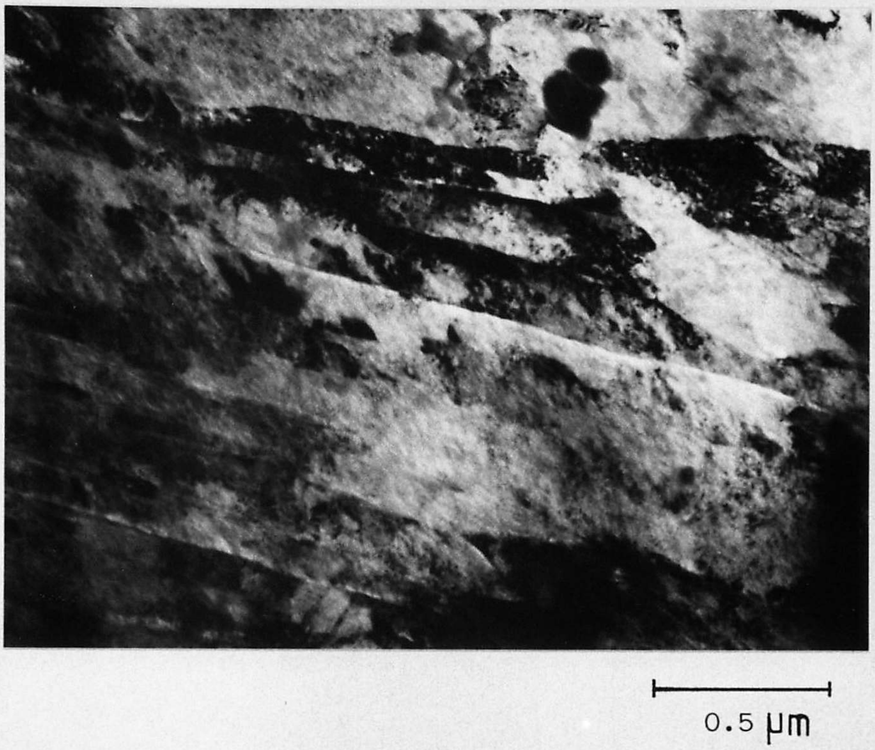

Fig.5.9. Martensitic microstructure in electron beam rapidly quenched steel (TEM)

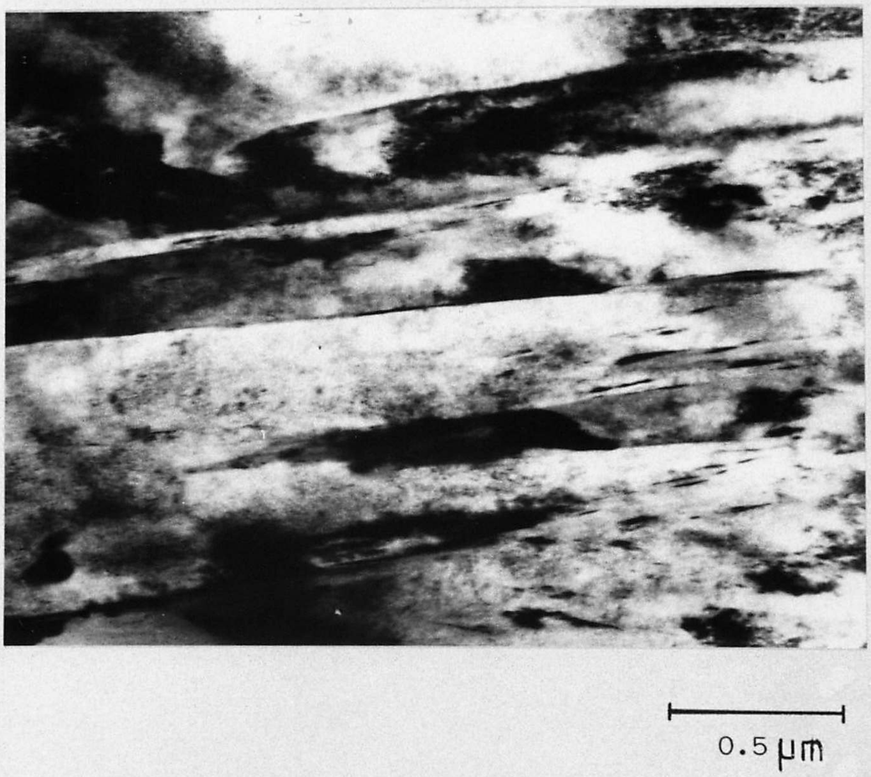

Fig.5.10. Martensitic microstructure in electron beam rapidly quenched steel (TEM).

Fig.5.11 Fig.5.12

Figs.5.11. and 5.12. Martensitic units observed in melt spun microstructures. Numbers marked, only show the different units. (TEM)

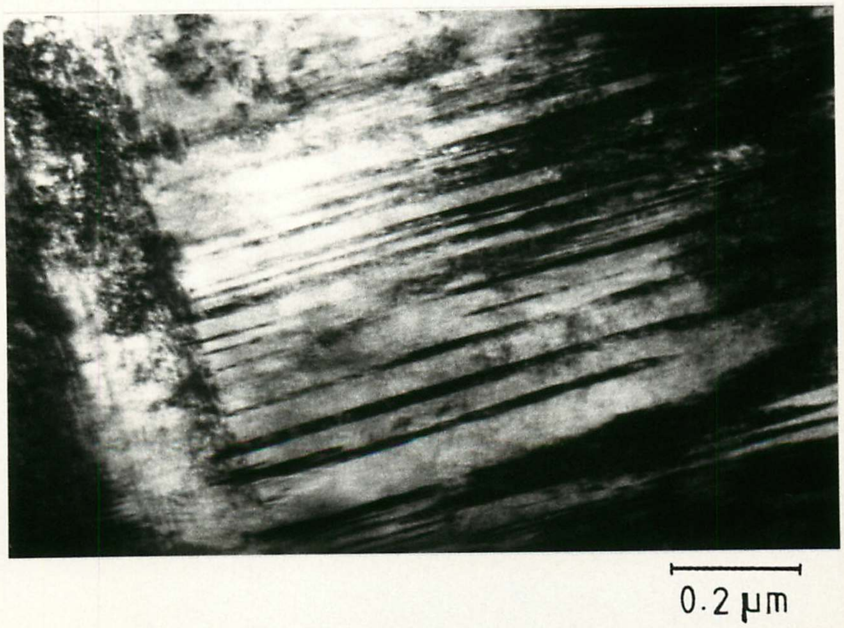

Fig. 5.13. Internal twins found in an electron beam surface melted region.

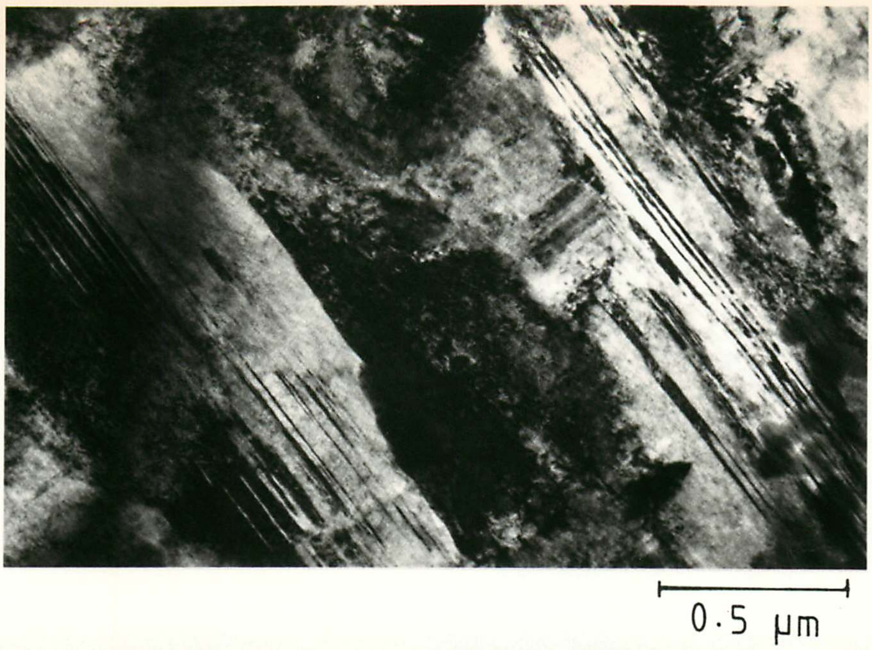

Fig.5.14. Internal twins in martensites, observed in another area of surface melted steel. (TEM)

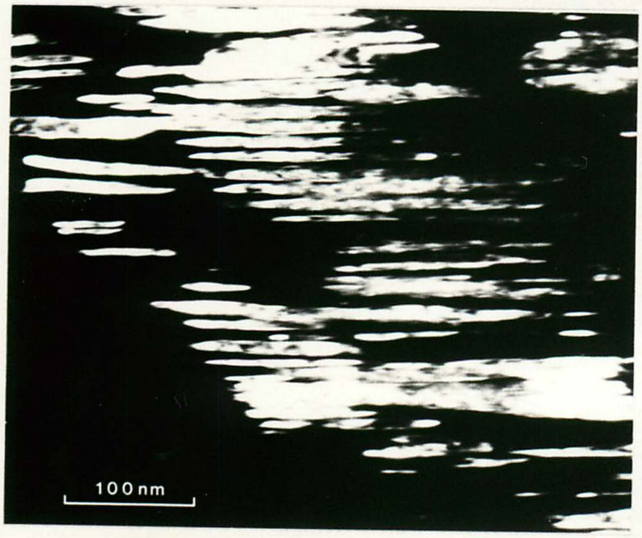

Fig.5.15a.
A centred dark field micrograph of internal twins in a martensite plate found in melt spun steel

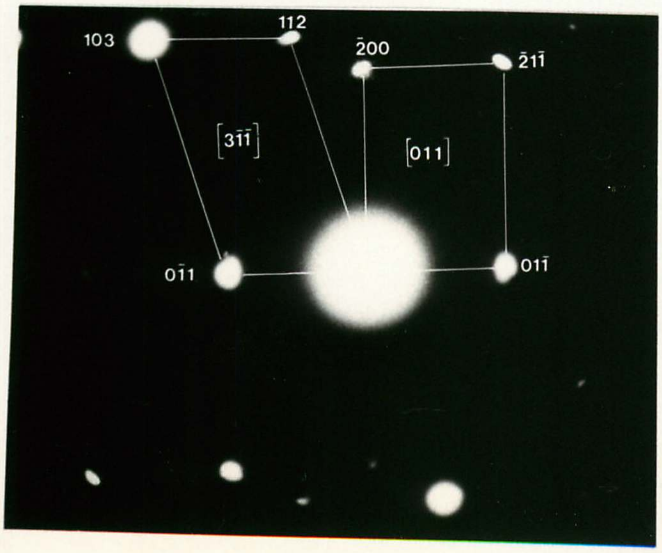

Fig.5.15b.
The diffraction pattern of the area shown in fig. 5.15a showing the martensitic orientations.

twins were also very fine (∿10nm width). The diffraction pattern of this area showing the martensite orientations is shown in fig.5.15b. The axis angle pair is <011> /66° which is reasonably approximate to the ideal <011> /70.52° within the experimental errors.

The reason for the changes in the martensite morphology may be attributed to the high quenching rates. Working on Fe-Mo-C alloys, Sare and Honeycombe (1978) found that after solid state quenching and relatively slow liquid-state quenching (rate $\sim 10^3 - 10^4$ Ks^{-1}) martensite had a lath morphology but after rapid quenching (splat cooling with cooling rate $> 10^6$ Ks^{-1}) martensite had a twinned plate morphology. The change in martensite morphology occurs due to the influence of the cooling rate on the martensite transformation temperature (M_s), which in fact, is related to the Critical Resolved Shear Stress (CRSS) for slip or twinning. Thomas (1971) suggested that the high quenching rates increased the solute content by inhibiting alloy carbide precipitation and this increase in the solute content in turn lowered the M_s temperature. In iron base alloys M_s temperature have been found to be depressed by rapid quenching. Ruhl and Cohen (1969) reported a depression of M_s in splat quenched Fe-Ni-B alloys. Later, Inokuti and Cantor (1976) showed that the M_s temperature of Fe-Ni alloys was also depressed by rapid quenching. The most plausible explanation for the presence of twinned plate martensites in rapidly quenched materials is the one which relates the M_s depression with the CRSS. Thomas (1971) described this phenomenon using a diagram (fig.5.16), which shows the schematic variation in CRSS with temperature for slip and twinning. During rapid quenching, at the lowered M_s temperature, the CRSS for twinning is lower than that for slip, thus allowing twinning to occur as it is the preferred shear mode for the transformation.

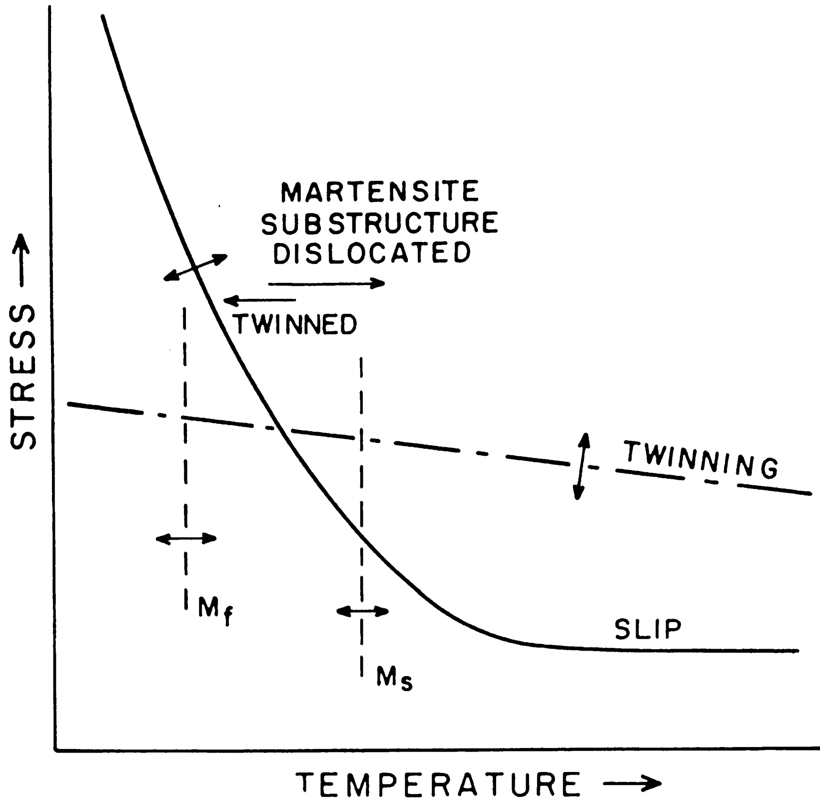

Fig.5.16.

The variation of the Critical Resolved Shear Stress with temperature for slip and twinning of martensite.

(after Thomas, 1971)

The structure of the solid state quenched steel was found to comprise, almost entirely, of lath martensites, which had a larger apparent average width (0.1 - 0.5μm) than those found in melt spun or electron beam quenched structures (Figures 5.17 and 5.18). The solid state quenched structure shown in fig.5.18 contains a large autotempered lath about 5μm wide.

5.1.4.3. Retained Austenite

Retained austenite was detected as interlath films in both electron beam quenched and melt spun microstructures. Most of the retained austenite was fragmentary in nature. Fig.5.19 is a 002_γ centred dark field electron micrograph showing some of the retained austenite found in electron beam quenched steel. An example of retained austenite found in melt spun steel structure and the selected area diffraction pattern are shown in fig.5.20. The centred 220_γ spot of the diffraction pattern was used to illuminate retained austenite in this instance. Both these figures (5.19 and 5.20) show that austenite was not uniformly retained between laths but was present as fragments.

Where sufficient diffracted intensity from the austenite was detected, it was possible to define the austenite/martensite crystallography. Fig.5.21 also shows the discontinuous nature of the retained austenite found in melt spun steels. Crystallographic relation detected from the selected area diffraction pattern showed that

$$(1\bar{1}1)_\gamma \quad // \quad (110)_\alpha$$

and

$$[\bar{1}01]_\gamma \quad // \quad [\bar{1}11]_\alpha$$

confirming that the austenite and martensite were related approximately (within the limitations of the techniques used) by the Kurdjumov-Sachs relationship (1930), which is frequently found in solid state quenched steels.

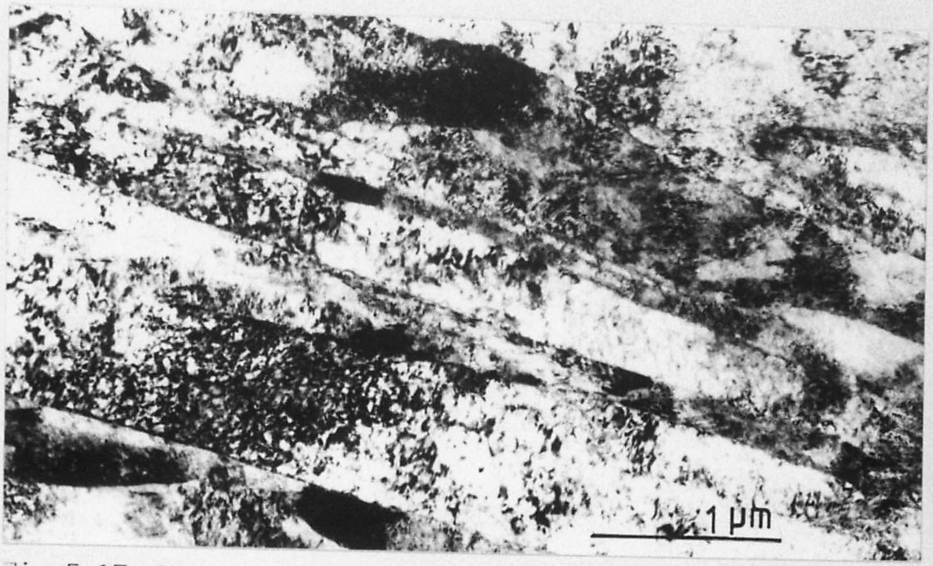

Fig.5.17. Martensite laths in solid-state quenched steel. (TEM)

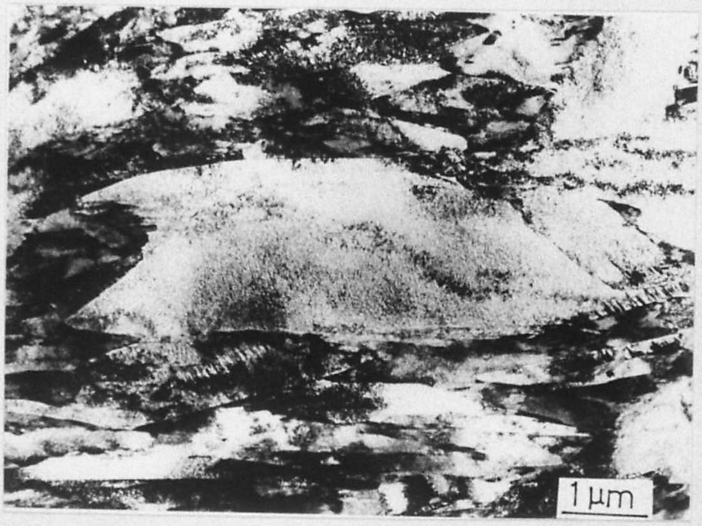

Fig. 5.18. Martensite laths including a large autotempered lath in solid state quenched steel. (TEM)

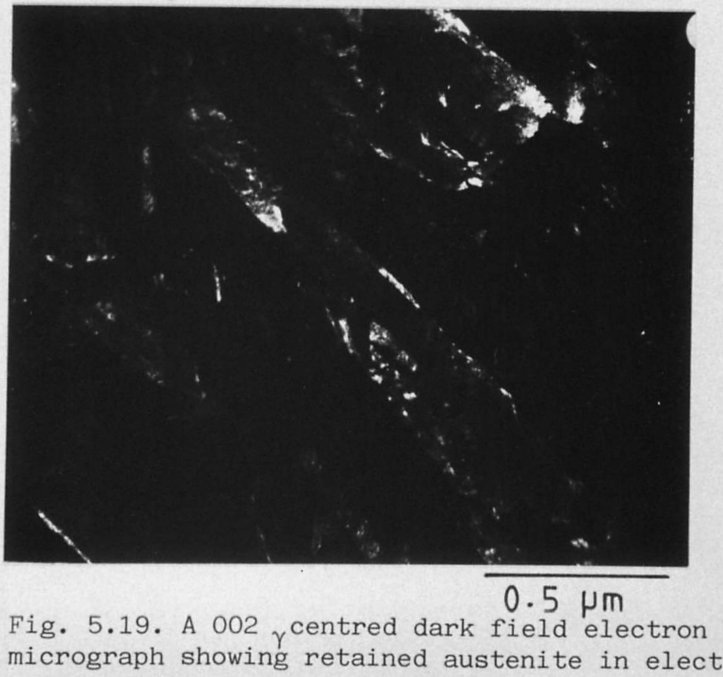

Fig. 5.19. A 002$_\gamma$ centred dark field electron micrograph showing retained austenite in electron beam rapidly quenched structure.

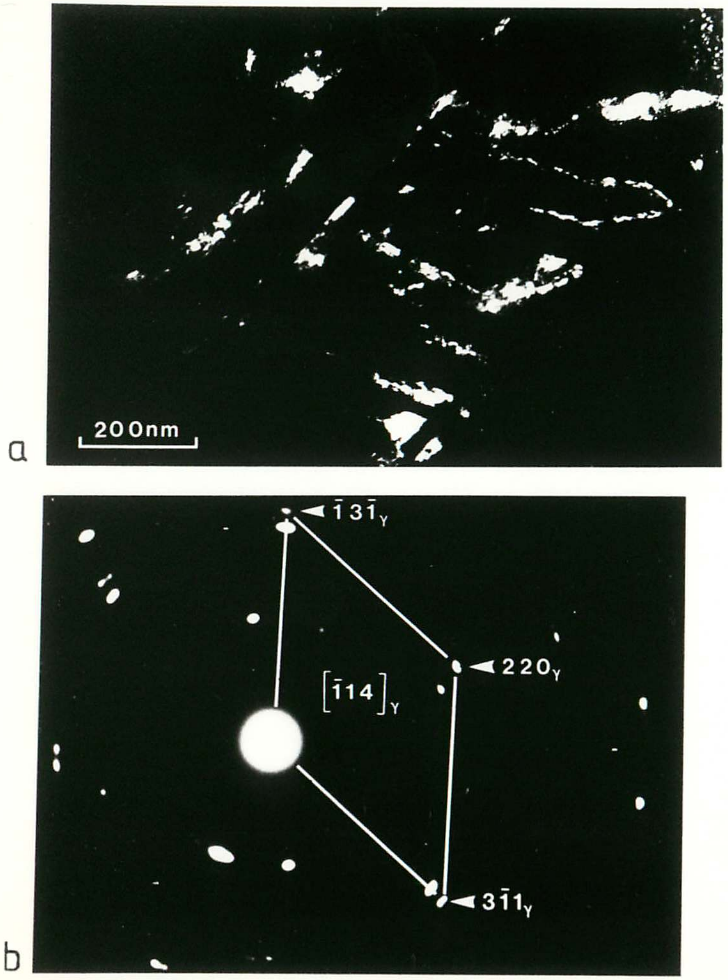

Fig. 5.20.
a) A centred dark field electron micrograph, showing retained austenite in melt spun steel.
b) Corresponding selected area diffraction pattern. 220_γ spot was used to illuminate re-austenite.

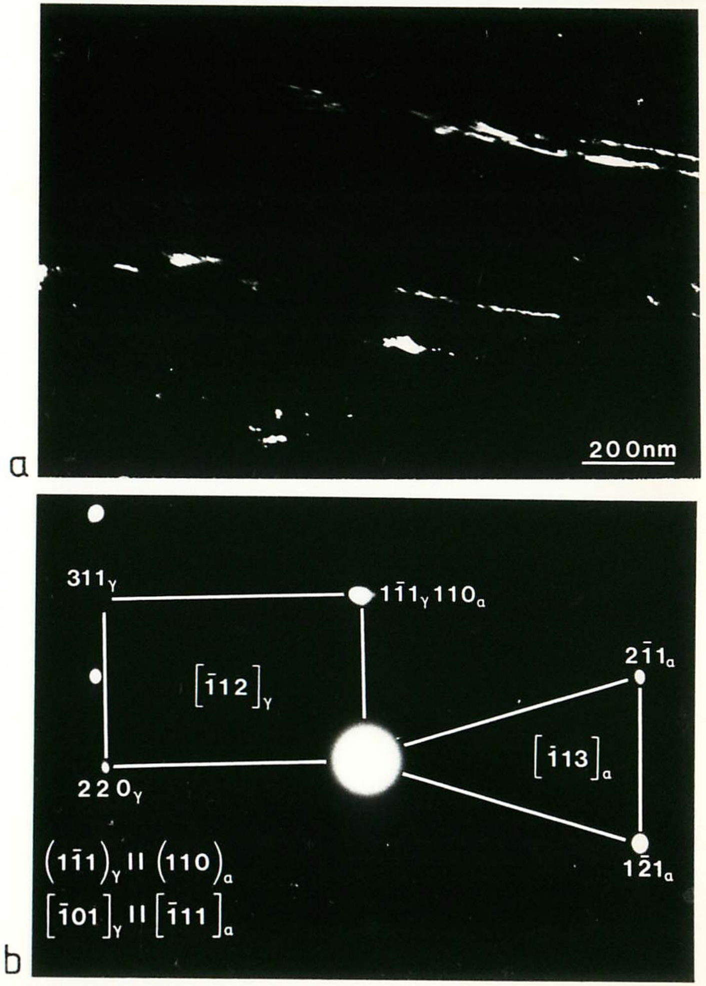

Fig. 5.21.
a) Retained austenite found in another area of melt spun steel (Dark field electron micrograph)
b) Corresponding selected area diffraction pattern. Kurdjumov-Sachs relationship detected between martensite and austenite orientations is also shown.

The fragmentary nature of the retained austenite is a result of the twinned martensites present in the microstructure. A similar result was found by Bhadeshia and Edmonds (1979) in their work on Fe-4Ni-0.4C alloy (solid state quenched), where it was observed that adjacent laths were twin related. Usually in solid state quenched steels, when the martensite laths are low angle related, the retained austenite is continuous in character. (e.g. Bee et al. 1979 , Law et al. 1979). It has therefore been suggested (Bhadeshia and Edmonds 1979) that austenite which can be mechanically stabilised between low angle related laths, would be unstable between the twin related laths. This follows from the fact that twin units shear in opposite directions, so that they can form in a mutually self accommodating manner. In contrast, the shear accompanying the formation of similarly oriented laths will be additive and promote the stabilisation of the interlath austenite.

The X-ray diffractometer traces of solid state quenched, melt spun and completely electron beam melted surface of ultra high-strength steel are shown in figures 5.22, 5.23 and 5.24 respectively. No austenite was detected in solid state quenched structure by X-ray diffractometry, but rapidly quenched structres gave rise to small austenite peaks. Electron microscopy studies also revealed that the amount of retained austenite present in electron beam surface melted steels and melt spun steels were larger than in the solid state quenched steels.

The increase in the amount of retained austenite, which occurs during rapid quenching can be attributed to the increased solid solubility of the alloying elements and to the grain refinement. Based on experimental results, Thomas (1978) reported that if all the carbides were in solution, a fine grain steel would retain more austenite than a coarse grained steel. In fact the stabilization of austenite by closely spaced boundaries due to the prevention of growth

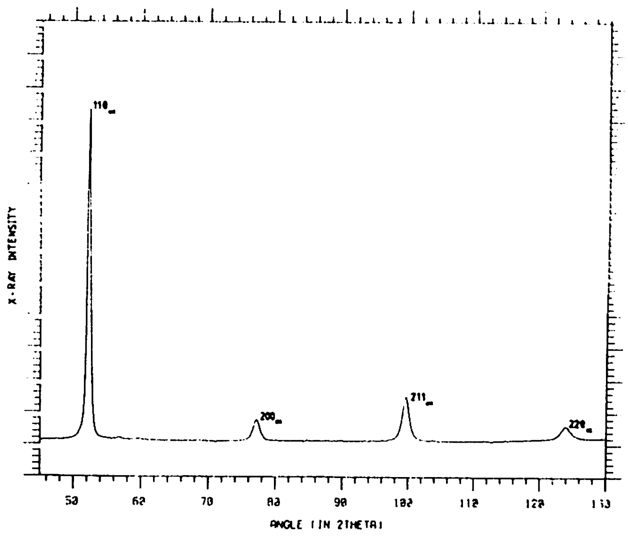

Fig. 5.22. X-ray diffractometer trace of solid-state quenched steel (CoK_α)

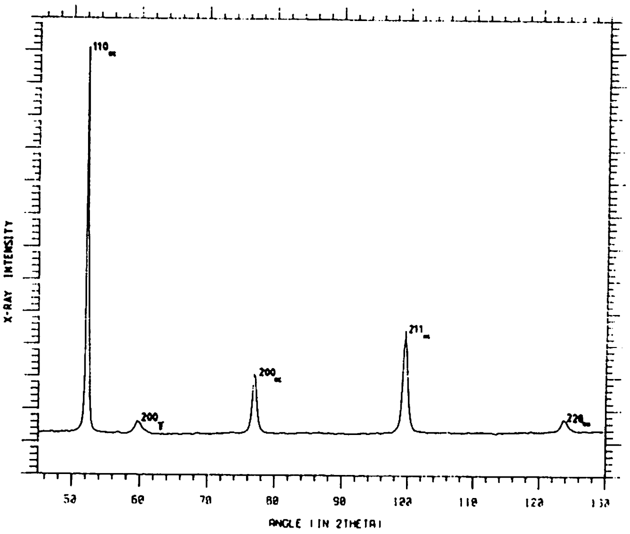

Fig. 5.23. X-ray diffractometer trace of melt spun steel (CoK_α)

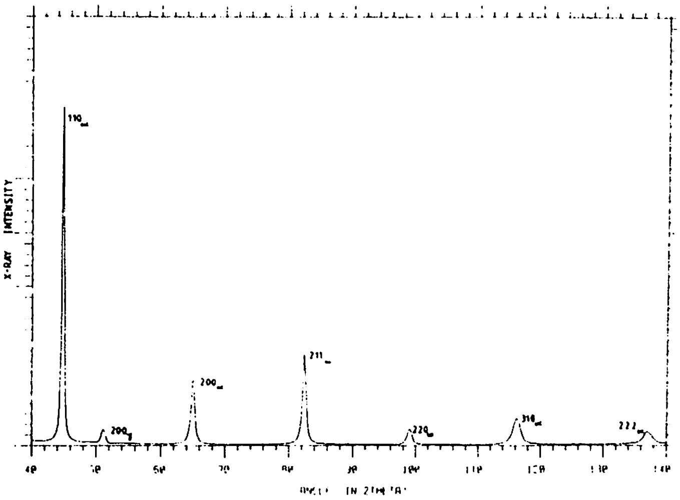

Fig. 5.24. X-ray diffractometer trace of completely electron beam melted surface. (CuK_α)

of martensite after nucleation was demonstrated earlier by Leslie and Miller (1964).

When the carbides and alloying elements are dissolved in solution, an increase in the retained austenite would occur, since the elements are free to stabilise austenite. Webster (1968) demonstrated that the increased solid solubility of alloying elements depressed the M_s temperature resulting in more retained austenite. Sare and Honeycombe (1975, 1978) and Kim and co-workers (1979) also have reported increases in solid solubility and the amount of retained austenite in splat cooled and electron beam surface melted tool steels. An increase in solid solubility, found in electron beam rapidly quenched and melt spun ultra high-strength steels of the present work is described in the next section.

5.1.4.4. Solid solubility

Autotempering was found to be virtually eliminated in the electron beam rapidly quenched steel in contrast to solid state quenched steel. No significant quantities of carbides were observed by electron microscopy. It was not possible to detect any carbides even by X-ray diffractometry (fig.5.24). probably overlap, The microstructure of melt spun high strength steel was also almost completely free of carbides. Fig.5.25 shows a rare observation of fine carbides in melt spun steel. Electron diffraction pattern of these carbides was consistent with cementite.

The observed lack of autotempering in rapidly quenched steel can be attributed to the high quenching rate, which inhibits carbide nucleation and growth. This inhibition leads to a greater supersaturation in rapidly quenched materials as observed by the measurements of the lattice parameters of martensites in solid state quenched and

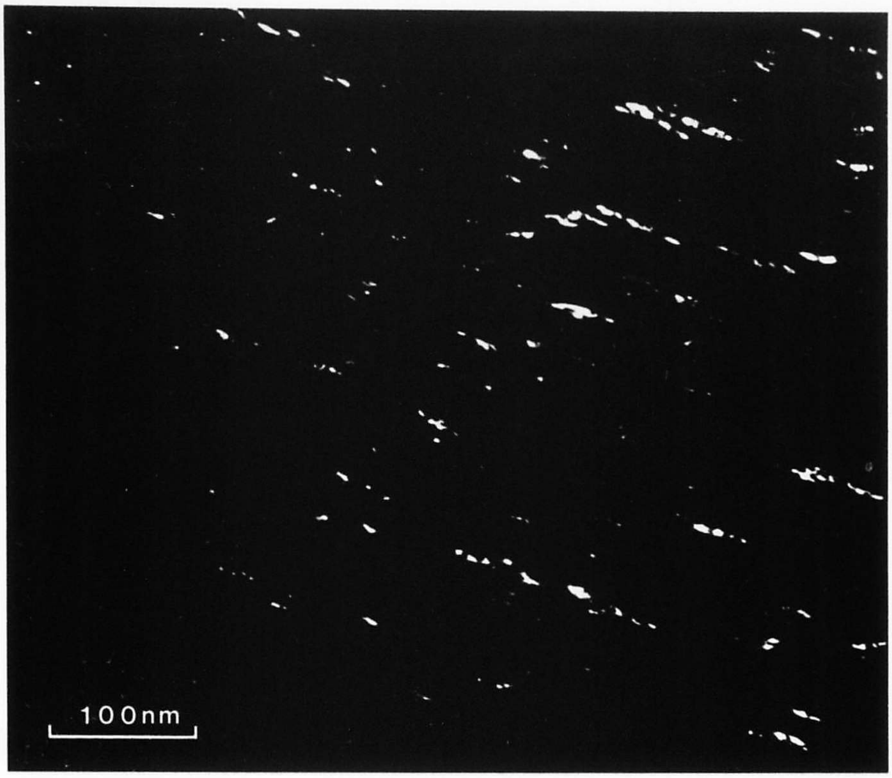

Fig. 5.25. Fine carbides observed in melt spun steel. (A rare observation - TEM, Dark Field)

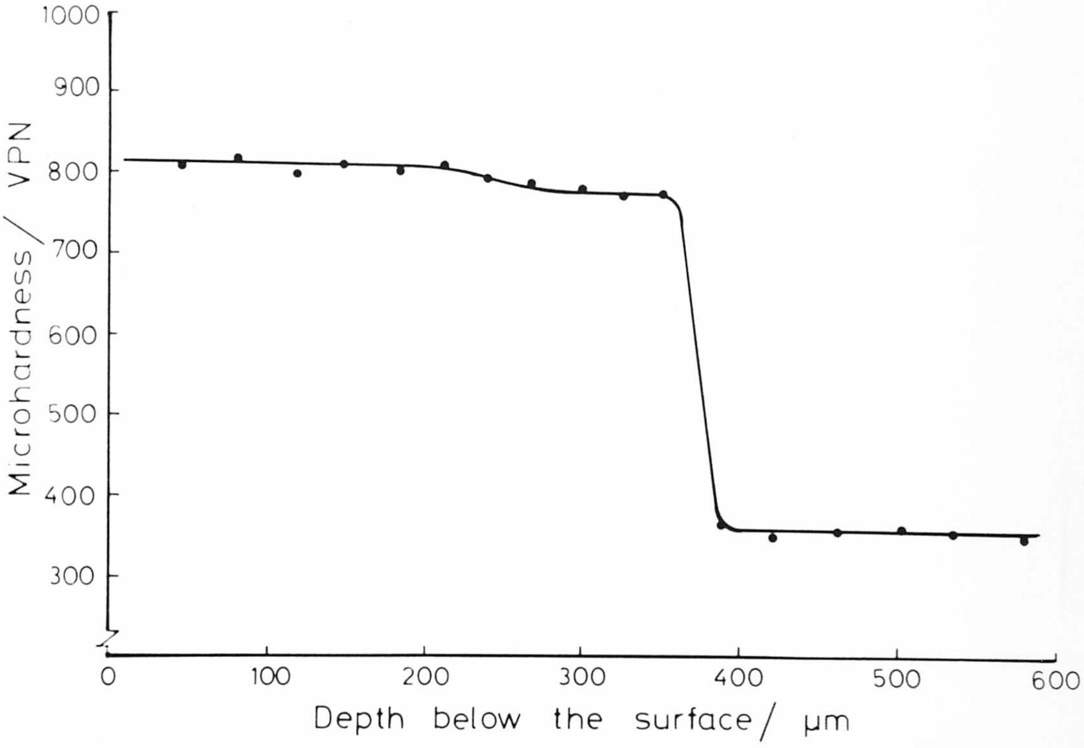

Fig. 5.26. Variation of microhardness with the depth below the surface in an electron beam melted region of steel.
Beam power - 200 W
Traverse speed - 4.4. cm s^{-1}

rapidly quenched steel (listed in table 5.1). It can be seen that even after allowing for the practical errors in measurement, the lattice parameters of electron beam quenched and melt spun steel are greater than that of the solid state quenched steel

Table 5.1.

Lattice parameters of Ultra High-Strength Steel.

condition	lattice parameter Å	X-ray wavelength (λ) Å
Solid state quenched	2.8690 ± 0.0012	Co K_α, 1.7902
Melt spun	2.8742 ± 0.0014	Co K_α, 1.7902
Electron beam rapidly quenched	2.8794 ± 0.0044	Cu K_α, 1.5417

The increased solid solubility, the increase in retained austenite and the enhancement of the amount of twinned martensites observed in rapidly quenched ultra high-strength steels are clearly all interlinked. The increase in supersaturation together with the refinement of the microstructure leads to a large increase in the microhardness of rapidly quenched steel and is described in the next section.

5.1.4.5. Micro-hardness

Rapid quenching of ultra high-strength steel has resulted in a considerable increase in microhardness. Fig.5.26 shows the variation of microhardness with the depth below the surface in an electron beam melted region of steel. The microhardness of the steel substrate was only ∿350VPN, but it increased up to 810 - 820 VPN when rapidly quenched. The heat affected zone had a microhardness, slightly lower than that of the melted region. Melt spun steel also showed a high microhardness of ∿800VPN as compared with that of ∿460VPN of the solid state quenched steel.

High hardness values obtained in rapidly quenched crystalline iron base alloys have been reported by several workers (Inokuti and Cantor, 1977 and Duflos and Cantor, 1978). This increase can be attributed to the grain refinement and to the increased solid solubility. In the present work, the rapidly quenched structures mainly consisted of fine scale martensites, presumably formed within small prior austenite grains. Although some retained austenite was also present, this mainly martensite structure is greatly responsible for the increase in microhardness. Inokuti and Cantor (1977) observed that when Fe-Ni, Fe-Mn and Fe-Ni-C alloys were splat quenched to give martensite, the microhardness obtained (∿ 700VPN) was very much greater than the corresponding solid state quenched alloys (∿250 VPN). On the other hand increasing the manganese content has been shown to lead to a relative decrease in microhardness

($\sim$400VPN) of splat quenched Fe-Mn alloy, due to an increase in the amount of retained austenite. In fully austenitic Fe-Ni and Fe-Ni-C alloys, the microhardness ($\sim$100 - 200 VPN) was independent of the quench rate since the retained austenite caused a sharp decrease in microhardness. Thus the small austenitic grain size produced by splat quenching high nickel alloys had been shown to have little effect on microhardness.

In contrast to the results of the present work and the earlier work mentioned above Ansell and Breinan (1965) have reported a decrease in micro-hardness of martensite with increasing cooling rate (in solid state quenched steels). Chilton and Kelly (1968) also suggested that the amount of autotempering, which occurs during cooling from the M_s temperature, decreased as the quenching rate increased, thus reducing the martensite hardness. However, in rapid quenching of materials, where martensite structures are observed, there are no reports to suggest a decrease in hardness with increasing quench rate, unless considerable amount of austenite is retained.

Inokuti and Cantor (1977) showed that the solid state quenched pure iron with a complete ferritic microstructure had a microhardness of $\sim$70VPN, whereas splat quenched pure iron could be ferritic with a hardness of $\sim$250VPN. These results can be interpreted as a consequence of the fine scale of splat quenched microstructure.

Thus, it can be concluded that the mainly martensitic microstructure together with the grain refinement caused a large increase in microhardness in the electron beam rapidly quenched ultra high-strength steel.

5.1.5. Topographical Characteristics and Melt Zone Geometry.

A main observation of the electron beam melted steel surfaces was the presence of ripples which had occurred during rapid solidifcation. Surface roughness depended upon process parameters such as the beam power and the traverse speed. On the rapidly solidified surfaces two ripple periodicities were evident; coarse ripples and finer ripples between them. At a constant power input, the mean spacings of both the coarse and fine ripples varied with the beam speed. When the power was increased at a constant traverse speed, the height of the central crest of the melted area increased and the troughs on both sides of the crest were deepened. Fig.5.27 shows a series of scanning electron micrographs of rapidly solidified surfaces using a 100W power beam, but with varying speeds. Decrease in the mean spacings and the increasing fineness of the ripples with increasing speed can be clearly observed.

The formation of fine ripples can be explained according to the model forwarded by Anthony and Cline (1977). They showed that the fine ripples formed as a result of surface tension gradients, caused by the presence of substantial temperature gradients in the melt pools. During surface melting, the heat flows in all directions away from the centre of the beam, resulting in a radial temperature gradient. Just underneath the beam, the temperature of the melt pool is at its maximum and the surface tension of the liquid metal is at a minimum. The temperature of the liquid metal decreases away from the centre of the beam, causing the surface tension to increase. As a result, liquid is pulled away (fig. 5.28) from the centre of the beam, thereby depressing the surface of the liquid under the beam and heightening the liquid surface elsewhere. Since the material under the beam moves in one direction, effective heightening of the liquid surface occurs only at the tail end and the sides of the melt pool.

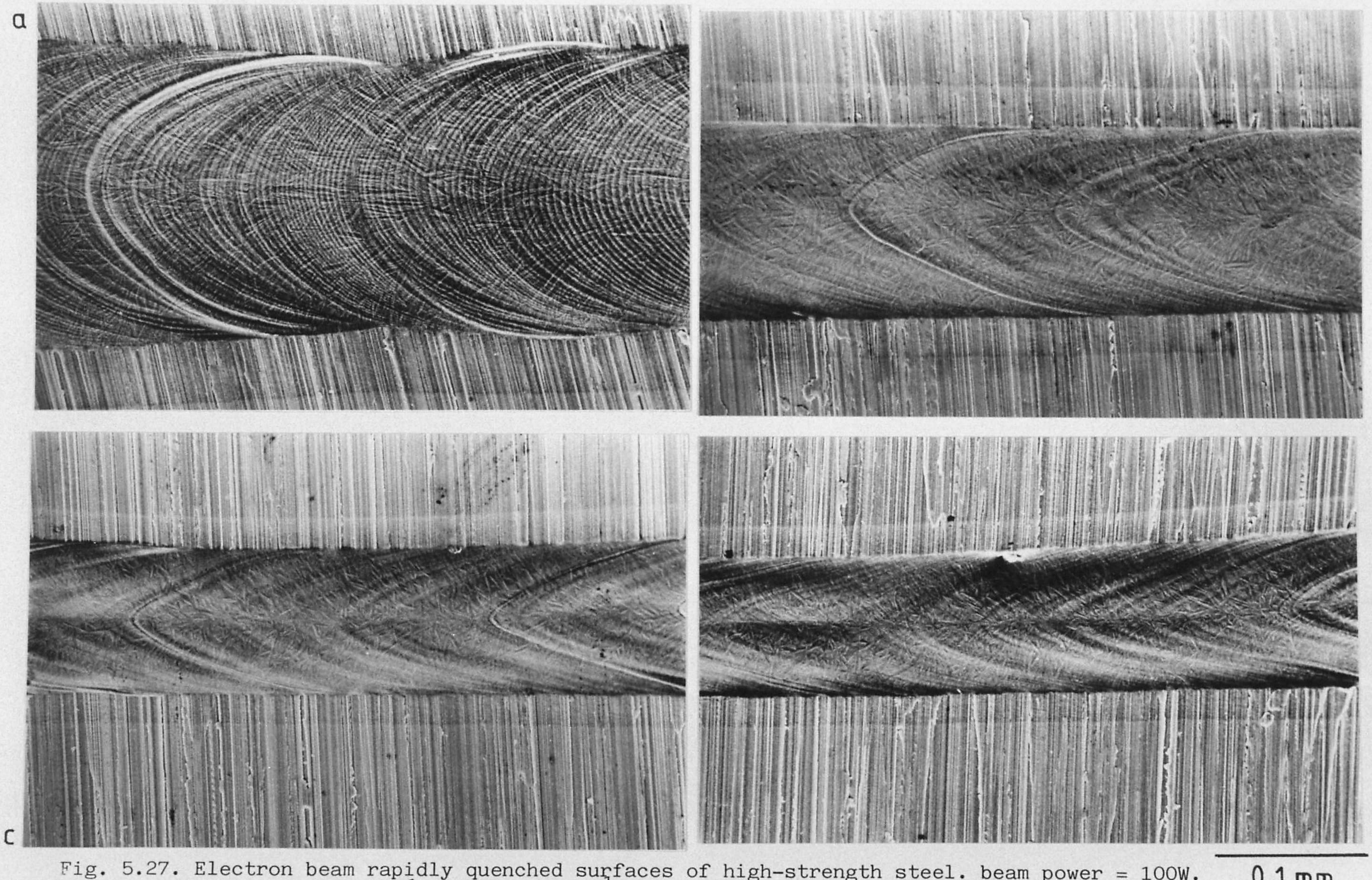

Fig. 5.27. Electron beam rapidly quenched surfaces of high-strength steel. beam power = 100W. traverse speeds; a)6.8 cm s^{-1} b) 20.4 cm s^{-1} c) 29.5 cm s^{-1} d) 34.2 cm s^{-1} (SEM)

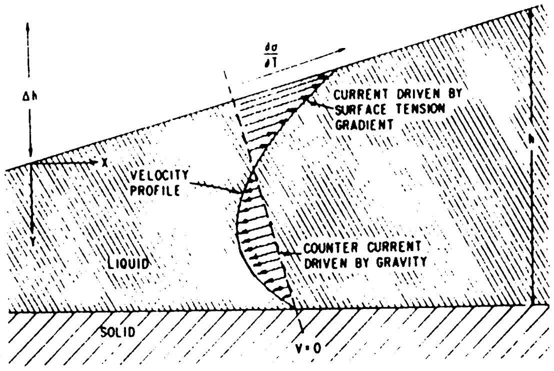

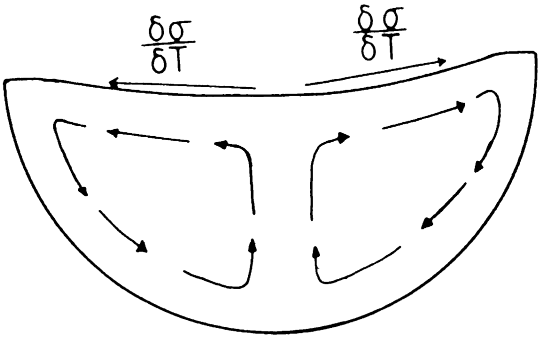

Fig. 5.28a. Flow pattern of a liquid surface layer, due to surface tension gradients counteracted by the force of gravity (after Anthony and Cline 1977)

5.28b. Schematic representation of the flow pattern in a transverse cross section of a liquid layer.

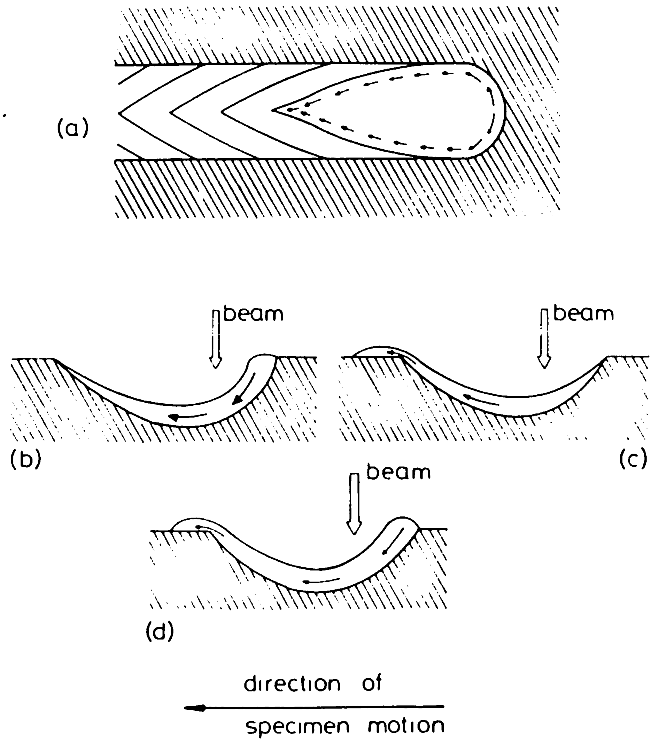

Fig. 5.29. Schematic representation of the rippling phenomenon (after Strutt 1980)

When the height difference, between the liquid at the centre of the beam and away from the beam increases, a pressure head develops and induces a counterflow of liquid back to the centre due to the force of gravity. At the steady state, the liquid flow due to surface tension and the gravity counterflow are balanced. Due to rapid solidification rates involved in surface melting these distortions of the liquid surface became frozen into the solid.

The ripple formation was also discussed by Strutt (1980) considering the hydro-dynamics involved in the melt. The model he proposed can be used to explain the coarse ripple formation. Two principal driving forces for the fluid motion in the melt pool were considered. One is the force of gravity, caused by the different levels of height within the melt pool and the other is the force applied by the vapour pressure at the front edge of the melt pool.

Motion of the material relative to the beam at first results in the formation of a liquid bulge ahead of the beam. The force of gravity causes the (fig.5.29) molten metal in this raised area at the front, to flow around the depression in the melt pool, enabling the fluid level in the back and front of the depression to gain the same height. The metal is so rapidly heated at the front edge of the melt pool, that a vapour pressure in excess of that at the rear of the pool is established there. Consequently this high pressure forces the liquid metal to flow to the back of the melt pool, resulting in a liquid overflow at the tail end. Fig.5.29 b,c and d show a schematic representation of this phenomenon. The formation rate of liquid in the bulge ahead of the beam as well as the rate of development of the critical vapour pressure depend on the process parameters such as beam power and traverse speed. Thus overflowing of the liquid melt at the trailing edge occurs periodically. Due to the high cooling rates involved in the rapid solidification, these flow marks are frozen in and appears as coarse ripples on the solidified surface.

It was observed that the surface ripples became finer when the traverse speed was increased. The maximum ripple heights were measured across the melts, perpendicular to the specimen traverse directions. The variation of the average maximum ripple height with the traverse speed is listed in table 5.2. Typical profilometer traces are shown in fig.5.30. Since the ripple height decreases as the traverse speed increases, it can be assumed that there is a critical traverse speed which would make the ripple height, zero.

The beam velocity required to supress rippling was discussed by Anthony and Cline (1977). Considering a linear velocity profile and shear stresses acting in the liquid metal and the surface tension gradient in the liquid, they theoretically obtained a critical velocity (V_c), that the beam must exceed to avoid surface ripples

$$V_c = \left(\frac{hg}{12}\right)^{1/2} \qquad 5.5$$

where h = thickness of the melt layer

and g = gravitational acceleration.

Since h depends on the beam power, thermal properties of the material and the traverse speed itself, equation 5.5 is more complicated than it appears to be.

In the present work of surface melting of ultra high-strength steels, this equation does not give accurate results. For example, with a 100W power electron beam and a traverse speed of 20.5 cm s^{-1}, a melt depth of 0.068mm was obtained experimentally. The surface of this melted region contained fine ripples. According to equation 5.5,

Table 5.2

Heights of surface Ripples of Electron Beam Melted Materials.

Traverse speed	Average Ripple Height (μm)	
cm s^{-1}	High-strength steel	$Fe_{80}P_{13}C_7$ alloy
6.8	6.9	15.0
11.4	4.0	13.0
20.5	3.2	11.5
24.8	3.0	7.5
29.6	2.7	2.5
34.2	1.5	4.5

A beam power of 100W was used.

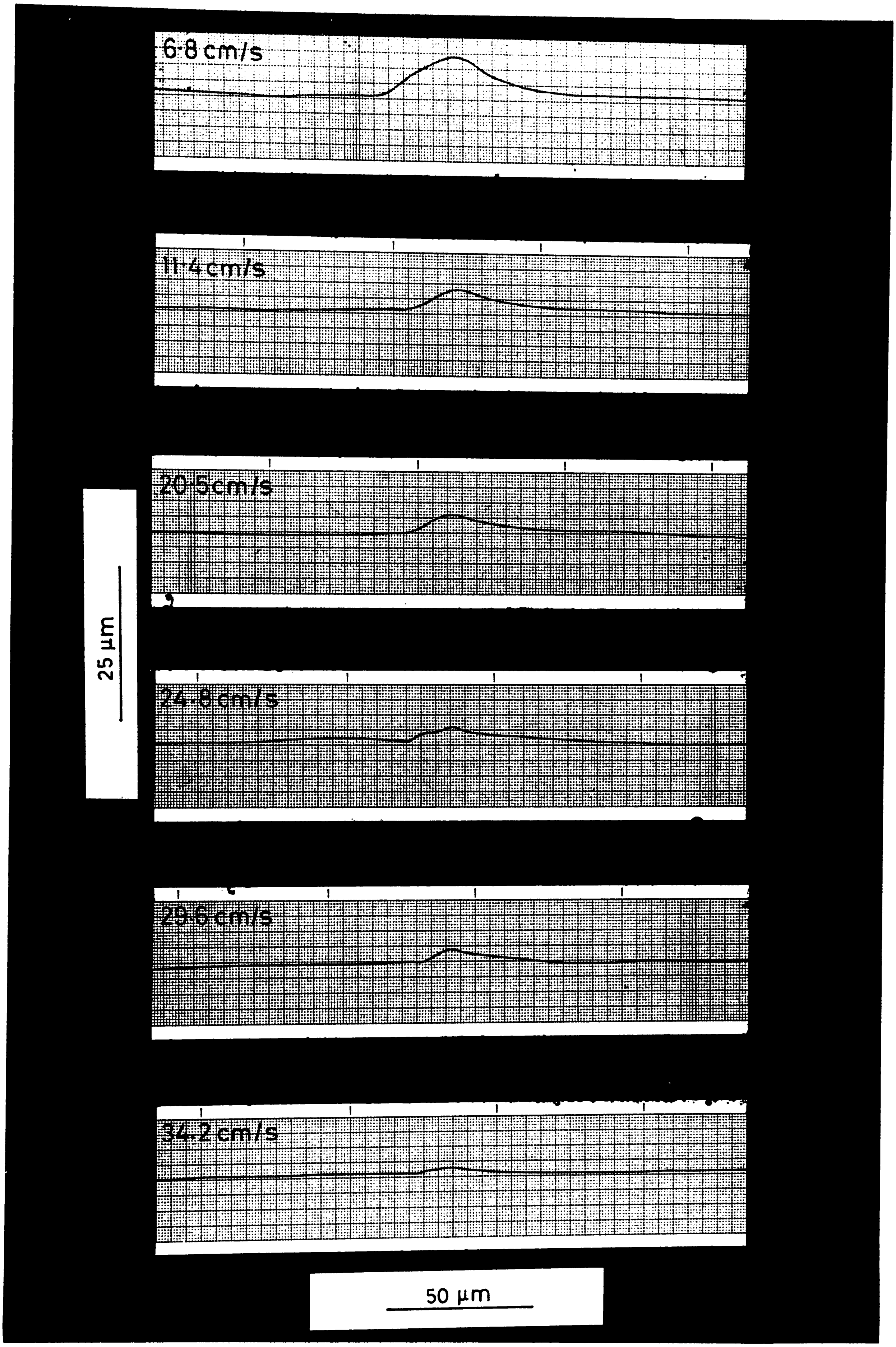

Fig. 5.30. Profoliometer traces taken across rapidly quenched surfaces of high-strength steel (100W electron beam) The traverse speeds used are marked on the traces.

if the melt depth is 0.068mm, the critical speed, which would avoid the rippling is 0.75 cm s^{-1}. Since surface ripples were observed experimentally even at a speed of 20.5 cm s^{-1}; about 27 times greater than the theoretical critical speed, the validity of equation 5.5 is questionable.

In electron and laser beam surface melting, if the interaction time is relatively great, the beam penetrates into the material, melting the material to a greater depth. A plasma cavity may also be observed at the surface. The melt pool near the surface can take a semi-circular shape but at the bottom of the melt pool, the depth can be a few times of its width. The resulting overall shape is that of a keyhole and hence is known as the keyhole effect. (Mazumdar and Steen 1980, Strutt 1980). In the present work, the keyhole effect was avoided by the use of low power beams and high traverse speeds.

Fig.5.31 is an example of a transverse cross section of an electron beam melted region showing the approximately semi-circular shape obtained (as discussed in chapter 4), justifying the use of Rosenthal's theory of heat flow. However at higher power inputs, the surface became rougher with an elevated central crest and deep troughs on either side of the crest. Usually when the power is increased, the vapour pressure at the front edge of the melt pool exerts a higher pressure at that edge. Consequently, the liquid metal is pushed heavily along the troughs, making the troughs deeper and causing the material to overflow at the trailing edge well above the original surface, forming an elevated crest. Fig.5.32 is a transverse cross section of a melt at 1100W but with a low traverse speed of $\sim$ 2cm s^{-1}. In this instance, the elevated crest and deep troughs and the probable onset of the keyhole shape at the liquid-solid interface are visible.

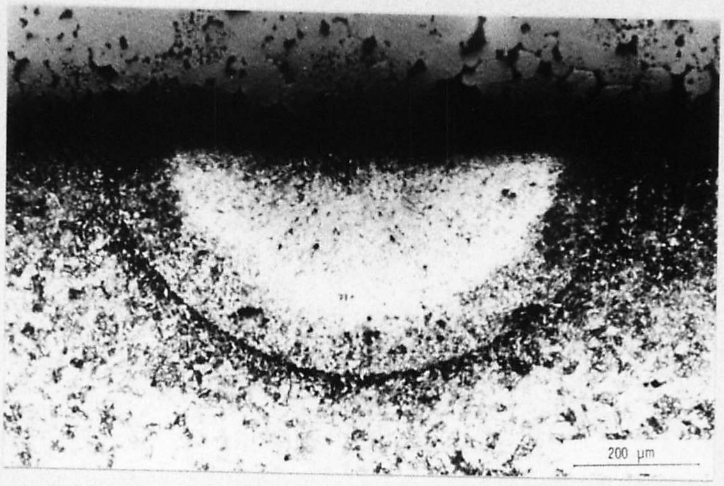

Fig. 5.31. A transverse cross section of an electron beam melted region, showing the approximately semi-circular shape. (Optical micrograph).

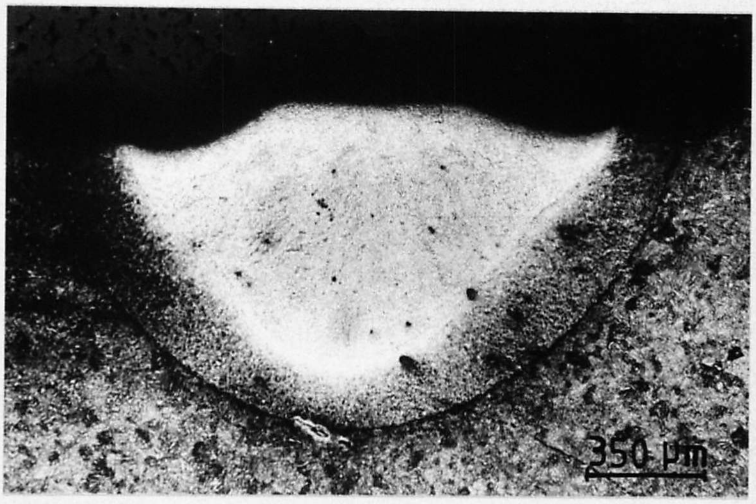

Fig. 5.32. A transverse cross section of an electron beam melted region, showing the elevated crest and the troughs on both sides of the crest, beam power - 1100W, traverse speed ~2 cm s^{-1} (Optical micrograph)

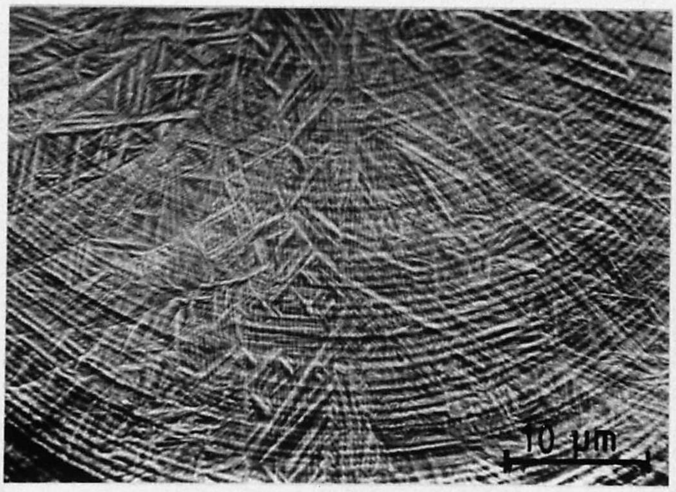

Fig. 5.33. Martensitic nature of the rapidly quenched surface observed without etching (SEM)

By scanning electron microscopy, the martensite nature of the microstructure could be observed on the rapidly quenched surfaces even without etching. (fig.5.33). No quench cracks were observed at the melted zones or the heat affected zone. Fig.5.33 also shows the surface dendrites, which had grown radially away from the centre, indicating the maximum heat flow direction.

5.1.6. Rapid Quenching of Surface Areas by Overlapping Passes.

Larger surface areas of steel specimens were rapidly quenched using multiple electron beam passes. Since the dimensions of the vacuum chamber are 30 x 30 x 30 cm, it was possible to surface melt fairly large samples, but only specimens with surface areas up to 5 x 5 cm^2 were used in the experiments. Overlapping beam passes were used for this purpose. By traversing the specimen under the focussed electron beam in two orthogonal directions, as shown schematically in fig. 5.34, it was possible to rapidly quench the complete surface areas.

Fig. 5.35 is a transverse cross section of electron beam treated area with multiple passes. The electron beam passes A, B and C, marked in fig. 5.35, were carried out sequentially. As a result of the overlap, a part of each melt pool became the heat affected zone of the next melt pass. Fig. 5.36 shows a scanning electron micrograph of the same sample. Here X, Y and Z areas were rapidly quenched consecutively. The line Y_1Y_2 on the surface shows the edge of the heat affected zone of the melt pool Y, but now Y_1Y_2 lies on the melt pool X. Similarly Z_1Z_2, which is the edge of the heat affected zone of melt pool Z lies on the melt pool Y.

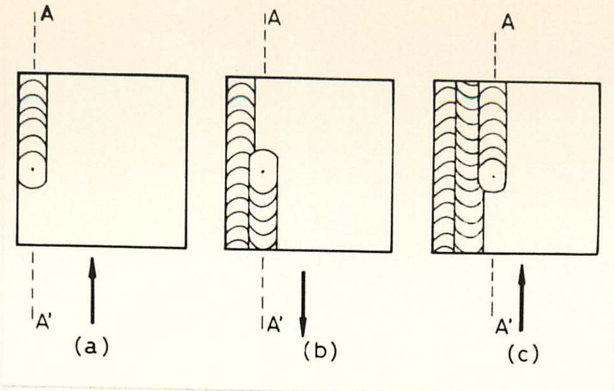

Fig. 5.34. Schematic diagram showing the rapid quenching of complete surface areas by overlapping electron beam passes. AA' is the line, which the beam interacts with the surface. a, b and c show the steps taken.

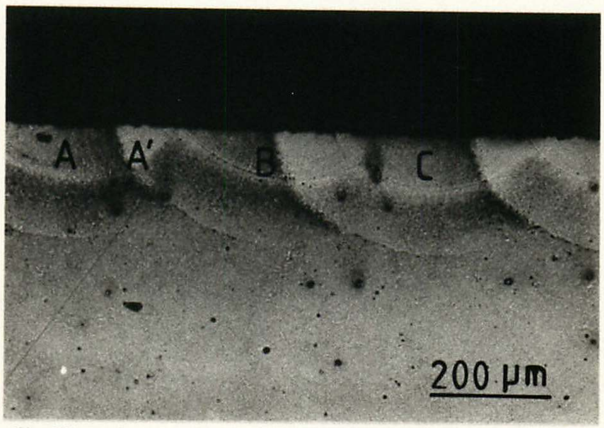

Fig. 5.35. A transverse cross section of electron beam treated area using overlapping passes. Beam passes A, B and C were carried out sequentially. (Optical micrograph)

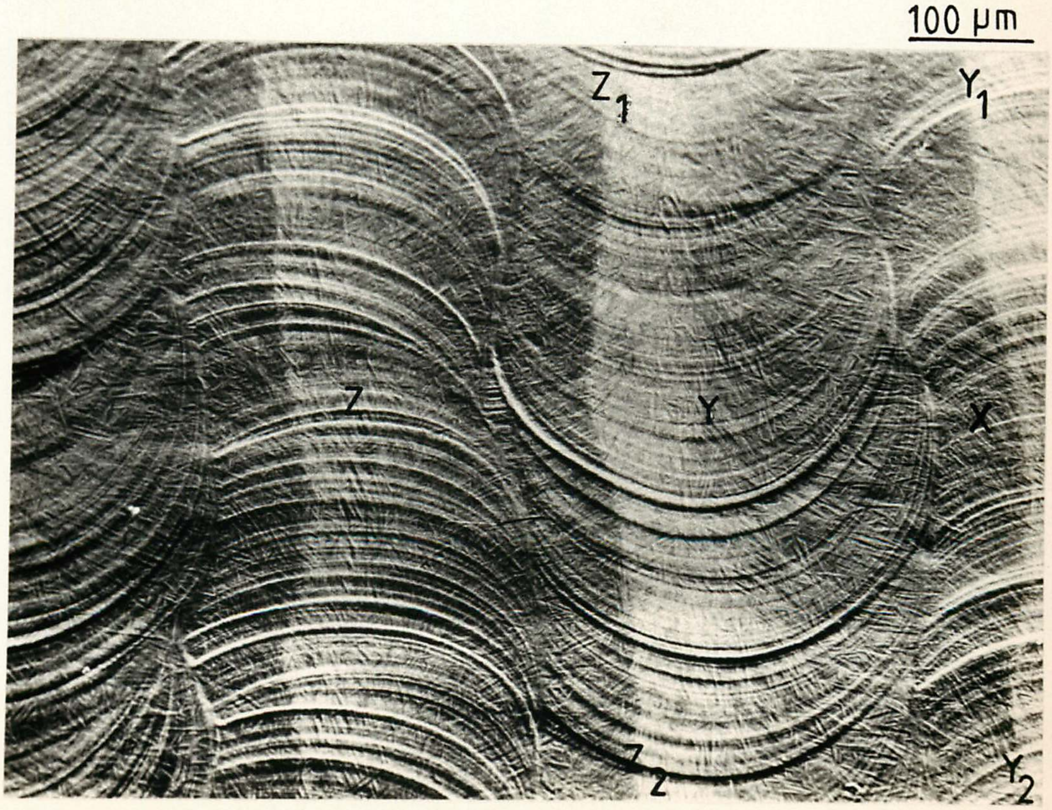

Fig. 5.36. A scanning electron micrograph of a surface, rapidly quenched using overlapping passes. The areas X,Y and Z were rapidly quenched consecutively.

From these observations, it is clear that the surface areas rapdily quenched by overlapping passes contain alternate areas of rapidly quenched and heat affected zones. However, quench cracks or any sort of surface cracking were not observed. The microhardness measurements showed that the microhardness of original melt zones were hardly affected by the heat effects of the neighbouring beam passes. Microhardness of these areas (e.g. area A' in fig. 5.34) were ∿790 VPN, which were a little lower than those of original melt zones.

Although no cracks were observed in electron beam melted surface layers of ultra high-strength steel, the formation of martensite ensures that residual thermal stresses will be present. Stresses and strains may also have arisen in the surface layer, due to the rapid solidification. Usually the stresses caused during the solidification of casting and welding of steels are removed by annealing at a temperature of ∿650°C. The heat effects from the neighbouring passes on the original melt passes, described above, may have a similar annealing effect, and cause a certain relief of internal stresses, making the surface properties better than in the original melt layer.

5.2. $Fe_{80}P_{13}C_7$ Alloy

5.2.1. Amorphous Layers at the Surface

The as cast microstructure of $Fe_{80}P_{13}C_7$ alloy specimens, prior to electron beam quenching consisted of coarse dendrites. After rapid quenching using electron beams, the surface melted areas were quite distinguishable in their cross sections due to the featurelessness of these regions (fig. 5.37). A larger part of the melt pools near

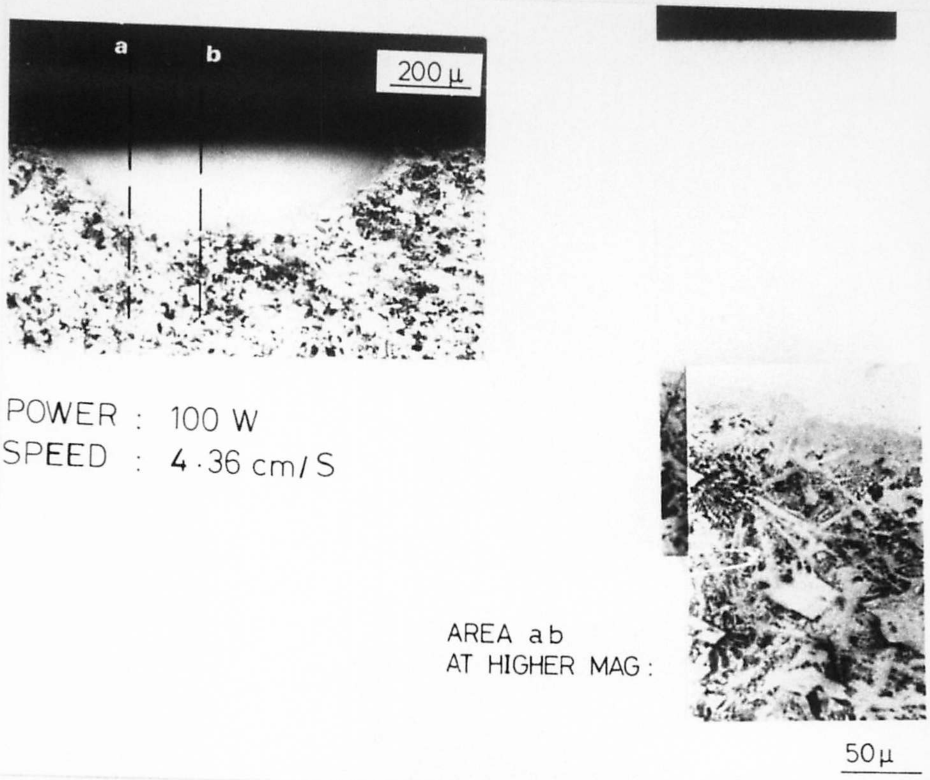

Fig. 5.37. A transverse cross section of an electron beam melted surface area of $Fe_{80}P_{13}C_7$ alloy. (Optical micrographs)

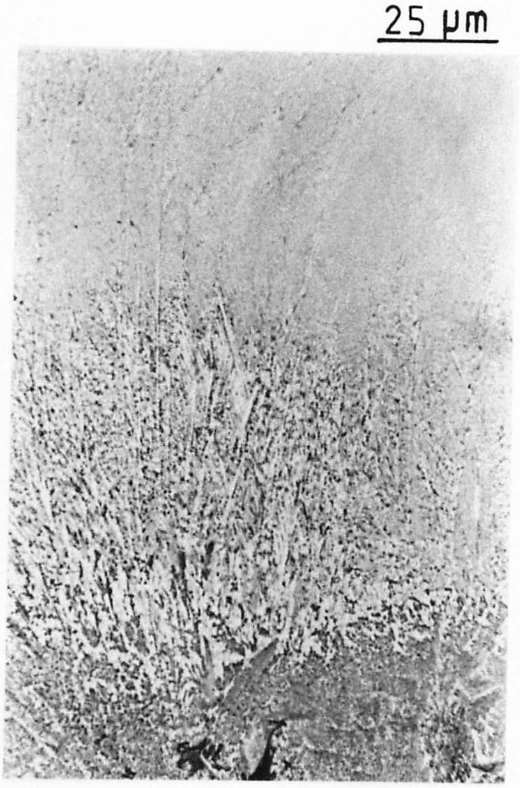

Fig. 5.38. Dendritic nature of the heat affected zone (area between the structureless melted area and the substrate). of another electron beam rapidly quenched $Fe_{80}P_{13}C_7$ alloy sample. (Optical micrograph).

the surface was structureless and even at higher magnifications no structure was detected, suggesting that the melt pools had become a metallic glass. However in the areas near the substrate, (heat affected zone) dendrites were present. Fig. 5.38 shows the dendritic nature of the areas between the featureless surface layer of a melted region and the substrate. Usually, all the dendrites had the same morphology in this region. They grew up from the bottom of the fusion zone and had finely spaced branches.

$Fe_{80}P_{13}C_7$ alloy has a ternary eutectic composition and therefore as discussed in section 2.1, has a higher glass forming tendency. Metallic glasses of Fe-P-C alloys have been formed earlier at a range of composition. The formation of $Fe_{80}P_{13}C_7$ (Duwez and Lin, 1967), $Fe_{80}P_{15}C_5$ (Duwez, 1967) and $Fe_{80-x}M_xP_{13}C_7$, where M = Ti, V,Cr,Mn,Co or Ni (Masumoto and Maddin 1971 , Naka et al 1975) metallic glasses have been reported. However, these metallic glasses were produced by rapid quenching methods such as centrifugal quenching or melt spinning and not by laser or electron beam surface quenching methods.

Confirmation of the amorphous nature of the electron beam quenched $Fe_{80}P_{13}C_7$ alloy was very difficult due to the thinness of the surface layers. In the present work amorphous structures were distinguished from crystalline structures by,

1. The presence of a relatively diffuse peak over a relatively wide scattering angle obtained by X-ray diffractometry

and/or

2. A diffuse ring pattern obtained in electron diffraction.

Fig.5.39 a and b show the X-ray intensity curve (Co K_α radiation) and electron diffraction patterns of amorphous $Fe_{80}P_{13}C_7$ alloy produced by melt spinning processes.

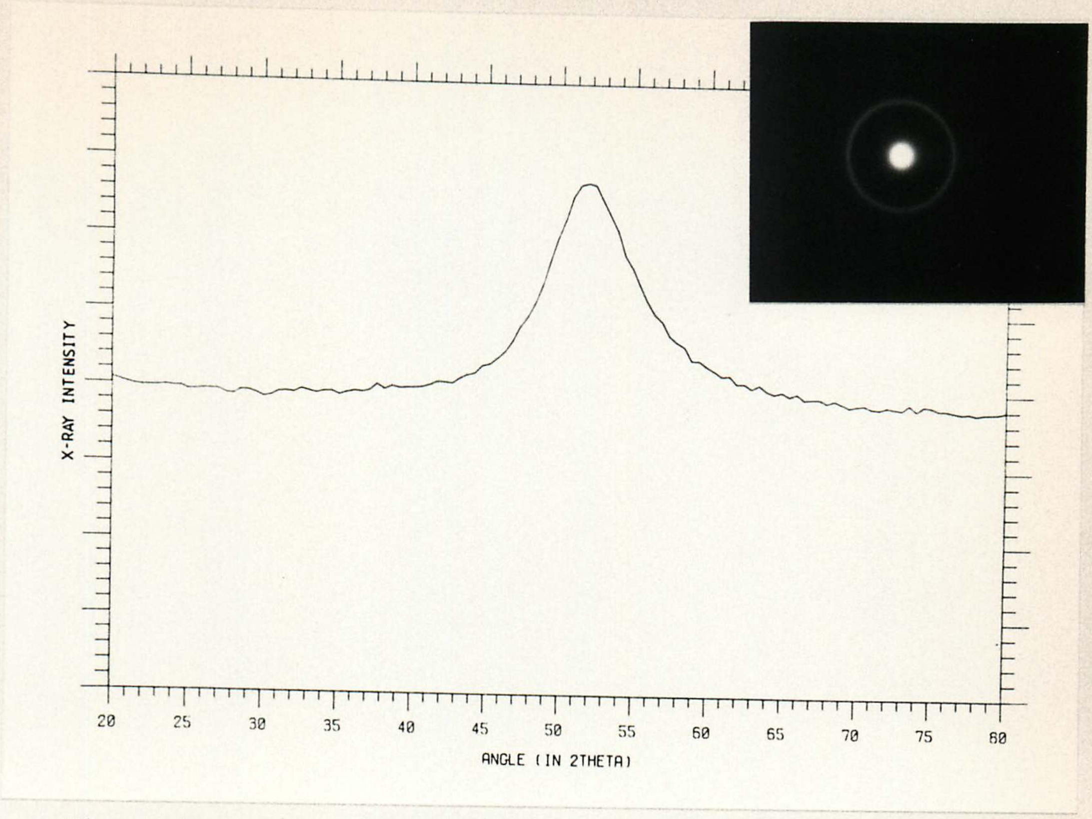

Fig. 5.39.
a) X-ray intensity curve (CoK_{α}), (b) electron diffraction pattern, of amorphous $Fe_{80}P_{13}C_{7}$ alloy ribbons produced by melted spinning.

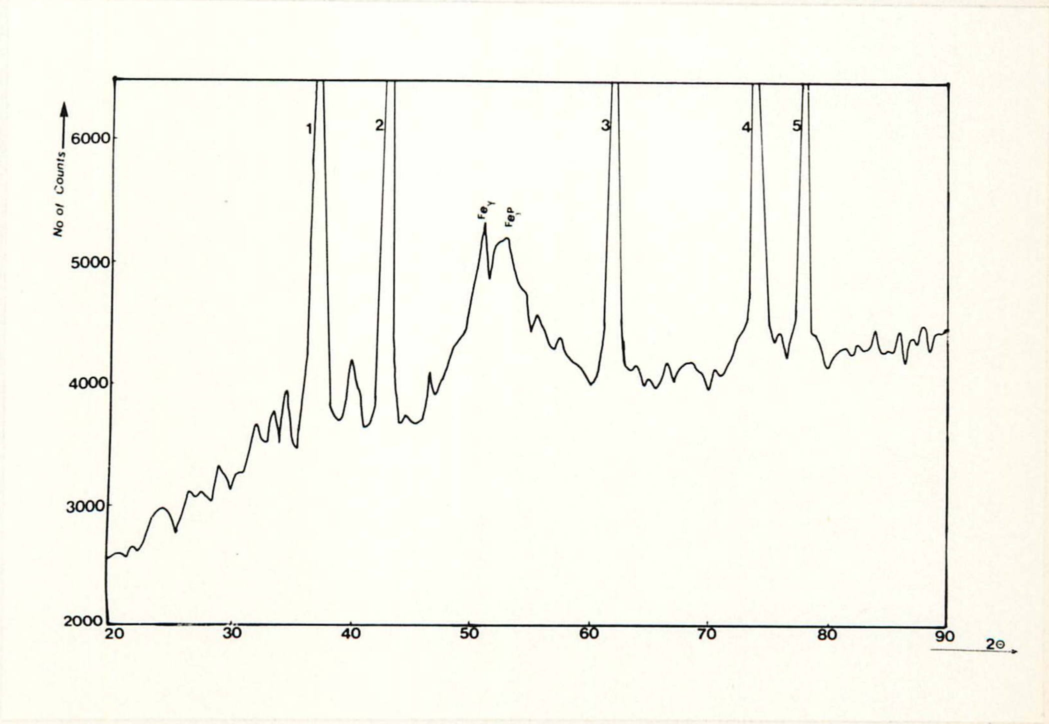

Fig. 5.40. X-ray intensity curve (CoK_{α}) of the electron beam melted region of high strength steel. Adjacent substrate area was masked with a lead sheet. (Peaks 1-5 are from the lead sheet).

In order to determine the structure of the electron beam melted regions of the $Fe_{80}P_{13}C_7$ alloy, at first X-ray diffractometry ($Co\ K_\alpha$) was used. Since the melted areas were very narrow (<1mm), it was difficult to collimate the X-ray beam, only on the surface melted region. However, in an attempt to isolate this region, the adjacent substrate area was masked with a thin lead sheet. The results obtained are shown in fig.5.40. Peaks labelled 1 to 5 are from the masking lead sheet. The region of interest correspond to the broad peaks at $2\theta = 51°$ and $53°$, which could be attributed to crystalline Fe and Fe_3P respectively. The width of these peaks ($\Delta 2\theta = \sim 12$ degrees) is much larger than that for the crystalline materials and indicates the overlapping of diffracted information from both the crystalline and amorphous regions. In pure amorphous materials, well defined peaks do not arise but as shown in fig.5.39a a broad diffuse scattering is expected in the X-ray intensity curves.

The amorphous nature of the $Fe_{80}P_{13}C_7$ surface melted layer was confirmed by electron microscopy. Thin foil preparation was extremely difficult but it was possible to investigate some thin areas. Fig.5.41 shows an amorphous area observed in an electron beam melted region and the corresponding diffraction pattern. The observed microhardness of the melted regions was also consistent with the presence of amorphous material. The micro-hardness of melt spun amorphous ribbons (amorphous nature confirmed by X-ray and electron diffraction) was found to be ~ 925 VPN. In the vicinity of the surface of the electron beam quenched regions, the microhardness was ~ 910 VPN, approximately similar to that of amorphous ribbons. The microhardness of the surface melted regions will be discussed in the next section.

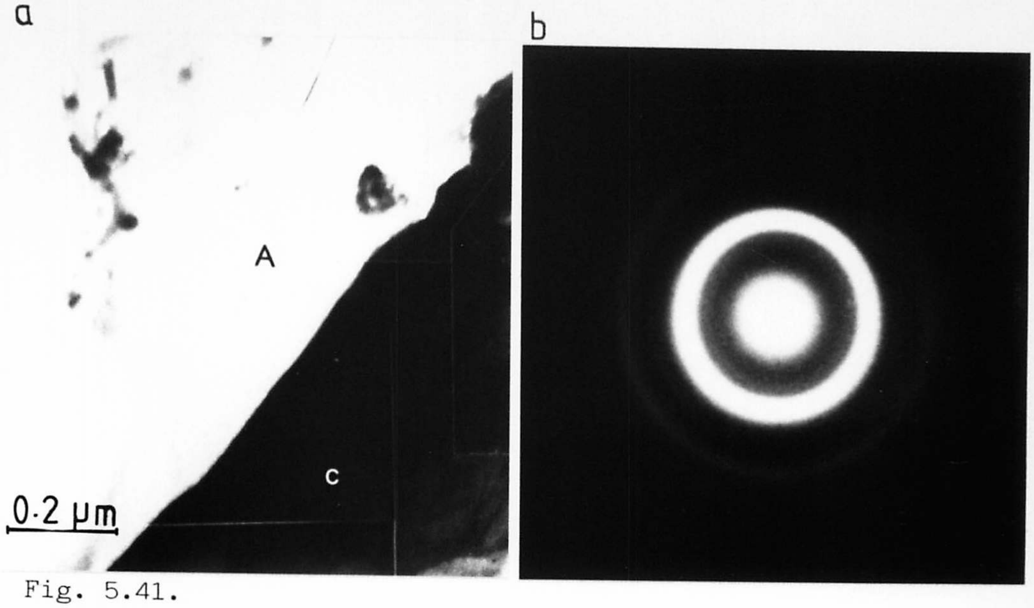

Fig. 5.41.
(a) An amorphous area observed in electron beam rapidly quenched $Fe_{80}P_{13}C_7$ alloy. A=Amorphous, C=Crystalline (TEM)
(b) Electron diffraction pattern obtained from the amorphous area.

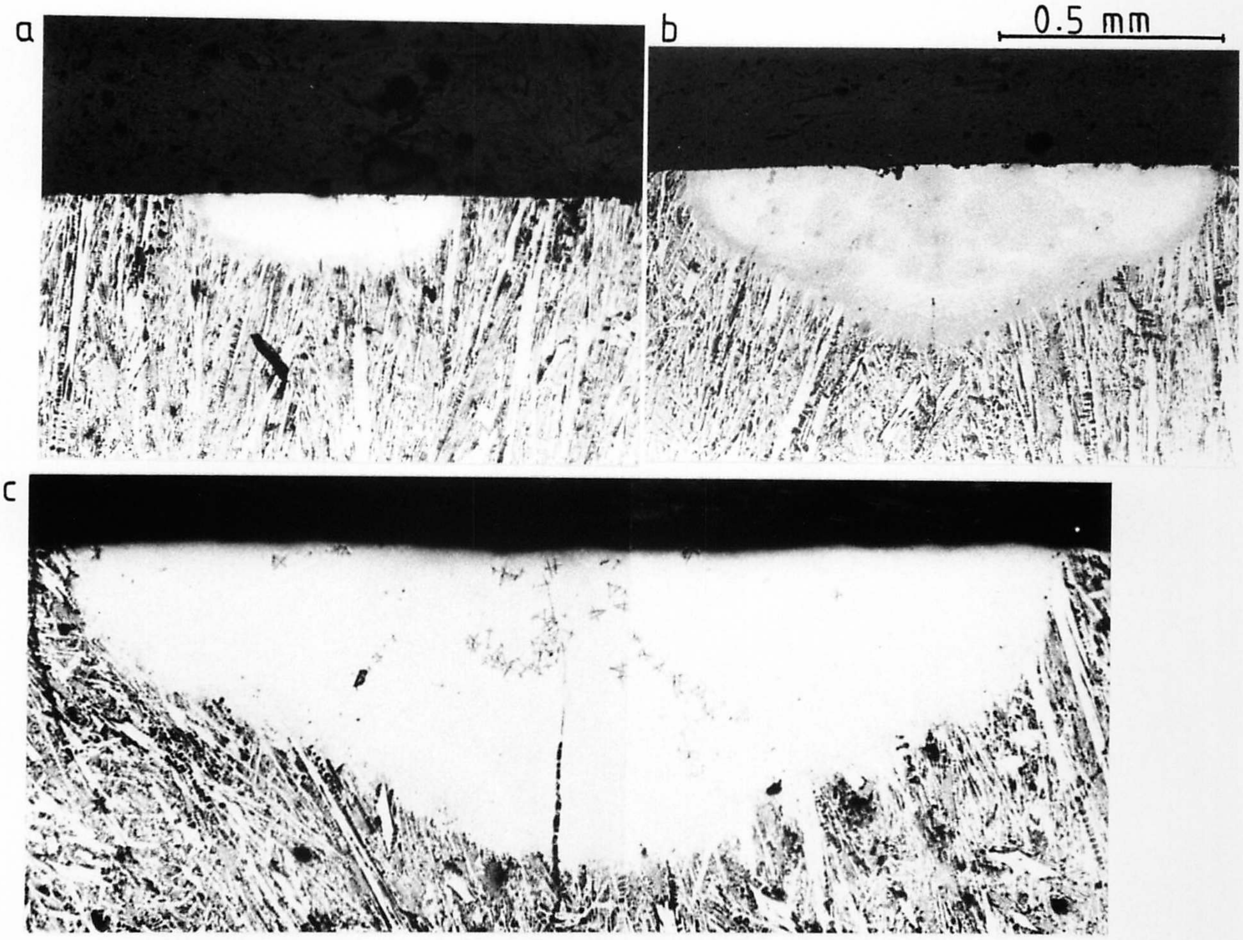

Fig. 5.42. Transverse cross sections of electron beam rapidly quenched $Fe_{80}P_{13}C_7$ alloy, with beam powers of (a) 100W (**b**) 300W and (**c**) 900W. Traverse speed was fixed at 4.4 cms^{-1}. (Optical micrographs)

In chapter 4, it was theoretically demonstrated that the quench rate decreased with any increase in beam power at the same traverse speed. This effect was experimentally confirmed by varying the beam power during the surface melting of $Fe_{80}P_{13}C_7$ alloy. At low power levels, the resolidified areas were featureless and any dendritic nature could be observed only in the areas near the substrate. Fig. 5.42a, b and c show the surface melted areas with a fixed traverse speed of 4.4 cm s^{-1} but at different beam powers of 100W, 300W and 900W respectively. Some dendritic areas, which were present near the surfaces of high power beam melted areas could be observed even at low magnifications, indicating the crystalline nature of these areas. Fig. 5.43 is an optical micrograph at higher magnification, showing the crystalline areas present near the surface in fig.5.42c. These dendrites have nucleated near the free surface, whereas the dendrites at the bottom of the melt pools, have grown from the substrate towards the free surface.

5.2.2. Property Evaluation

Microhardness measurements of a melt region, from the free surface to the substrate are shown in fig.5.44. In the vicinity of the surface, microhardness was $\sim$ 910 VPN. It increased with depth below the surface, up to about 1250 VPN and then gradually fell to $\sim$ 650 VPN, the latter being the microhardness of the as cast substrate. Naka et al (1975) reported a higher hardness for Fe_3C-Fe_3P compound in the crystalline $Fe_{80}P_{13}C_7$ alloy than that for the same alloy in the amorphous state. This explains the observed increase in microhardness with depth; the region near the substrate was crystalline.

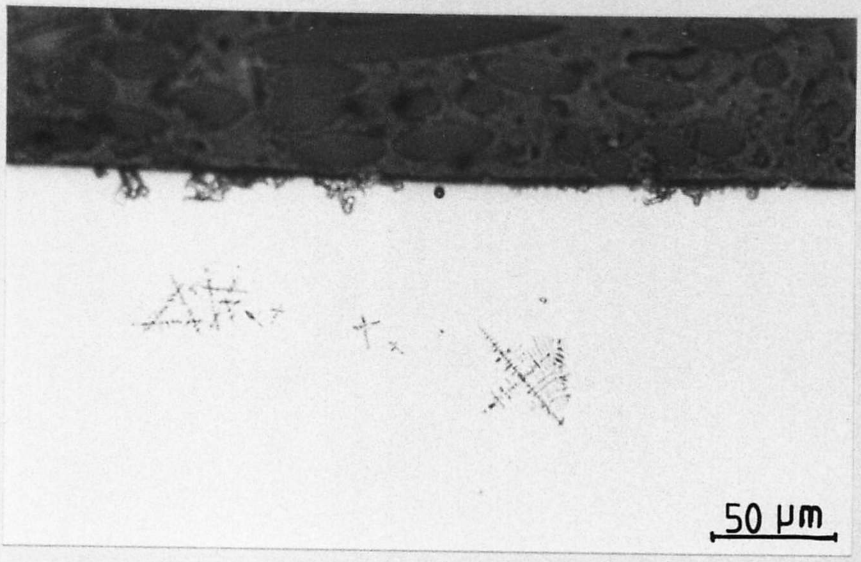

Fig. 5.43. An optical micrograph at a higher magnification showing the crystalline areas present near the surface in fig. 5.42 C.

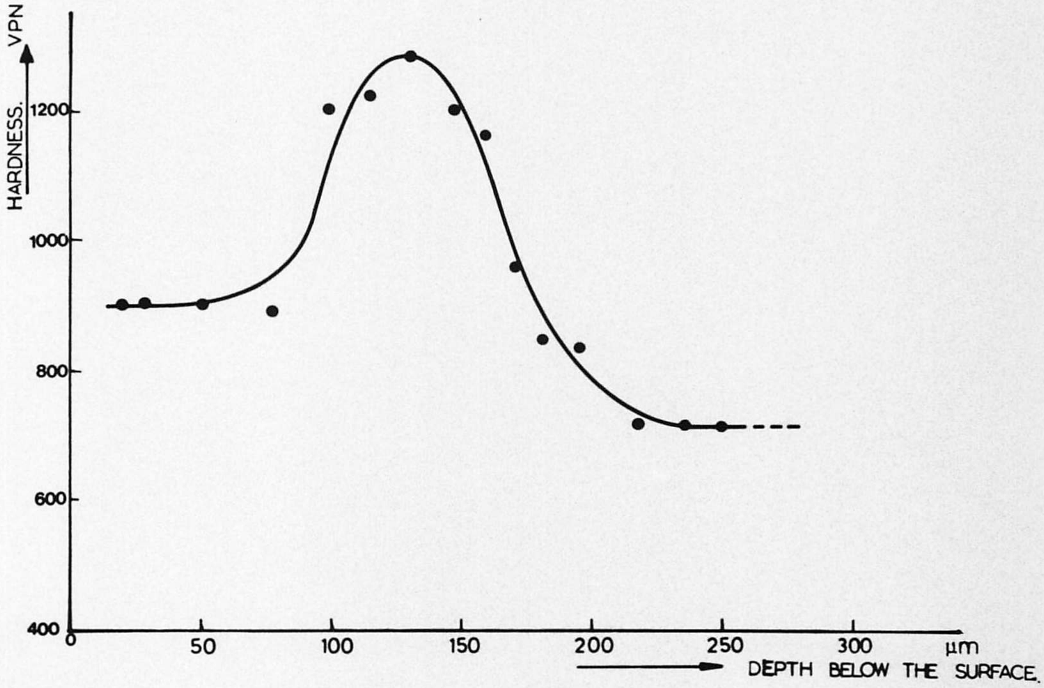

Fig. 5.44. Variation of micro-hardness of an electron beam rapidly quenched surface of $Fe_{80}P_{13}C_7$ alloy, with the depth below the surface. Beam power used - 100W, traverse speed 4.4. cm s^{-1}

However, there is a difference in the values of the microhardness of amorphous $Fe_{80}P_{13}C_7$ phase between the work of Naka et al. (1975) and the present work. They reported a microhardness of $\sim$760VPN compared with the $\sim$ 910-925 VPN observed in the present work. The exact reasons for this difference is not clear but the variation in quenching rates may have an effect on the microhardness of metallic glass. Naka et al.'s experiments involved a centrifugal rapid quenching method and it is possible that this could explain the difference in hardness relative to the present work. Furthermore it should be noted that Collings et al. (1978) reported a microhardness of 936 ± 15 for $Fe_{80}P_{13}C_7$ metallic glass produced by melt spinning.

Masumoto and Maddin (1975) reported a value of 2.4 for H/σ_{UTS} of $Fe_{80}P_{15}C_5$ metallic glass. Davies (1975) suggested that H/σ_{UTS} of metallic glasses was insensitive to chemical composition. However, since $Fe_{80}P_{13}C_7$ composition is nearly similar to the composition of $Fe_{80}P_{15}C_5$, it can be expected that H/σ_{UTS} value for $Fe_{80}P_{13}C_7$ is also about 2.4. This assumption would give a σ_{UTS} value of $\sim$380 kg/mm^2 for $Fe_{80}P_{13}C_7$ metallic glass, showing that it has a remarkably high strength.

Another observation was the occurance of cracks in the surface melted layers. Cracks were found in most of the solidified layers, although a few crack free layers were also observed, when low power beams were used. In low power melted areas, the cracks were very fine and the coarseness of the cracks increased with increasing beam power, as shown in fig. 5.42. These cracks, which seem to have been caused by the stresses generated during solidification, were not observed in surface melted high strength steel. It is clear that the cracks initiated at the crystalline regions near the substrate. Microcrystalline phases of $Fe_{80}P_{13}C_7$ alloy usually consist of Fe_3C and Fe_3P compounds (Naka et al 1975) which are hard and brittle, and thus can be very susceptible to solidification stresses. As the liquid solidifies during rapid solidification, the volume of the melted zone expands. This uneven volume expansion induces stresses in the heat affected zone and the substrate. The brittle, crystalline, heat affected zone fails to accommodate the stresses and easily forms cracks. Apart from these stresses, caused by the volume expansion, the surface is also pulled towards the substrate from the both sides, due to the surface tension effects described earlier in section 5.1.5. These stresses help the cracks to propagate towards the surface.

On the other hand, the amorphous phase being free of grain boundaries is known to have better mechanical properties and would be expected to resist the propagation of cracks. This effect can be seen in figures 5.42 b and c, where some of the cracks were present only at the crystalline areas of the melt pool and have not propagated into the amorphous region. However, if the stresses are large enough, the cracks may propagate through the amorphous phase.

The measurement of the crystallization temperature (T_x) of $Fe_{80}P_{13}C_7$ amorphous surface layers was not possible as the amorphous phase could not be physically isolated. Hence, melt spun amorphous ribbons were used and T_x was measured using Differential Scanning Calorimetry (DSC). Metallic glasses are metastable with respect to crystalline phases at temperatures below the liquidus. On heating a metallic glass transforms to a crystalline phase or phases. Because these crystalline phases have a lower free energy, the reaction is always exothermic. Fig. 5.45 shows the DSC curve for the amorphous ribbons,

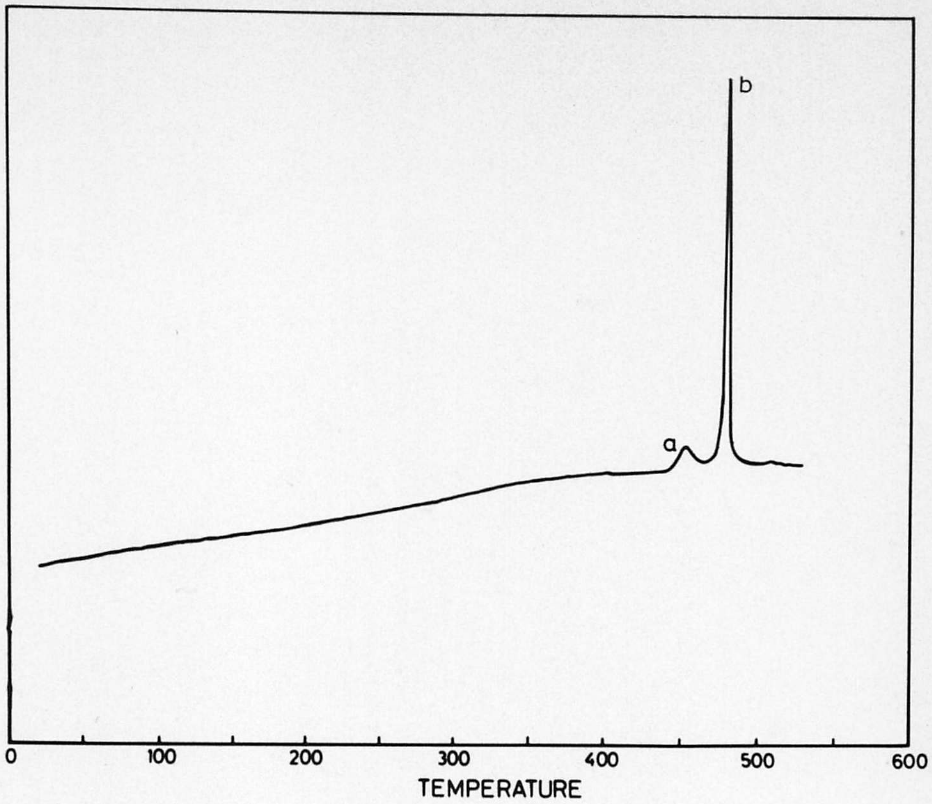

Fig. 5.45. DSC curve obtained for the $Fe_{80}P_{13}C_7$ amorphous ribbons, at a heating rate of 10°C min^{-1}. The peak at'a' indicates the primary crystallization at 458°C and the peak at'b'indicates the major crystallization to stable phases at 487°C.

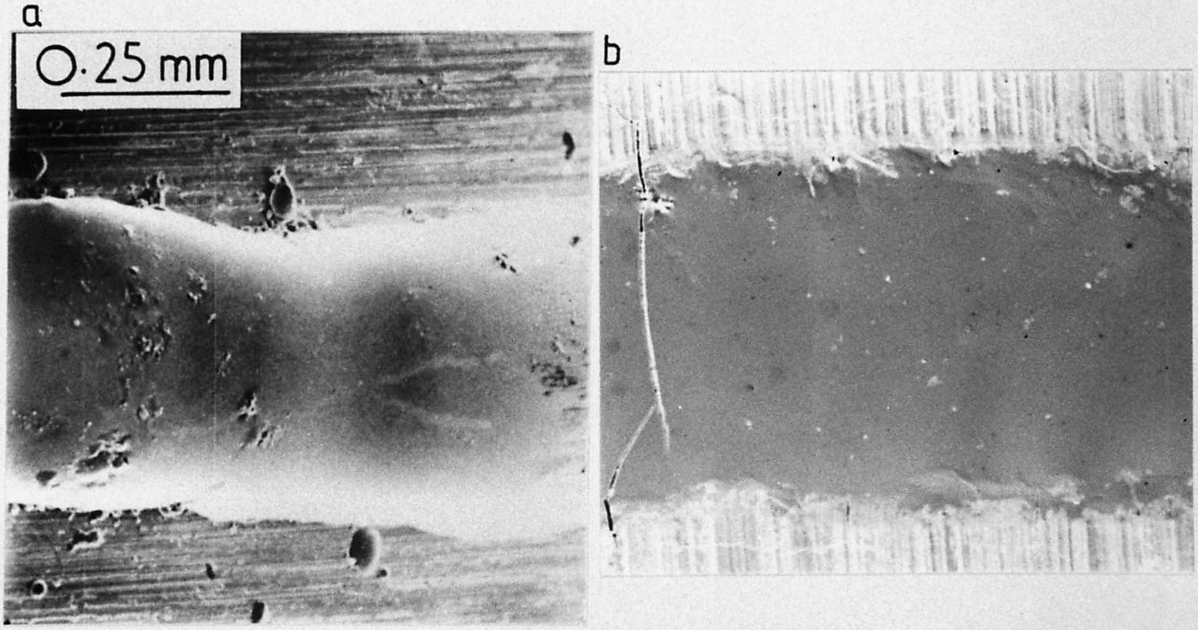

Fig. 5.46. a and b. Rapidly quenched surfaces of $Fe_{80}P_{13}C_7$ alloy (SEM)

at a heating rate of 10°C min^{-1}. The results indicate two exothermic peaks; A major exothermic peak at 487°C and a smaller peak at 458°C. The crystallization of amorphous $Fe_{80}P_{13}C_7$ alloy has been investigated in detail by Masumoto and Maddin (1975) and Yeh and Maddin (1979). They also reported the presence of two such peaks and with the experimental results obtained using DSC and transmission electron microscopy and demonstrated that the crystallization of $Fe_{80}P_{13}C_7$ alloy goes through an intermediate stage prior to the final crystallization. The two exothermic peaks observed correspond to these two stages; the first small peak for the primary crystallization and the second major peak representing the transformation to the stable crystalline phases. However, it is not possible to find a definite crystalline temperature (T_x) of a metallic glass, since it varies with the heating rate. Yeh and Maddin (1979), using DSC at a heating rate of 20°C min^{-1} observed the first and second crystallization peaks of $Fe_{80}P_{13}C_7$ amorphous phase at ∿452°C and 465°C respectively, which are slightly different from the temperatures observed in the present work.

After crystallization the microhardness increased from ∿ 925VPN (amorphous phase) to ∿1248 VPN, which is similar to that of crystalline heat affected zones of electron beam rapid quenched $Fe_{80}P_{13}C_7$ alloy. Crystallization of the amorphous ribbons made them brittle. They were ductile prior to crystallization but afterwards became so brittle, that they could be snapped between the fingers. This observed brittleness of the crystalline $Fe_{80}P_{13}C_7$ phase emphasizes the observations discussed earlier with regards to the formation of cracks in the heat affected area of electron beam treated regions. When annealed, structural rearrangements in metallic glasses lead to the formation of a fine dispersion of mechanically weak metal rich phase and a highly ordered metalloid rich phase with a high flow strength (Chen 1976). The difference between these two phases would result in stress concentrations and high local shear strains upon bending would make the glass brittle.

5.2.3. Topographical Characteristics

The surface morphology of $Fe_{80}P_{13}C_7$ amorphous layer suggests that the turbulance of the melt pool was at a minimum at the time of the solidification. Fig. 5.46 shows typical rapidly quenched surfaces of $Fe_{80}P_{13}C_7$ alloy. Fine ripples were never observed on the surface layers, within the range of the processing parameters used. This effect has been caused probably by a higher surface tension at the surface of liquid $Fe_{80}P_{13}C_7$ alloy. However the coarse ripples caused by the periodic overflow of liquid metal at the tail end of the melt pool (discussed in section 5.15) could be resolved. Cracks were present in the rapidly quenched regions but the amount of cracks was reduced by the use of low power electron beams. The surface did not show any dendritic nature or structure upon etching even at higher magnifications.

Fig. 5.47 shows typical profilometer traces taken across the individual surface melted regions of $Fe_{80}P_{13}C_7$ alloy, in a direction perpendicular to the direction of the traverse. These passes were made with 100W power electron beam, but with different traverse speeds. The variation of the average maximum ripple height with traverse speed is listed in table 5.2. The roughness of $Fe_{80}P_{13}C_7$ alloy surface decreased with increasing traverse speed, similar to the results observed in electron beam surface quenched ultra high strength steels (fig.5.30). It is reasonable to assume that at a much higher speed, the ripple height would become zero.

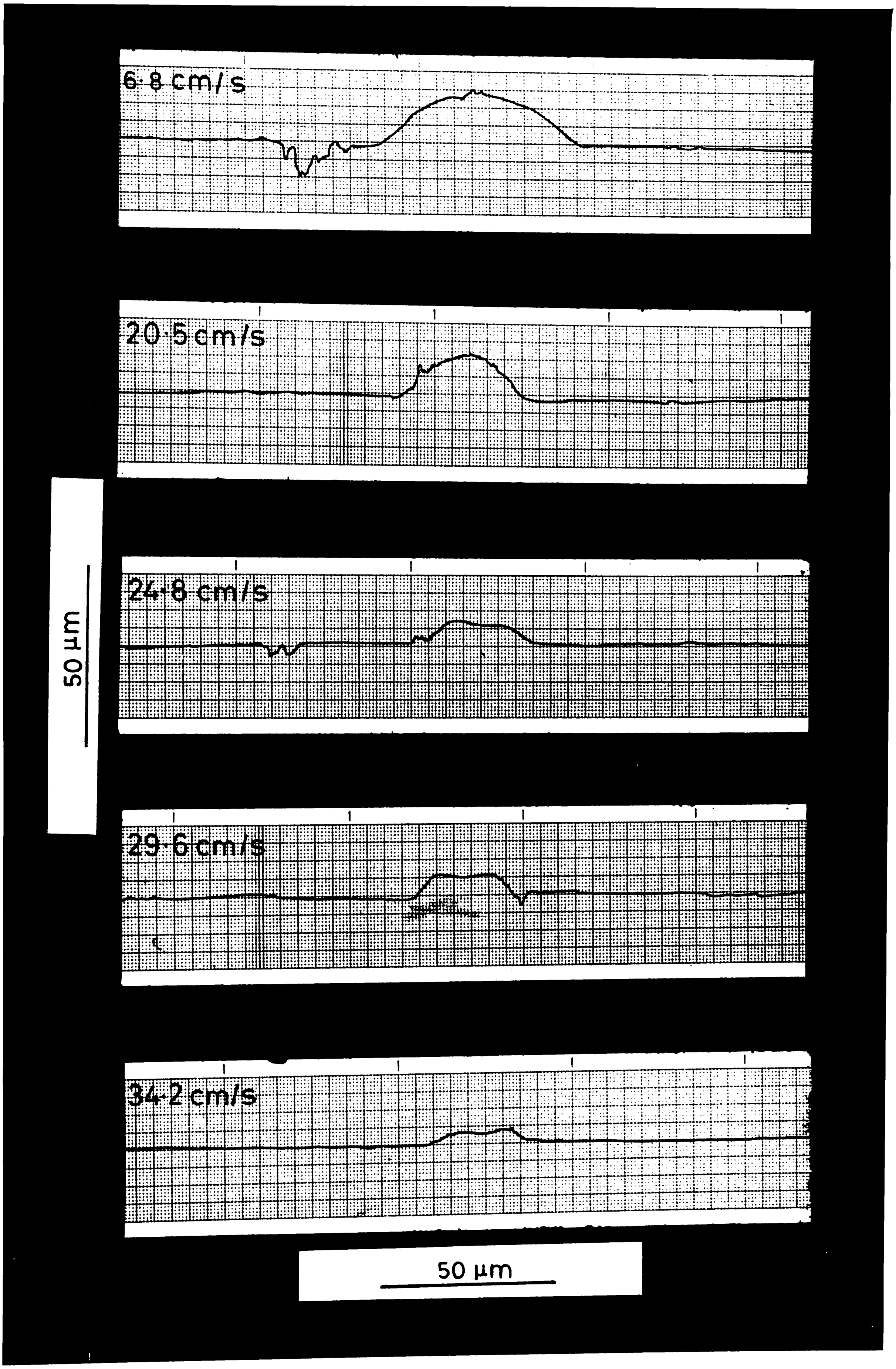

Fig. 5.47. Profoliometer traces taken across rapidly quenched surfaces of $Fe_{80}P_{13}C_7$ alloy. (100W electron beam) The traverse speeds used are marked on the tracers.

Although the surface melted regions of $Fe_{80}P_{13}C_7$ alloy were free of fine ripples, the height of coarse ripples seemed to be greater than those observed in the surface melted ultra high-strength steel. In steel, the maximum ripple height was $\sim 7\mu m$ at a low traverse speed of 6.8 cm s^{-1} and decreased to $\sim 1.5\mu m$ at 34.2 cm s^{-1} speed. The maximum ripple height of $Fe_{80}P_{13}C_7$ alloy was $\sim 16\mu m$ at 6.8 cm s^{-1} and decreased only to ~ 4.5 cm s^{-1} at 34.2 cm s^{-1} speed. It is possible that $Fe_{80}P_{13}C_7$ alloy in the liquid state has lower viscosity than ultra high strength steel, resulting in a higher amplitude of the coarse ripple, when the vapour pressure forced the liquid metal to overflow at the tail end of the melt pool. (coarse ripple formation on the surfaces was discussed in section 5.1.5.).

5.2.4. Rapid Quenching of Surface Areas by Overlapping Passes

Fig. 5.48 is a transverse cross section of the surface layer, melted with overlapping passes. The melted and resolidified regions were again featureless, but the effect of heat from the neighbouring passes on the featureless regions were quite distinguishable. Those areas of the amorphous regions have become crystalline. The microhardness of the unaffected areas (e.g. area x in fig. 5.48) of the original melt passes were in the range of 910-918 VPN, which were similar to that of melt spun and electron beam quenched regions of the $Fe_{80}P_{13}C_7$ amorphous alloy. The heat affected areas (e.g. area Y in fig. 5.48) had an average microhardness of ~ 1245 VPN, indicating its crystallinity.

A considerable amount of cracks were present on the surface. Figures 5.49 and 5.50 show the completely rapidly quenched surface at two different magnifications. As described earlier in section 5.2.2,

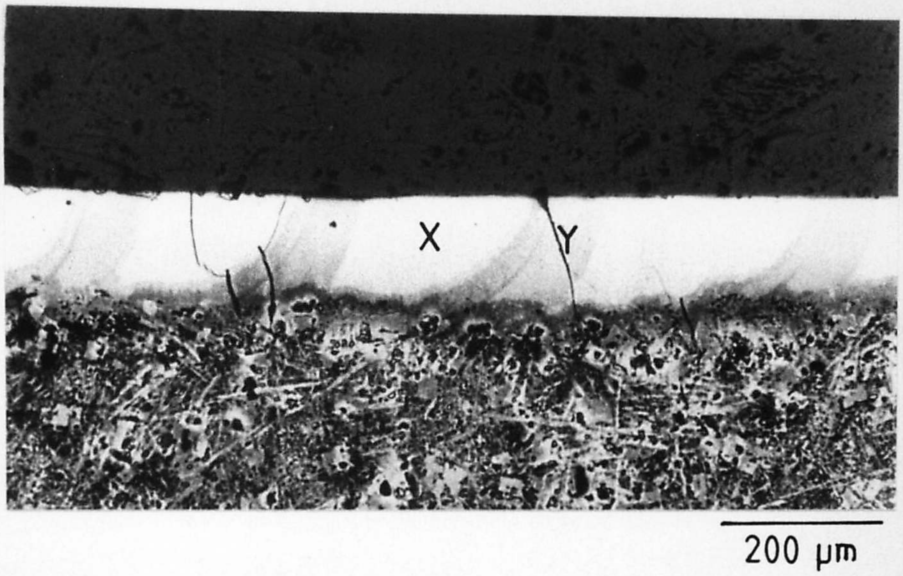

Fig. 5. 48. A transverse cross section of a surface layer, rapidly quenched using overlapping beam passes. (Optical micrograph).

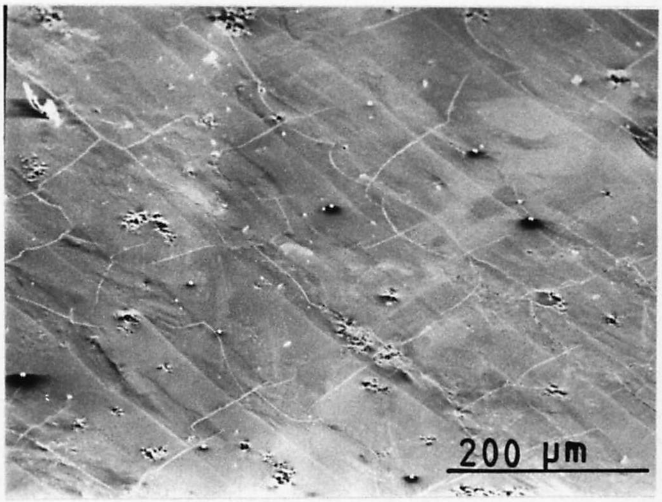

Fig. 5.49. The surface of the completely rapidly quenched area showing the cracks present.

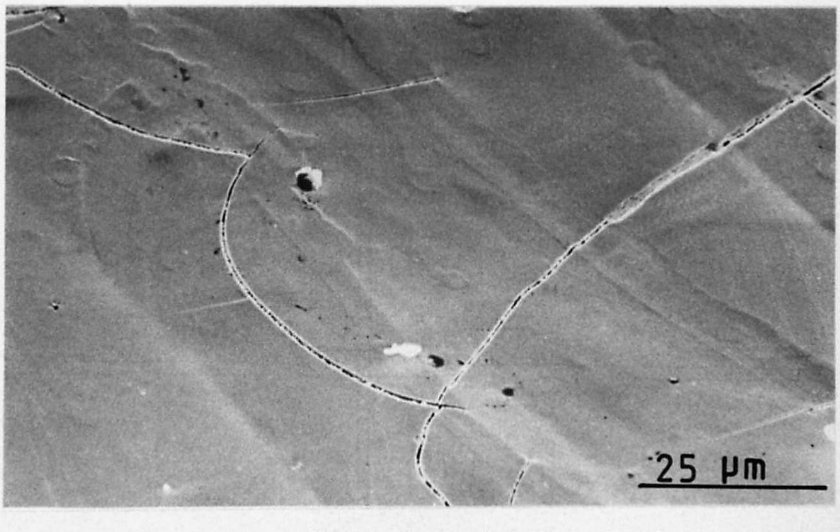

Fig. 5.50. Same surface shown in fig. 5.49., but at a higher magnification shows the cracks in otherwise smooth surface.

a few cracks were found even in the individual melt passes, but the increased amount of cracks observed in completely rapidly quenched surfaces indicate that the crystallization of amorphous layers enhanced the crack nucleation and propagation.

5.3. Other Alloys

Only a few metallic glasses of different compositions have been formed by laser or electron beam rapid quenching. In the present work, it was decided to introduce other alloying elements to $Fe_{80}P_{13}C_7$ alloy in order to produce different metallic glasses. Since metallic glasses containing chromium are expected to have better corrosion resistance, chromium was added to Fe-P-C alloy system in order to obtain $Fe_{70}Cr_{10}P_{13}C_7$ and $Fe_{60}Cr_{20}P_{13}C_7$ compositions and were subjected to electron beam rapid quenching. Detailed investigations such as on ultra high-strength steels and $Fe_{80}P_{13}C_7$ alloy were not undertaken with these compounds.

Low power electron beams (80-100W) were used to produce rapidly quenched surface layers on the as cast specimens of these alloys using traverse speeds in the range of 4.4 - 24.4 cm s^{-1}. Figures 5.51 and 5.52 show transverse cross sections of the melted regions of $Fe_{70}Cr_{10}P_{13}C_7$ and $Fe_{60}Cr_{20}P_{13}C_7$ alloys respectively. The structurelessness of the melted regions of both alloys were quite distinguishable. Even at higher magnifications no dendrites were observed. The average microhardnesses of the rapidly quenched regions of $Fe_{70}Cr_{10}P_{13}C_7$ and $Fe_{60}Cr_{20}P_{13}C_7$ alloys were ∿1070 VPN and ∿1092 VPN respectively. These values are higher than those of the $Fe_{80}P_{13}C_7$ metallic glass. The re-solidified areas of both alloys were free of cracks. It is known that the crystallization temperature of iron base metallic glasses increase with increasing chromium concentration (Naka et al 1975). Therefore amorphous Fe-Cr-P-C alloys have better properties than $Fe_{80}P_{13}C_7$ amorphous alloy.

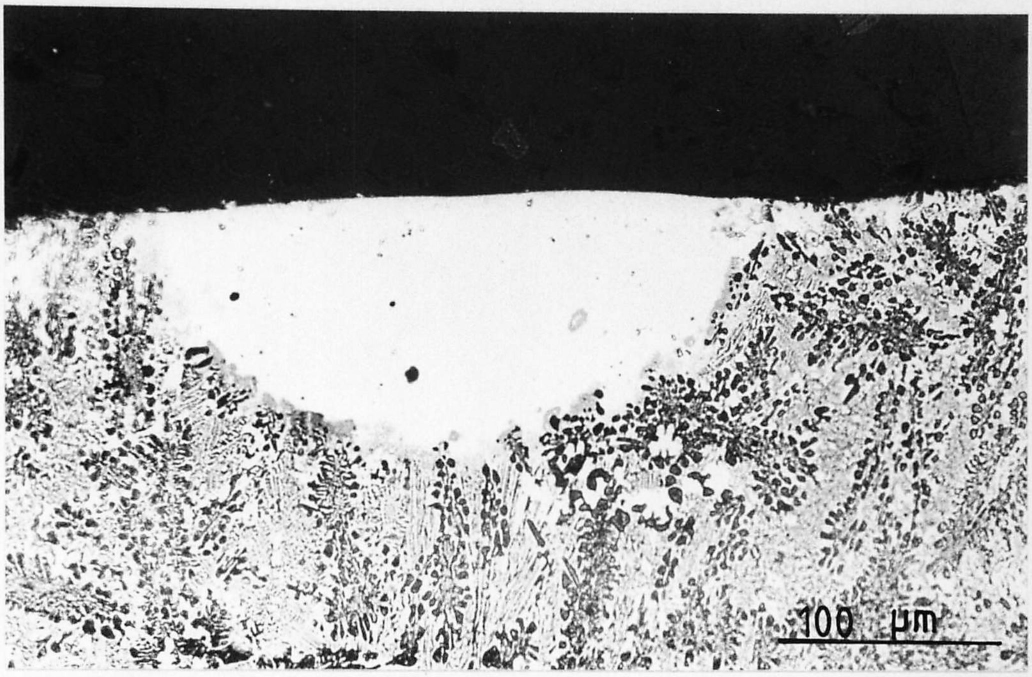

Fig. 5.51. A transverse cross section of electron beam rapidly quenched $Fe_{70}Cr_{10}P_{13}C_7$ alloy beam power - 100W, traverse speed - 24.8 cm s^{-1}

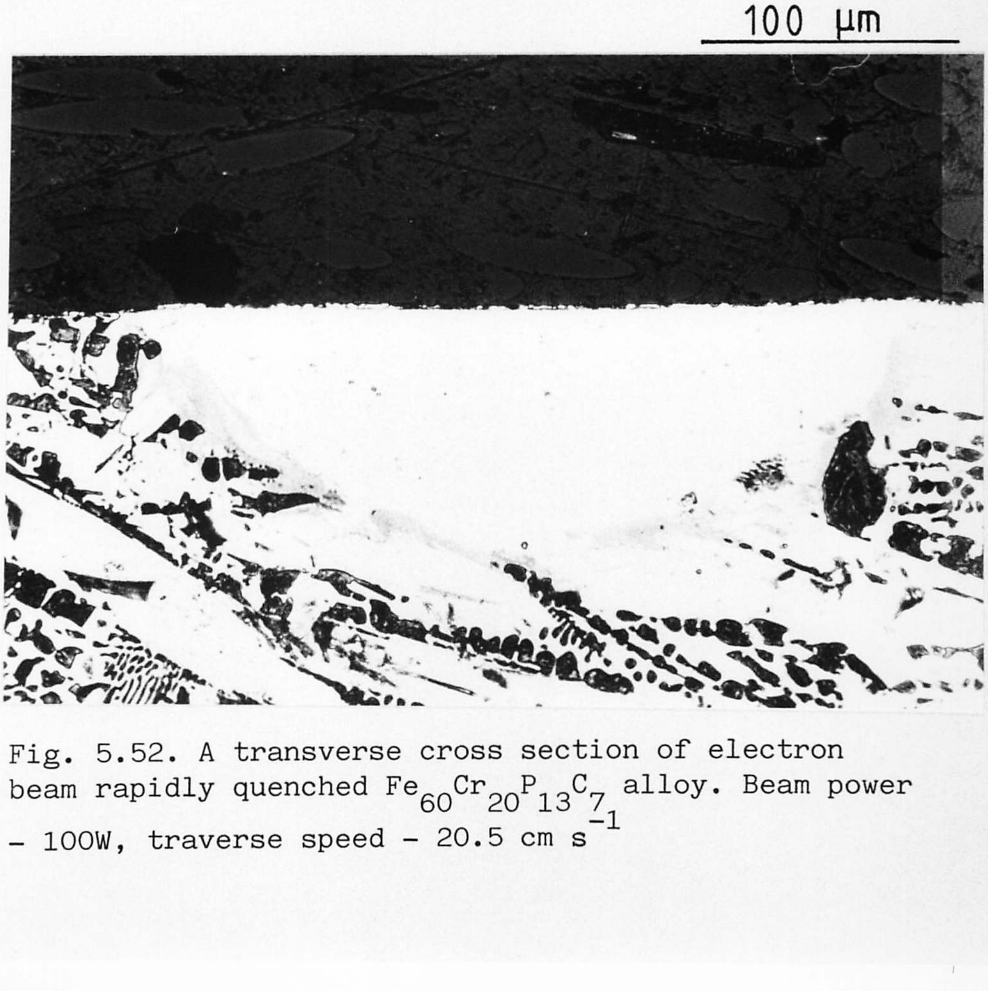

Fig. 5.52. A transverse cross section of electron beam rapidly quenched $Fe_{60}Cr_{20}P_{13}C_7$ alloy. Beam power - 100W, traverse speed - 20.5 cm s^{-1}

5.4. Conclusions

1. Electron beam melted regions of ultra high strength steel consisted of columnar and cellular dendrites. According to the relationship between cooling rate (r) and the dendrite arm spacing (d), $[\,d.r^{a} = c\,]$, cooling rates up to 2×10^{6} °C s^{-1} were found to be present during solidification.

2. Rapid quenching process led to a high degree of grain refinement.

3. Solid solubility in the melted region was increased with an inhibition of alloy carbide precipitation.

4. Lowering of M_s temperature due to increased solid solubility has favoured twinning in martensites since it is usually the preferred mode of lattice invariant shear at low transformation temperatures.

5. The increased solid solubility and the grain refinement effect resulted in an increase in retained austenite in surface quenched steel. Most of the retained austenite associated with twinned martensite regions were discontinuous in nature, probably because of the self-accommodation of adjacent twin related martensites.

6. The grain refinement, increased solid solubility and mainly martensitic structure associated with electron beam surface quenching of high strength steels led to a large increase in microhardness.

7. The microstructure and microhardness of melt spun high strength steel were very similar to those of surface quenched steel.

8. Surface tension gradients counteracted by the force of gravity in the melt pool, combined with high quenching rates caused fine ripples on the surface. The increased vapour pressure and the formation of a liquid bulge at the leading edge of the melt pool resulted in the formation of coarse ripples at high quenching rates.

— although enhanced corrosion resistance

9. The roughness of the surface decreased with increasing traverse speed at a constant beam power, while an increase in beam power at a constant speed, increased the roughness of the surface.

10. Overlapping beam passes were used to rapidly quench large surface areas of ultra high strength steels, without much change in the properties of the original melted areas due to heat effects of neighbouring passes.

11. Metallic glass layers were formed at the surface of $Fe_{80}P_{13}C_7$ alloy specimens by electron beam rapid quenching.

12. The areas near the substrate of rapidly quenched regions of $Fe_{80}P_{13}C_7$ alloy were crystalline. The microhardness of crystalline regions was higher than that of amorphous regions but the crystalline areas were brittle and susceptible to cracking. The amorphous phase being free of grain boundaries and brittle phases, has better mechanical properties.

CHAPTER 6.

6. Application of Surface Layers on Steel.

6.1. Introduction

In chapter 5 it was shown that the electron beam rapid quenching of crystalline materials (such as steels) would generally have a beneficial effect on the microstructure leading to an improvement of the mechanical properties of the material. Electron beam surface quenching of alloys, with a glass forming tendency, would form a metallic glass at the surface. With the present knowledge of metallic glasses as discussed in chapter 2, it can be expected that metallic glass surface layers have better mechanical, wear resistant and corrosion resistant properties due to their extreme homogeneity and the absence of grain boundaries.

Since metallic glass layers were successfully produced at the surface of bulk $Fe_{80}P_{13}C_7$ alloy specimens by electron beam rapid quenching method, efforts were made to produce $Fe_{80}P_{13}C_7$ glassy layers on the surface of ultra high-strength steel specimens. The techniques investigated to achieve this aim are as follows.

1. Application of the $Fe_{80}P_{13}C_7$ amorphous ribbons, (single and multiple layers) followed by electron beam rapid quenching.
2. Application of $Fe_{80}P_{13}C_7$ alloy powder layers with the use of a binder, followed by electron beam rapid quenching.
3. Plasma spraying of $Fe_{80}P_{13}C_7$ alloy onto the surface of steel followed by electron beam rapid quenching.
4. Sputtering of $Fe_{80}P_{13}C_7$ alloy onto the steel surface.

Microhardness of the layers, thus obtained, were examined whenever possible. Sputtered and surface clad layers were subjected to high temperature gas erosion experiments to examine the wear resistance. The above mentioned surface treatments and the property evaluation of the surface layers are described in this chapter.

6.2. Application of Melt Spun Amorphous Ribbons on Steel Surfaces

Since $Fe_{80}P_{13}C_7$ amorphous ribbons have been produced by melt spinning, efforts were taken to apply these ribbons on the surfaces of steel, in order to obtain clad amorphous surface layers. Pieces of melt spun ribbons were bonded to steel surfaces by spot welding both ends of the ribbons to the steel surfaces or by the use of a binder; Collodion. Electron beam rapid quenching was carried out with beam powers in the range of 100 - 150W with a speed of 4.4 cm s^{-1}.

Although the aim was only to clad the amorphous ribbons, electron beam quenching resulted in complete melting of the ribbons (thickness of ribbons $\sim$50-60μm) and a thin area of the substrate. Hence, the dilution effects were significant and all the re-solidified regions became crystalline. In order to reduce the dilution effects, experiments were repeated with the application of more than one layer of $Fe_{80}P_{13}C_7$ amorphous ribbons, prior to electron beam quenching. The lifting of ribbons from the surface due to the interaction with the beam was a problem. However, even when this problem was overcome by spot welding the ribbons to the surface at several places, the dilution effects were so great that no glass formation was achieved.

Fig.6.1 shows a cross-section of the melted area where three layers of ribbon were applied prior to rapid quenching. Unlike the re-solidified regions of ultra high strength steels (as discussed in section 5.1.2.), the dendritic structure of these rapidly quenched regions were very prominent due to the mixing of larger amounts of the

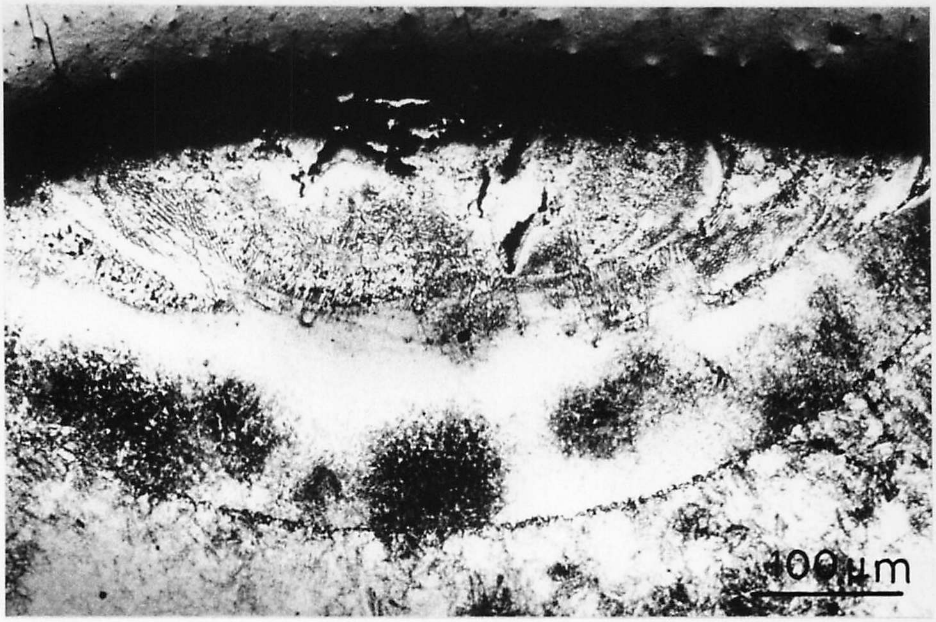

Fig. 6.1. A cross section of a melted area, where three layers of amorphous $Fe_{80}P_{13}C_7$ ribbons were applied prior to rapid quenching (Optical micrograph).

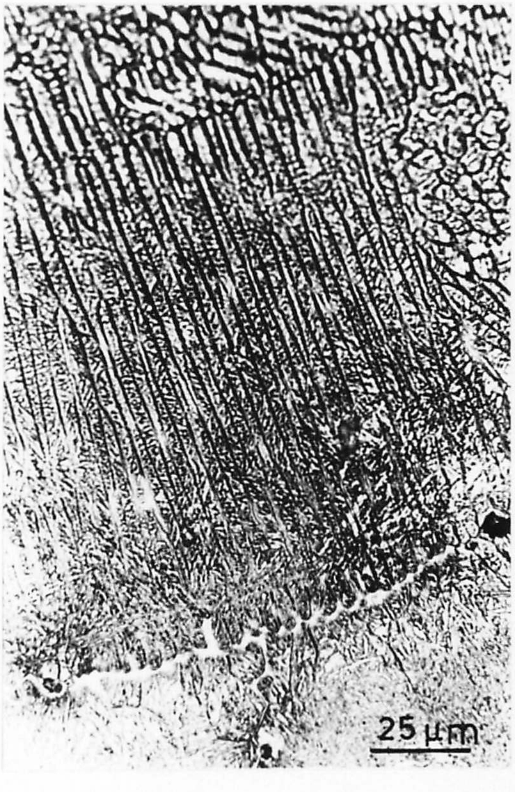

Fig. 6.2. A section of the rapidly quenched region of a sample, which is similar to one shown in fig.6.1, showing columnar dendrites (Optical micrograph).

alloying elements; phosphorous and carbon. Figure 6.2 is an optical micrograph taken at a higher magnification, showing a region of columnar dendrites, which grew from the interface between the melted and unmelted areas. There was always a tiny gap between the ribbons and the steel surface, resulting in proposity in the melted region. When multiple layers of ribbons were used, porosity in the melted region was more significant.

6.3. Surface Cladding of $Fe_{80}P_{13}C_7$ Powder Layers on Steel

6.3.1. Application of powder on steel surfaces.

Laser or electron beam rapid quenching of alloy powders on different substrate materials can be used to obtain the optimum process parameters which can later be used advantageously to clad better and methodically applied surface layers such as plasma sprayed or sputtered coatings. Not many studies have been reported on surface cladding of alloys. Steen and Courtney (1980) used laser beam surface melting to clad Co-29Cr-9W-1.8C alloy onto a Nimonic 75 (Ni-20Cr-0.4Ti-5Fe) substrate. Their work was on crystalline layers and no amorphous layers were expected. Tucker and Ayers (1981) produced rapidly quenched powder layers of a Ni-7Cr-2.8B-4.5Si-3Fe alloy on steel substrates. Prior to electron beam quenching, the powder layers were sintered at 1220K to provide sufficient particle-particle and particle-substrate bonding. However, where the properties of the substrate material should not be changed, sintering treatments cannot be undertaken. In the present work $Fe_{80}P_{13}C_7$ alloy powder was applied on steel substrates using a binder and electron beams were used to rapidly quench the surface.

The $Fe_{80}P_{13}C_7$ alloy was powdered (particle size 100-250μm) at Davy Loewy Ltd, Bedford.

For surface cladding, powders of particle size less than 100μm were used. Scanning electron micrographs of the powder (before the separation of particles with different sizes) are shown in fig.6.3.

The alloy powder was mixed with Collodion, and was spread on ultrasonically cleaned steel specimens. The effect of Collodion on the carbon concentration was assumed to be negligible. In order to measure the thickness of the powder layer, the wet mixture of powder was sandwiched between the steel specimen and a glass slide, both of pre-determined thicknesses. Since an objective of the study was to establish the processing conditions to obtain an amorphous $Fe_{80}P_{13}C_7$ layer, different thicknesses of the powder layer (0.2-0.6mm) were used.

6.3.2. Metallic Glass Layers by Rapid Quenching

Electron beams were used to clad the powder layers to the substrate. At each thickness, different electron beam power inputs (from 80W-200W) were employed. Specimens were traversed under the focussed electron beam at a constant speed of 4.4 cm s^{-1}.

The resulting rapidly quenched layers had various degrees of adherence to the substrate. A typical series of observations is shown in fig. 6.4. In this instance a beam power of 80W was used to rapidly solidify powder layers of 0.2, 0.4 and 0.6mm thick. At greater thicknesses ($\geqslant$ 0.6mm), the beam power was insufficient to melt the complete layer. Consequently, wetting of the substrate by the liquid alloy did not occur, resulting in the formation of droplets, which did not adhere to the substrate at all. At medium thicknesses,

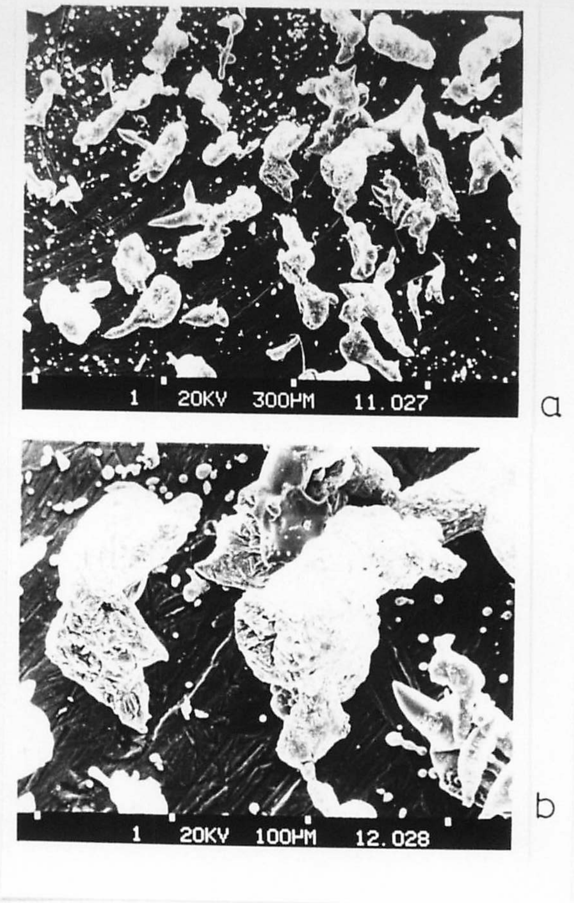

Fig. 6.3. The $Fe_{80}P_{13}C_7$ alloy powder, before the separation of particles with different sizes. Figures a and b show different magnifications (SEM)

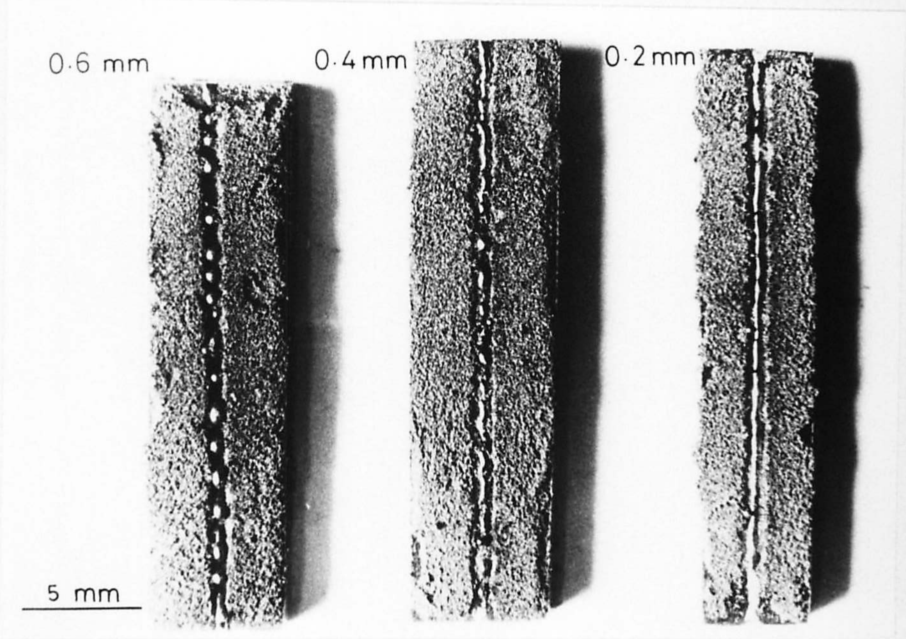

Fig. 6.4. Electron beam rapidly quenched $Fe_{80}P_{13}C_7$ powder layers showing the effect of the thickness of the coating. Beam power 80W, traverse speed 4.4 cms^{-1}

the rapidly quenched layers were discontinuous in nature, some parts being adhered to the substrate and some not. (see 0.4mm thick layer in fig. 6.4). Figure 6.5 shows a transverse cross section of a poorly adhered globule found in that layer. Some areas were featureless but the crystalline nature of some areas were quite obvious.

However, an optimum thickness, at which the powder layer was rapidly quenched forming apparently well adhered continuous layer was found at each different beam power. In the case of 80W beam power, the ideal thickness was 0.2±0.02mm as shown in fig.6.4. The cross section of this layer had an approximately semi-circular shape (fig.6.6) due to the surface tension effects of the liquid metal at the time of the solidification. The power was enough to melt the powder layer without melting much of the substrate. Even at higher magnifications, no structure was observed in most of the areas of the clad layer. evidence for any crystallinity was found only in the area near the interface of rapidly quenched layer with the substrate.

Fig.6.7 shows the effect of different beam powers on a constant melt depth. In this instance 0.2±0.02mm thick layer was subjected to beam powers in the range of 80W to 150W. Melted and resolidified areas formed continuous trails (as distinct from trails of globules and had taken approximately semi-circular cross-section due to high surface tension of the liquid alloy. At relatively higher beam powers (>100W), comparatively large areas of the substrate underneath the coating were melted and the resolidified areas were crystalline. The cross sections of the layers melted with 100W and 150W beam powers, show overall dendritic structues (fig.6.7). The crystallization of the resolidified region is due to the following reasons.

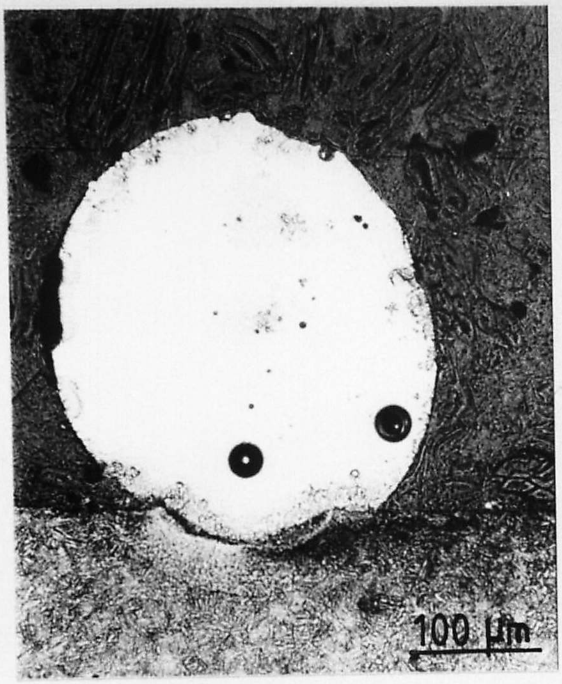

Fig. 6.5. A transverse cross section of a poorly adhered globule found in 0.4mm thick layer. (optical micrograph)

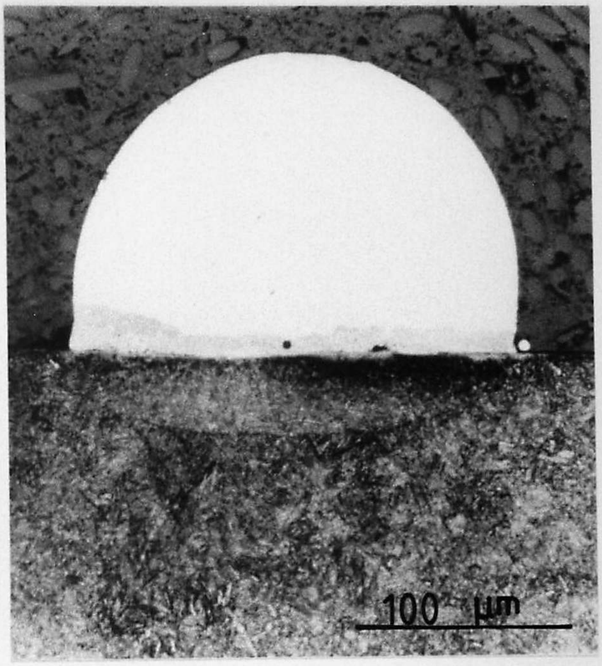

Fig. 6.6. A cross section of a well adhered layer. Thickness of the coating = 0.2mm (optical micrograph)

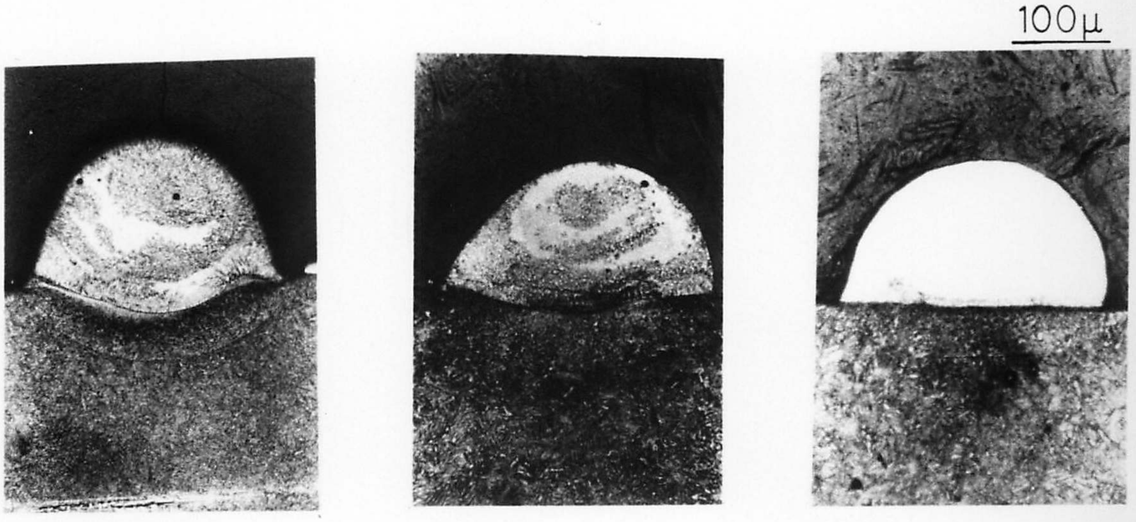

150 W 100 W 80 W

Thickness of coating = 0·2 mm
Traversing speed = 4·36 cm/s

Fig. 6.7. The effect of different beam powers on the same powder coating. (Optical micrographs).

1. The change of the glass forming composition as a result of the dilution of the $Fe_{80}P_{13}C_7$ alloy by the steel substrate.
2. The lower cooling rate of increased power inputs as a direct result of the higher amount of heat energy which had to be transferred to the substrate.

At a power level of 80W, a 0.2mm thick powder layer was well adhered to the substrate after rapid quenching and appeared non-crystalline. Even at higher magnifications, this layer did not reveal any crystalline structure except in the area close to the substrate.

Due to the thin nature of these surface layers, it was difficult to confirm the amorphous nature by X-ray or electron microscopy techniques. The average microhardness of the structureless resolidified layers varied from ∿880 VPN near the surface to about 1150 VPN near the substrate. Fig. 6.8 shows the variation of microhardness of the rapidly quenched layer (80W) shown in fig. 6.7. The microhardness in the vicinity of the surface was close to the microhardness of $Fe_{80}P_{13}C_7$ amorphous layers (∿910 VPN) obtained by electron beam quenching (discussed in section 5.1.4.5). A difference in the cooling rates or the presence of unresolved fine pores in the rapidly quenched powder layer may have caused the observed reduction in microhardness. However, higher values of the microhardness would have been expected if the layer was crystalline. The increase in microhardness near the interface is due to the crystallinity of the layer. The heat affected zone of the steel substrate had a microhardness of about ∿790 VPN due to the martensitic nature of that region. Microhardness of amorphous and crystalline $Fe_{80}P_{13}C_7$ phases were discussed earlier in section 5.2.2.

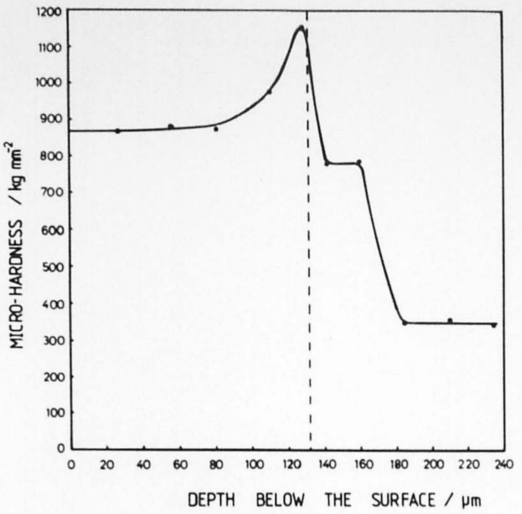

Fig. 6.8 The variation of the micro-hardness of rapidly quenched $Fe_{80}P_{13}C_7$ powder layer (80W power, 0.2mm thickness) with the depth below the surface.

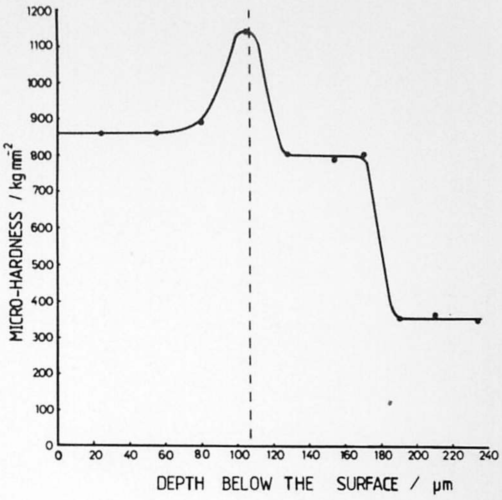

Fig. 6.10. The variation of micro-hardness of the layer shown in fig.6.9b, with the depth below the surface.

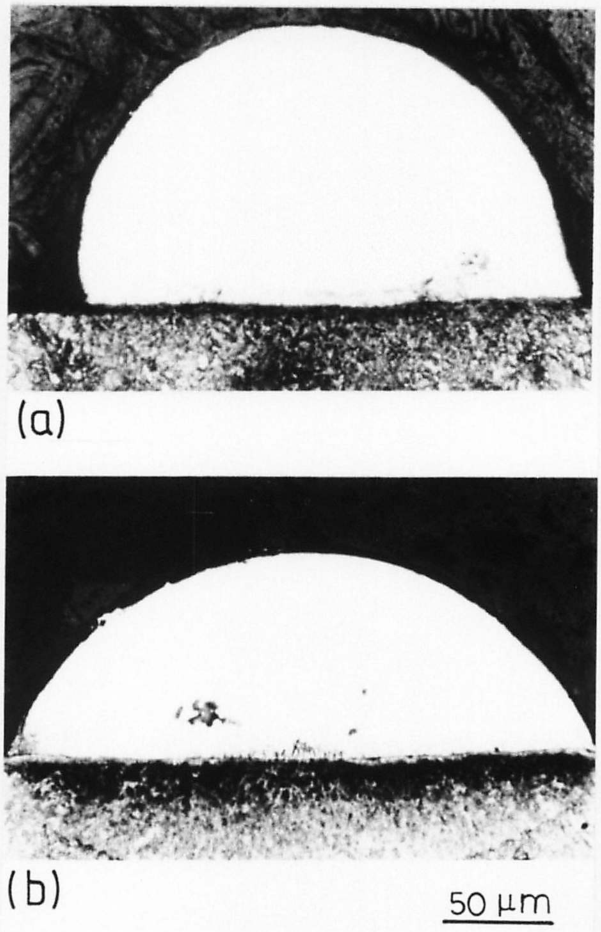

Fig. 6.9.
(a) A cross section of the rapidly quenched $Fe_{80}P_{13}C_7$ powder layer (80W power, 0.2mm thickness, 4.4 cm s^{-1} traverse speed)
(b) A cross section of the same layer, after rapid quenching again

As a result of the powder layer being loosely packed, displacement of the powder to both sides of the passage of the beam occurred. Consequently it was not possible to rapidly quench the whole surface area by overlapping passes.

These amorphous melt regions were rapidly quenched again by subjecting them to electron beam surface melting, in order to investigate whether the layers would retain the amorphous nature. It was expected that the rapid quenching of the amorphous area would be similar to the exposure to a momentary heat pulse; a condition, the inner surface of a gun barrel is subjected at each firing. The specimens were traversed at 4.4 cm s^{-1} under an electron beam of 80W power. Fig.6.9a shows the 0.2mm thick layer after surface melting and fig. 6.9b shows the same layer after rapid quenching again. The melted area was spread on the substrate by the second pass. Most of the area in the vicinity of the surface remained structureless. The variation of microhardness with the depth below the surface was similar to that observed in the original rapidly quenched layer., (fig. 6.10).

Fig. 6.11 shows the results of energy dispersive X-ray (EDX) analysis of phosphorous and nickel in the original melted layer and the same layer after remelting. It should be noted that the analysis was carried out, assuming that there was no carbon but only phosphorous nickel and iron present in the alloy. Consequently the quantitative values are not accurate but these results show the main trend in the variation of the concentration of the elements. After remelting the phosphorous content in the rapidly quenched region was slightly reduced. An important observation is that actual dilution of the powder layer with the substrate has occurred only in a very thin region (∿20μm) at the interface. At ∿5-10μm below the interface the phosphorous concentration in the substrate was almost negligible and nickel

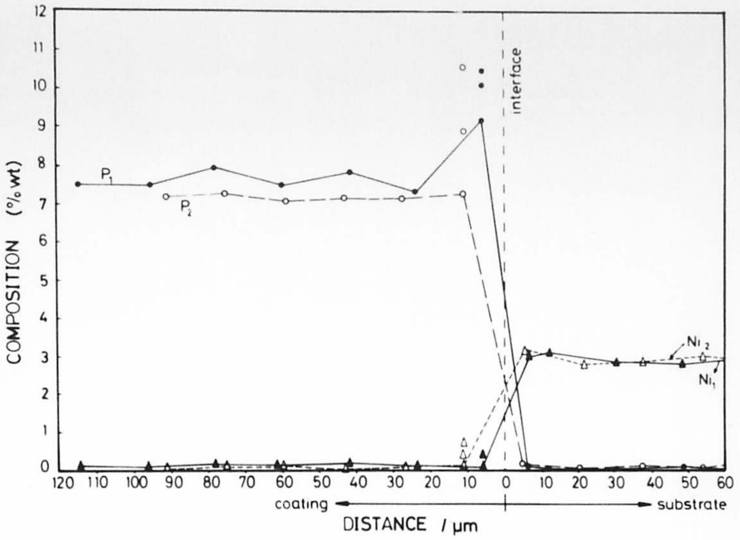

Fig. 6.11. Phosphorous (P_1 and P_2) and nickel (Ni_1 and Ni_2) in rapidly quenced layers shown in fig 6.9a (P_1, Ni_1) and fig. 6.9b (P_2,Ni_2)

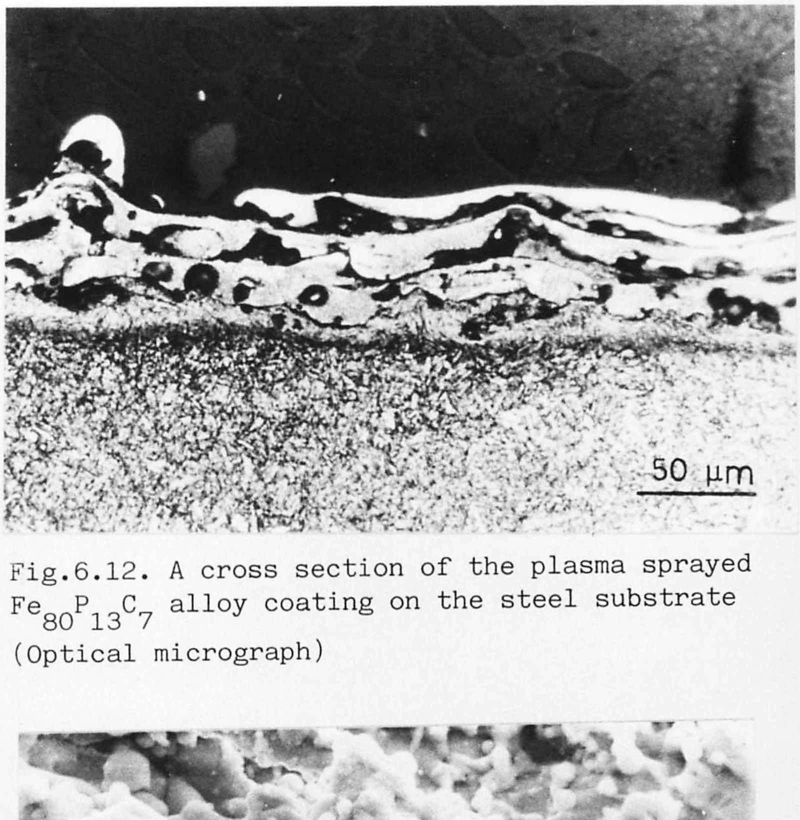

Fig.6.12. A cross section of the plasma sprayed $Fe_{80}P_{13}C_7$ alloy coating on the steel substrate (Optical micrograph)

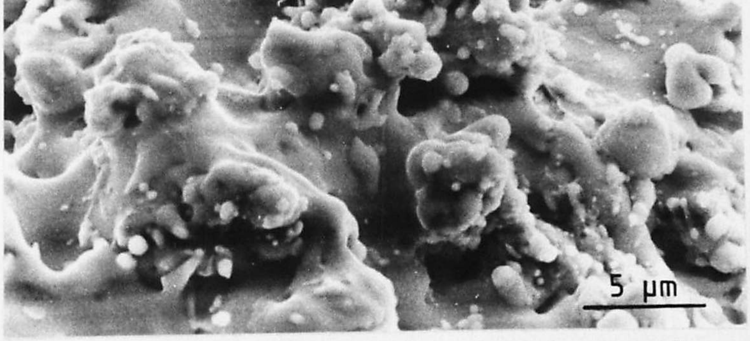

Fig. 6.13 The surface of the plasma sprayed $Fe_{80}P_{13}C_7$ alloy layer (SEM)

could be traced only in a thin alloy layer of about 10μm above the interface. The dendrites observed in the rapidly quenched layer contained above average levels of phosphorous and nickel.

It may be concluded that the application of an alloy powder of a glass forming composition, on steel, followed by electron beam rapid quenching could be used to produce amorphous layers on steel substrates. When the process parameters were optimized, the alloys could be clad with a minimal dilution with the substrate at the interface.

6.4. Rapid Quenching of Plasma Sprayed Layers

6.4.1. Plasma Deposition of $Fe_{80}P_{13}C_7$ Alloy Layers

The semi-circular shape of electron beam rapidly quenched layers and the inability to rapidly quench large surface areas were two main disadvantages of electron beam quenching of loose powder layers. Both these disadvantages were caused by the fact that the powder layers were not well adhered to the substrate, prior to surface melting. Therefore efforts were concentrated on methods by which coatings of even thicknesses could be made well bonded to the substrates. Plasma spraying was one of the methods investigated.

The $Fe_{80}P_{13}C_7$ alloy powder described in section 6.3 was used in plasma spraying, which was carried out at AERE, Harwell. Details of the process parameters used for plasma spraying the $Fe_{80}P_{13}C_7$ alloy powder onto high-strength steel substrates were as follows.

Gun - Metco type 3MB

Nozzle - GH (medium spray cone, medium velocity)

Voltage- 72V

Current- 400A

Power - ∿49kW

spray distance - 130mm

spray rate - 76g /minute

Argon was blown over the substrates during the coating process, in an attempt to reduce the level of any oxidation.

The thicknesses of the plasma sprayed coatings were in the range of 60–70μm. However, the coating was found to be very porous due to the fact that the plasma spraying process was carried out in ambient atmosphere. Fig.6.12 shows a cross section of the plasma sprayed Fe–P–C alloy coating. The volume fraction of porosity in the deposited layer was estimated by measuring the area fraction of porosity, and it was found to be in the range of ∿44 - 48%. The amount of porosity was much greater than expected. The deposition of gas bubbles, attached to depositing sprayed particles is mainly responsible for the porosity, which would have been greatly reduced or completely avoided if the process was carried out in a reduced pressure atmosphere or in vacuum. Due to the large amount of porosity in the layer, accurate micro-hardness measurements could not be made. A scanning electron micrograph of the typical plasma sprayed surface is shown in fig.6.13. The presence of pores open to the surface resulted in a rough surface.

Electron probe micro-analysis (EPMA) of the original $Fe_{80}P_{13}C_7$ alloy powder and the plasma sprayed layer was carried out to compare the compositions of the alloy before and after plasma spraying and to examine the homgeneity of the coating. Micro-analysis of phosphorous, carbon and iron was carried out at RARDE, Fort Halstead and the methods used are described in appendix 2.

Results obtained are as follows.

	%wt. P	%wt. C
Fe-P-C alloy powder used for plasma spraying	∿ 8.0	∿ 0.83
plasma sprayed coating	∿ 6.1-6.9	1.6-2.2

The accuracy of the carbon content is less certain (vide appendix 2) but the analysis shows that the phosphorous content was reduced by 1-2%wt. during the plasma spraying process. This suggests the possible presence of other elements such as oxygen, but the concentrations of these elements were not analysed. The concentrations of elements did not vary across the coating, suggesting that the layer was homogeneous.

Plasma spraying is usually a technique, which combines melting, quenching and compacting in a single operation. Calculations of heat transfer between a plasma jet spray droplet and a highly conducting metal surface indicated cooling rates of the order of 10^7 °C/sec (Moss 1968). The extension of solid solubility and the presence of metastable phases in plasma sprayed silver alloys were reported by Moss and Young (1964). Extended solid solubility found in aluminium-vanadium alloys were also reported by Moss (1968) and Moss and Schulster (1969). A metastable form of Al_2O_3 was produced by plasma spraying (Mcpherson 1973) and supersaturation in the TiO_2-Cr_2O_3 (Barry et al. 1968) and Al_2O_3-Cr_2O_3 (Mcpherson 1973) mixtures also have been achieved by this technique. The cooling rates obtained in plasma jet spraying, reported by Moss (1968) is high enough to produce amorphous phases in suitable glass forming alloys. The production of amorphous metals by plasma spraying was reported by Giessen et al. (1977), who have produced 0.75mm thick amorphous $Zr_{40}Cu_{60}$ sheets in a controlled atmosphere.

However in the present work, X-ray diffractometry results confirmed that the plasma sprayed Fe-P-C coatings were crystalline. The Fe_{α}, Fe_3C and Fe_3P phases were detected in X-ray intensity traces. The composition change occurred during plasma spraying, or the low cooling rate caused by the large amount of porosity affecting the heat transfer from plasma sprayed particles to the substrate has made the Fe-P-C layer crystalline. The influence of a range of variables such as powder size, substrate conductivity and preparation, gas flow rate and arc power is important for the nature and quality of plasma sprayed layers. Several workers (e.g. Shankar et al. 1981) have reported the investigations on these variables but in the present work it was not possible to study these variables in detail.

6.4.2. Electron Beam Surface Melting.

Plasma sprayed layers were subjected to electron beam surface melting, with the aim of densifying the porous layers and producing metallic glass layers by rapid quenching. Since the layers were very thin, the surface melting was carried out using only low power beams of 40-100W with traverse speeds in the range of 4.4-30.4 cm s^{-1}. Both single and multiple melt passes were made. Figures 6.14 and 6.15 show transverse cross sections of rapidly quenched regions, under different processing parameters. In the melted region shown in fig.6.15, it can be seen that the processing parameters used were just enough to melt the plasma sprayed layer and clad it to the steel substrate without melting too much of the substrate. This ideal situation minimises the dilution of the alloy layer with steel.

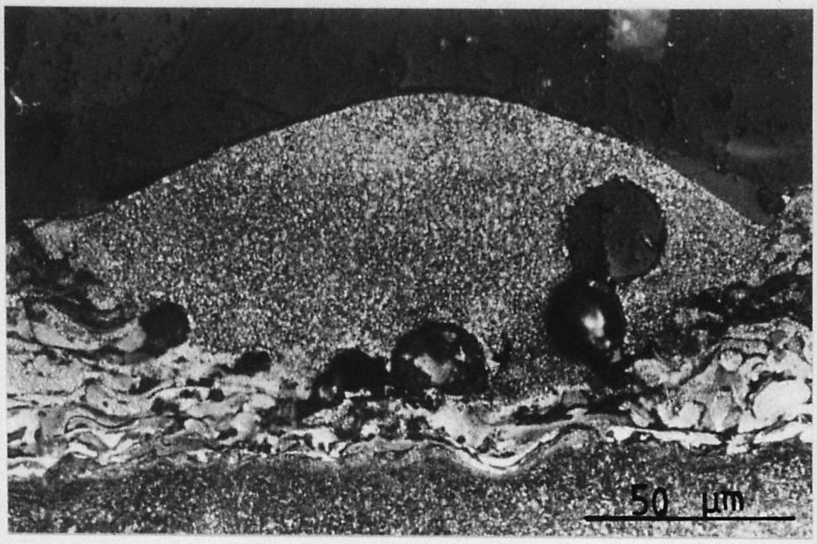

Fig.6.14. A transverse cross section of rapidly quenched region of plasma sprayed $Fe_{80}P_{13}C_7$ layer. Beam power - 40W, traverse speed - 11.4 cm s^{-1}. (Optical micrograph)

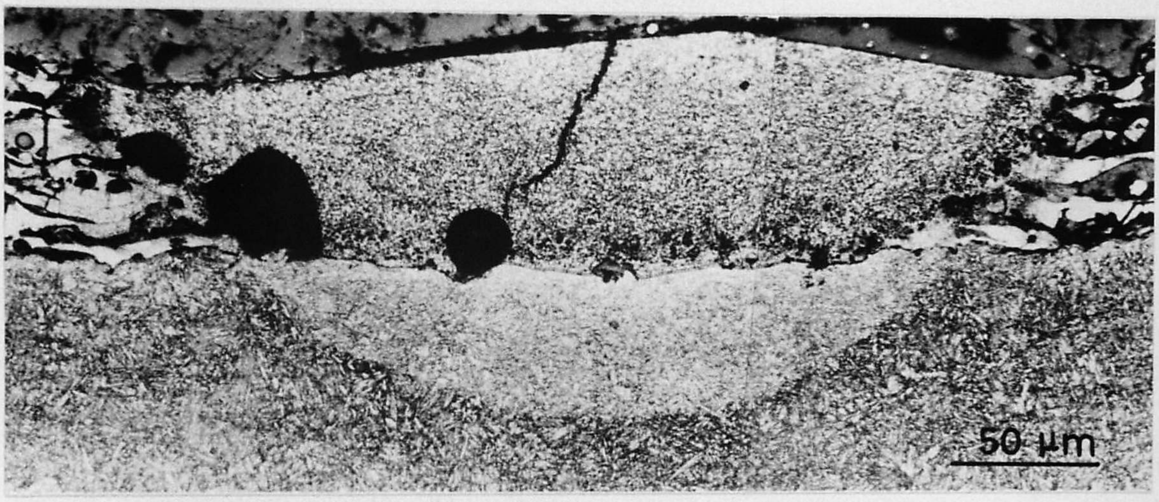

Fig.6.15. A transverse cross section of a rapidly quenched region of plasma spayed $Fe_{80}P_{13}C_7$ layer. Beam power - 50W, traverse speed 4.4. cm s^{-1}. (Optical micrograph).

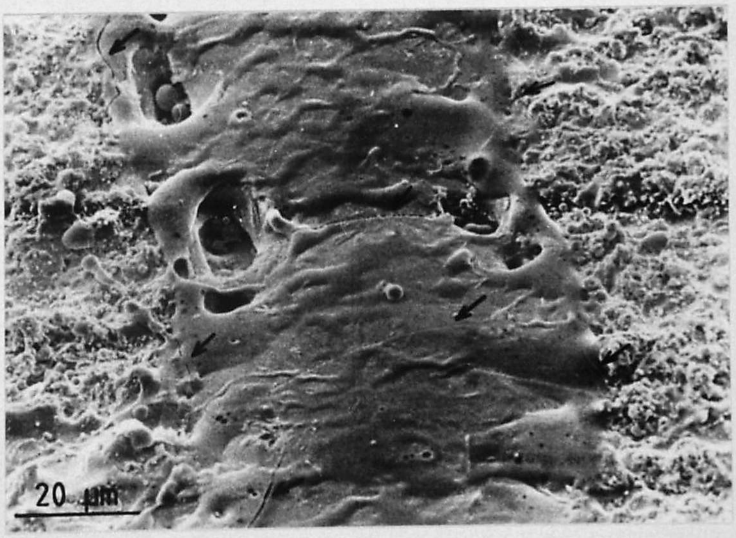

Fig. 6.16. The surface of the rapidly quenched area (a single pass) of the plasma sprayed layer. Arrows indicate the cracks. (SEM)

6.4.2.1. Surface Cracks.

Cracks were present frequently in the surface melted regions. These cracks did not spread usually to the substrate although some cracks were observed in the unmelted areas of the plasma sprayed layer near the melt/solid interface (fig.6.15). Thermal stresses produced during the rapid solidification has lead to the formation of cracks in the crystalline region. The porosity present in this region (discussed in the next section) has enhanced the propagation of cracks. It was observed that most of the cracks were associated with pores. Fig.6.16 is a scanning electron micrograph of the electron beam rapidly quenched area (a single pass) of a plasma sprayed layer. The surface was apparently rougher than the electron beam quenched surface of bulk $Fe_{80}P_{13}C_7$ alloy, (vide section 5.2.3). This roughness has been caused by the turbulance due to the gas movements and the expulsion of gas at the surface. There was no particular pattern of the presence of cracks, which were found all over the resolidified surface. In fig.6.16 the arrows indicate the presence of cracks.

Figure 6.17 shows scanning electron micrographs of the surface of a plasma sprayed layer before and after surface melting of the whole surface using overlapping passes. Consolidation of the porous layer occurred by surface melting. However, the widely spread cracks were still present.

6.4.2.2. Porosity

By optical microscopy it was observed that all surface melted areas of plasma sprayed layers were crystalline. The change of composition could be a possible factor for the crystallization of the melt during the solidification. However, since amorphous

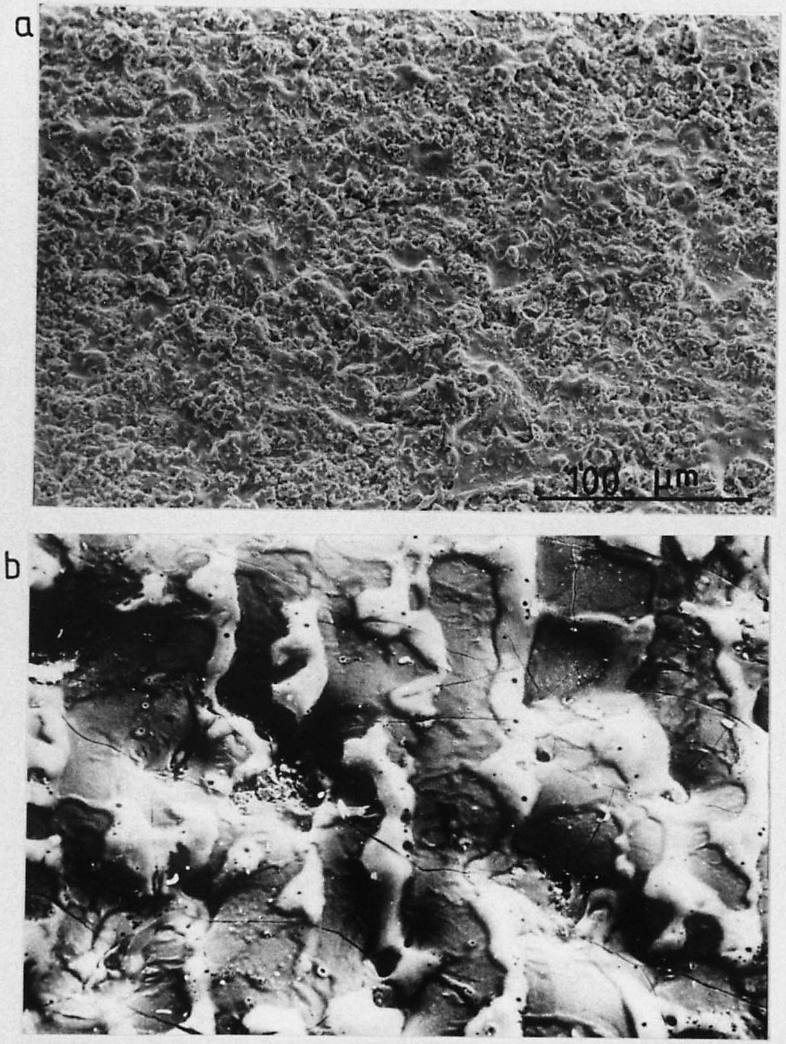

Fig.6.17.
(a) The surface of the plasma sprayed $Fe_{80}P_{13}C_7$ alloy layer, (SEM).
(b) The same layer after electron beam quenching, using overlapping passes (SEM)

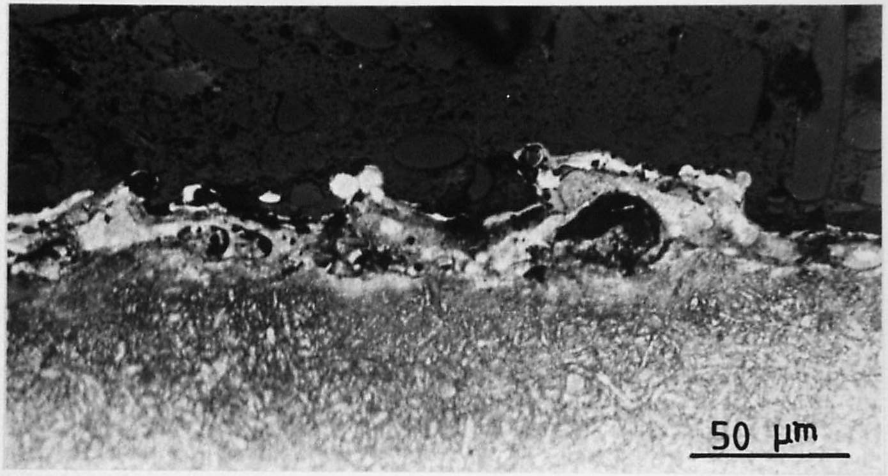

Fig. 6.18 A cross section of the plasma sprayed $Fe_{80}P_{13}C_7$ layer, after keeping at 750°C for 24 hours.

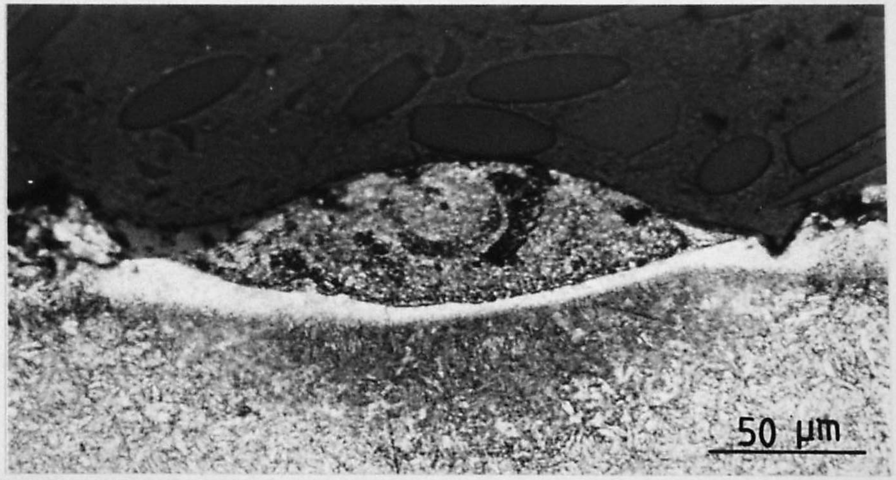

Fig.6.19. A cross section of the electron beam rapidly quenched region of the layer shown in fig.6.18

Fe-P-C alloys of different compositions have been produced by other workers (as discussed in chapter 2), in this instance, the poor heat transfer properties of the layer due to porosity,affecting the cooling rate was probably the most responsible factor for the crystallisation of the rapidly quenched layer. Due to the heat obtained from the electron beam, the temperature and pressure of the gases trapped within pores increase and the gas escapes from the layer. The presence of a large amount of gas and the movement of gas in the layer would adversely effect the heat conductivity within the layer, thus decreasing the cooling rate. Some of the gas bubbles formed in the melt were trapped during the rapid solidifcation and could be observed in most of the melted areas (Fig.6.14 to 6.15).

Efforts were made to force out the trapped gas from the plasma sprayed layers by heating in vacuum prior to electron beam surface quenching. Although this possibility was investigated, it should be noted that the substrate also would be affected by this heat treatment, so that it can be only applied where a property change of substrate is acceptable.

Plasma sprayed steel specimens were sealed in vacuum in silica glass tubes and were heated gradually from room temperature to 750°C and were kept at that temperature for 24 hours. With the increase in temperature, expulsion of trapped gases occurred blowing off some of the coating. After the heat treatment, a large amount of powder particles, which had been removed from the coating was observed inside the glass tube. Figure 6.18 shows the plasma sprayed layer after the heat treatment. Due to the very thin nature of the layer (after the heat treatment), it was difficult to rapidly quench only the layer. Often electron beam melting resulted in melting the substrate as well, thus changing the composition of the layer and reducing any chance of making the layer amorphous. Fig. 6.19 shows an area, which was electron beam melted after the heat treatment.

Since there was a loss of about 1-2%wt. phosphorous and a probable loss of carbon during the plasma spraying, it was decided to use a Fe-P-C alloy powder with higher phosphorous and carbon concentrations in order to compensate any losses during plasma spraying. For this purpose, an alloy was made with average concentration of 9.8%wt. phosphorous and 1.88% Carbon. The powder of this alloy was used to obtain a plasma sprayed coating on steel. Phosphorous content of the coating was analysed by EDX analysis and found to be 9.1%wt. (Not analysing carbon, but after normalising. For qualitative assessment only).

However, by X-ray diffractometry it was found that this layer was crystalline, results being similar to that of the first plasma sprayed layer. Porosity was still present extensively. Surface melting using electron beams produced crystalline regions, which were quite distinguishable by optical microscopy. Figures 6.20 and 6.21 show cross sections of a single pass and an overlapping multiple pass electron beam treated areas of the plasma sprayed coating respectively. These experiments confirmed that it was not the change of composition but it was possibly the reduced cooling rate, caused by the poor heat transfer properties of the layer which was responsible for the crystallisation of the plasma sprayed Fe-P-C layers on rapid quenching.

It may be concluded that the porosity, in the plasma sprayed layer is a major disadvantage in obtaining amorphous layers by plasma spraying process itself or even after electron beam rapid quenching. All the variables, which effect the quality and the nature of plasma sprayed coatings were not studied but it may be assumed that plasma spraying in a low pressure atmosphere or in vacuum would lead to a

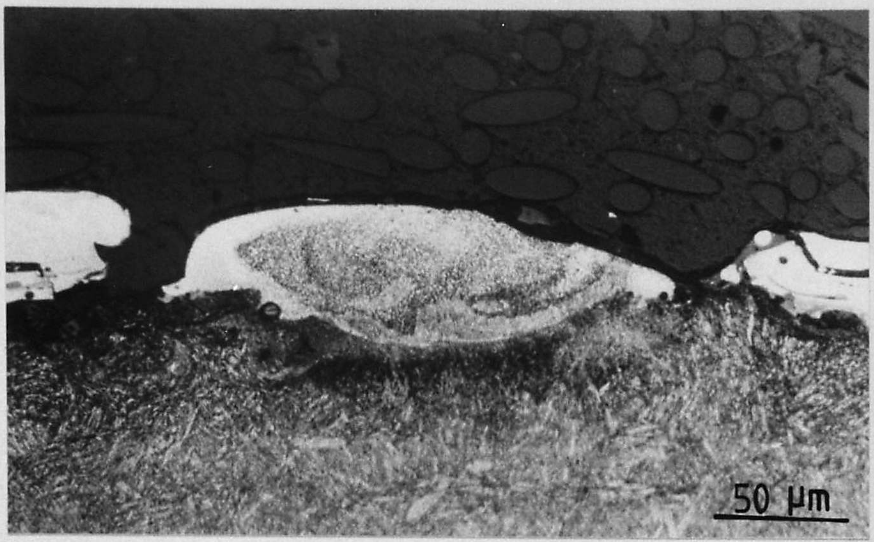

Fig. 6.20 A transverse cross section of the electron beam quenched region (single pass) of plasma sprayed Fe - P - C alloy powder layer with higher phosphorous concentrations.

Fig. 6.21. A transverse cross section of the electron beam rapidly quenched region (overlapping multiple passes) of plasma sprayed Fe - P - C powder layer with higher phosphorous and carbon concentrations.

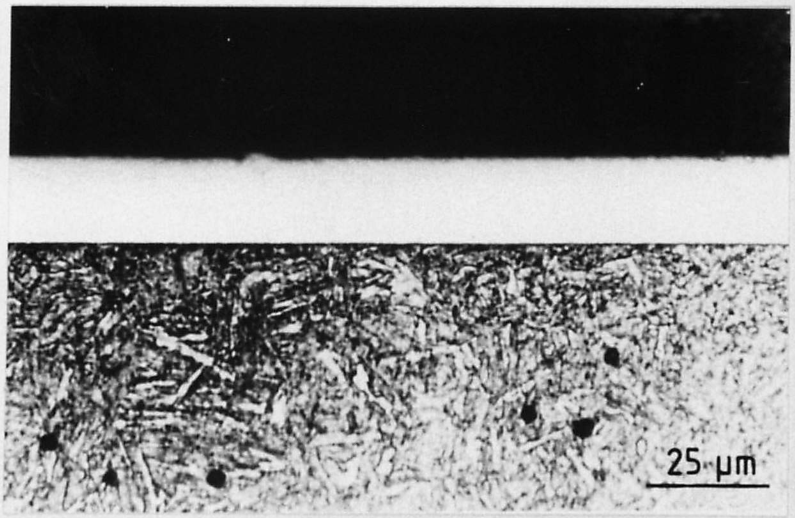

Fig. 6.22. A cross section of the sputtered $Fe_{80}P_{13}C_{7}$ layer.

lesser amount of porosity in the coatings and would have improved the quality of the layer.

6.5. Sputter Deposition of $Fe_{80}P_{13}C_7$ Alloy Layers.

6.5.1. Amorphous Layers by Sputter Deposition

Since the higher vapour quenching rates associated with sputtering, promote the formation of metastable structures and amorphous phases (Cantor and Cahn 1975, Dahlgren 1978) it was decided to use sputtering process as a possible means of producing amorphous layers on steel substrates. On the other hand sputtering being a technique which can be used to coat relatively large surface areas, the correct alloy composition and process parameters would yield a large surface layers of metallic glass.

Specimen preparation and the employed direct current sputtering process were described in section 3.4. Layers were deposited at a rate of ∿0.5 - 1.5°A per second. The thicknesses of thin films obtained were in the rate of ∿10 - 17μm. Figure 6.22 shows a cross section of sputtered $Fe_{80}P_{13}C_7$ layer on steel. When the process parameters were optimised, an apparently well adhered, pore free layer was obtained. When 2% Nital, which would usually etch $Fe_{80}P_{13}C_7$ alloy was used, the layer appeared structureless. Microhardness of relatively thicker layers were measured using a 50g load.

The average microhardness was found to be ∿920 VPN, which was approximately similar to that of melt spun $Fe_{80}P_{13}C_7$ amorphous ribbons. (∿925 VPN).

During each sputtering experiment on ultra high strength steel surface, a $Fe_{80}P_{13}C_7$ layer was sputtered simultaneously on a sample of NaCl or KCl. By dissolving the salt, it was possible to obtain layers suitable to investigate by transmission electron microscopy, which confirmed that sputtered $Fe_{80}P_{13}C_7$ layers were amorphous. The diffraction pattern of these sputtered films consisted of only one diffuse ring; a characteristic of amorphous materials (figure 6.23). Fig. 6.24 is a bright field electron micrograph of the thin layer showing the usual amorphous structure.

6.5.2. Growth Defects

The sputtered layer was apparently well adhered to the substrate but it was not free from growth imperfections and voids. Fig.6.25 shows a cross section of the layer with areas in which preferential deposition has occurred due to 'impurities' or 'foreign' particles. The growth of thin films is affected even by the smallest impurity particle. When there is an impurity particle on the substrate surface, it has a shadowing effect on the surface of the layer around it. The sputtered particles from the target tend to deposit on the impurity particle preferentially . Consequently the growth on that particle occur at a higher rate. Preferential deposition can be initiated by an impurity particle on the surface prior to the beginning of sputtering (marked a in fig. 6.25) or even by impurity particles deposited during sputtering (marked b in fig 6.25).

It may be relatively easier to avoid the preferential deposition due to impurities on the substrate suface by prolonged and thorough ultrasonically cleaning and sputter-etching the surface prior to sputter deposition. However the avoidance of preferential deposition due to impurities deposited during sputtering is more complicated. The 'foreign' or 'impurity' particle can be any particle other than the usual sputtered material from the target. One problem encountered in sputtering is the failure of the sputtered deposits to stick on other items inside the chamber. e.g. on shields etc. Sputtered material collected elsewhere other than the substrate, can fly off in small

Fig. 6.23.
The electron diffraction pattern obtained from the sputtered $Fe_{80}P_{13}C_7$ layer, showing that the layer was amorphous.

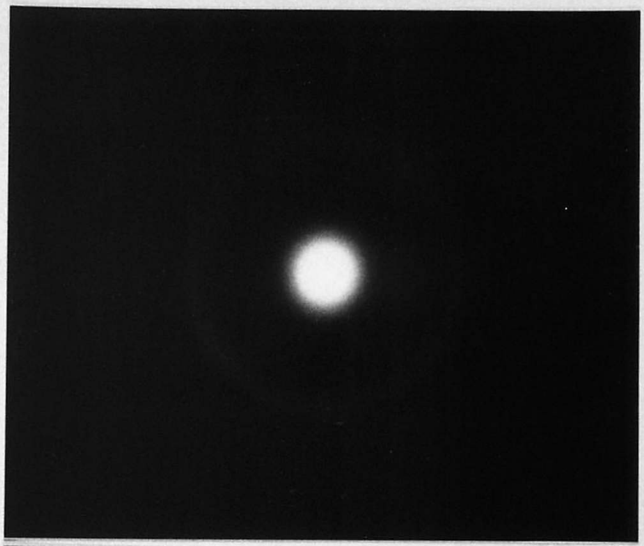

Fig. 6.24.
A bright field electron micrograph of the sputtered layer.

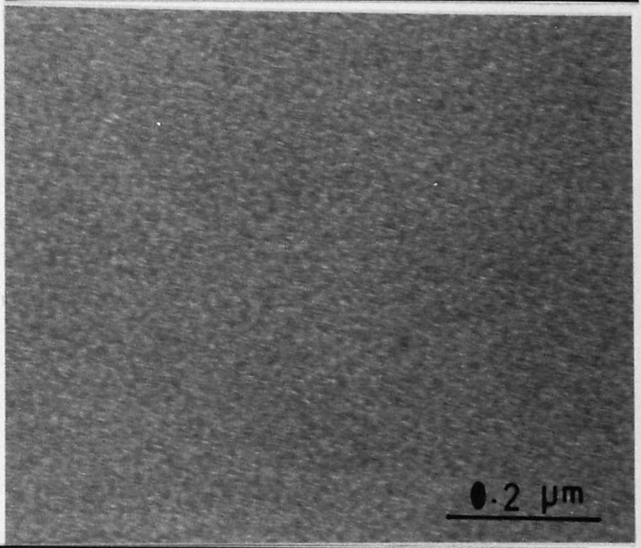

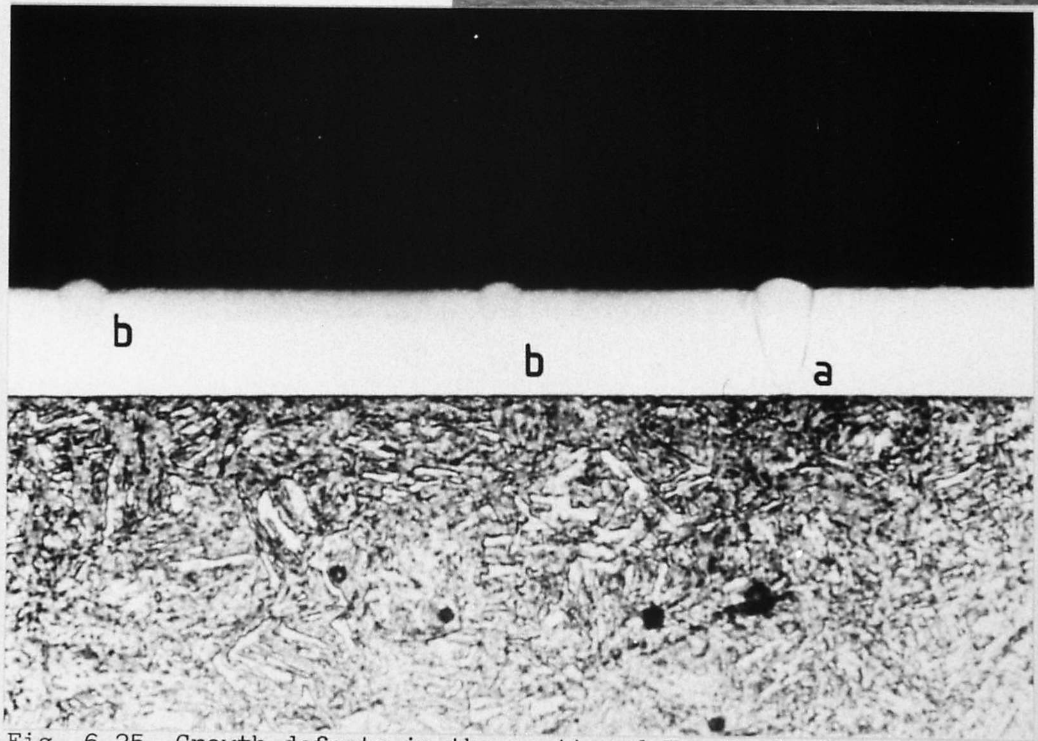

Fig. 6.25. Growth defects in the sputtered $Fe_{80}P_{13}C_7$ layer. The areas of preferential deposition, initiated by impurities, prior to beginning (marked a) and by impurities deposited during sputtering (marked b) are shown. (optical micrograph)

pieces during sputtering due to the lack of adherence or the release of internal stresses. Some of these materials can deposit on the substrate surface, initiating the preferential deposition. Steps should be taken to avoid this problem. The adherence of stray materials can be improved by allowing the shields to run at elevated temperatures in order to reduce stresses and to enhance the diffusion at interface.

A scanning electron micrograph of the surface of the sputtered $Fe_{80}P_{13}C_7$ layer is shown in fig.6.26. The diagonal lines on the micrograph, are some remaining polishing marks on the substrate prior to sputtering. The white hillocks are the outgrown preferential deposited areas and the dark holes are the voids caused by the removal of some of them. Fig.6.27 shows a cross section of the sputtered layer with voids due to the lifting off of the preferential deposited areas. Thus it can be seen that the growth instabilities, which occur during deposition have significant effects on the sputtered layer.

On closer examination, the cross section of the sputtered layer shown in fig.6.22 reveals faint lines parallel to the substrate surface. This effect is similar to that of a layer consisting of 2 or 3 different thin layers and was observed only in some sputtered layers. However, the amorphous nature of the layer was not affected by these defects. Since the process was not interrupted at an intermediate stage, the cause of this defect is not clear. It is probably due to a change in the rate of sputtering caused by an unobserved factor such as a difference in the gas pressure or other process parameter.

6.5.3. Electron Beam Surface Melting.

The sputtered layer was then heated by an electron beam, with the main objective of investigating whether the sputtered layer would retain its amorphous nature on subsequent rapid cooling. Since the

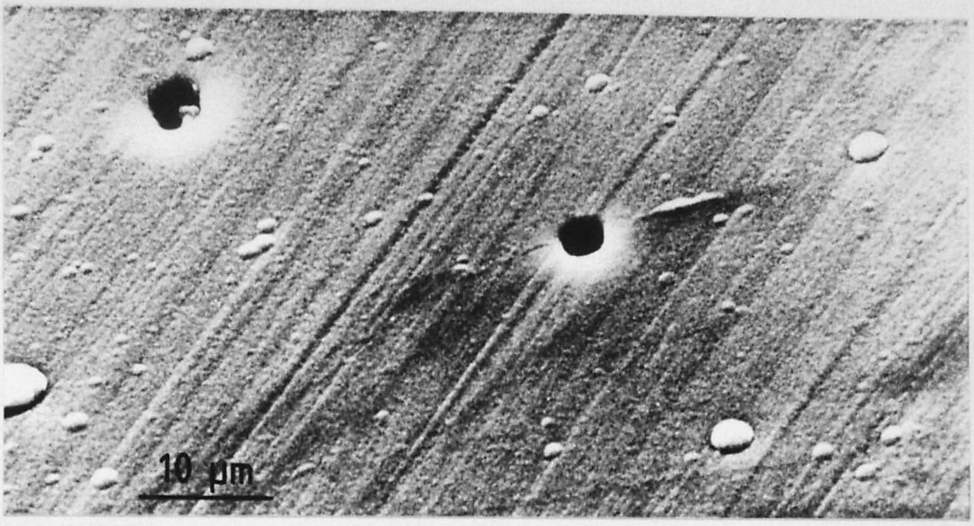

Fig. 6.26. The surface of the sputtered $Fe_{80}P_{13}C_7$ layer (SEM)

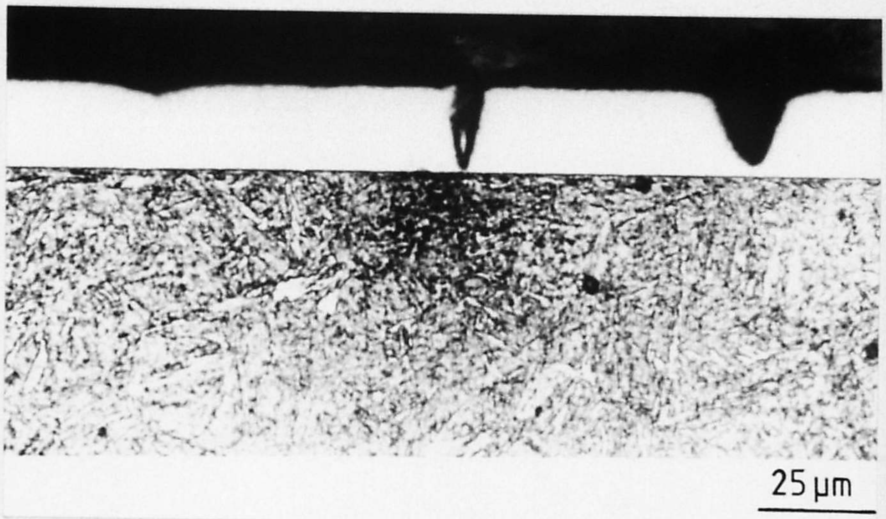

Fig. 6.27. A cross section of the sputtered $Fe_{80}P_{13}C_7$ layer with voids caused by the lifting off of the preferential deposited areas (Optical micrograph)

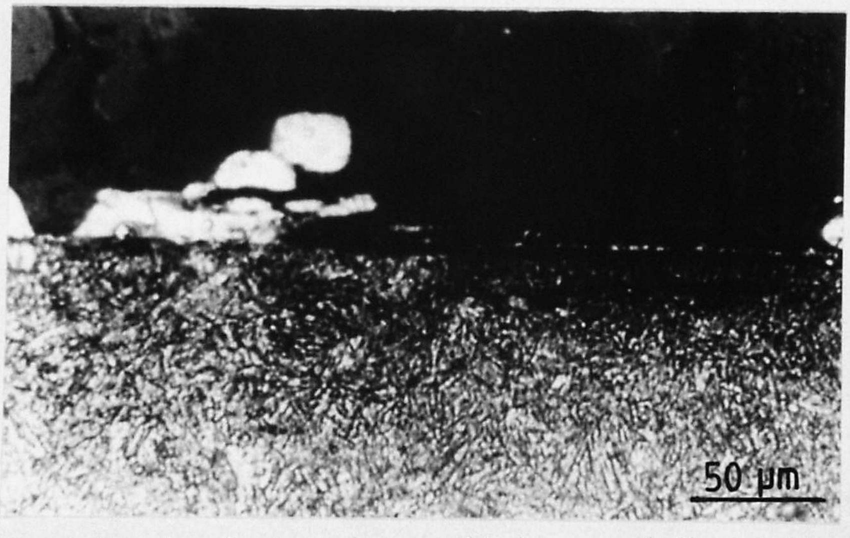

Fig.6.28. An electron beam melted area of the sputtered layer.

thickness of the layers was only ∿10-17μm, very low power beams and high traverse speeds were used in order to melt only the layer (to avoid dilution). This aim was achieved by the use of a beam power of 40W with a traverse speed of 34.2 cm s^{-1}. Although these conditions were good enough to melt only the layer, it was observed that the electron beam has shattered and removed the sputtered layer from the substrate surface. Fig.6.28 shows an electron beam surface melted area of the sputtered layer. This shattering and removal of the layer can probably be an effect of the bombardment of electrons on the thin layer but it also raised doubts about the adhesion of the layer to the substrate. Tests carried out to investigate adhesion and wear resistance properties of sputtered $Fe_{80}P_{13}C_7$ amorphous will be discussed in the next section.

6.6. Assessment of Gas Erosion Wear Resistance of the Surface Layers.

For the investigation of gas erosion wear resistance of surface layers on steel, the following samples were subjected to thermal gas erosion experiment decribed in section 3.10.

Sample 1. - One of the split vent samples was sputtered using a $Fe_{80}P_{13}C_7$ alloy target (fig.6.29). Sputtering was carried out with an average voltage of 580V and an average current of 60mA for 53 hours. Since it was not practical to remove the layer for examination, $Fe_{80}P_{13}C_7$ layers were also sputtered on a piece of NaCl and a sample of high-strength steel (∿ 5x15mm) simultaneously with the split vent sample.

The layer sputtered on NaCl was removed by dissolving NaCl in water and its amorphous nature was confirmed by electron microscopy. The thickness of the layer on the small steel sample was ∿15μm (fig.6.30) and it was assumed that the layer on the split vent sample had the same thickness. The cross section shown in fig.6.30 also showed the

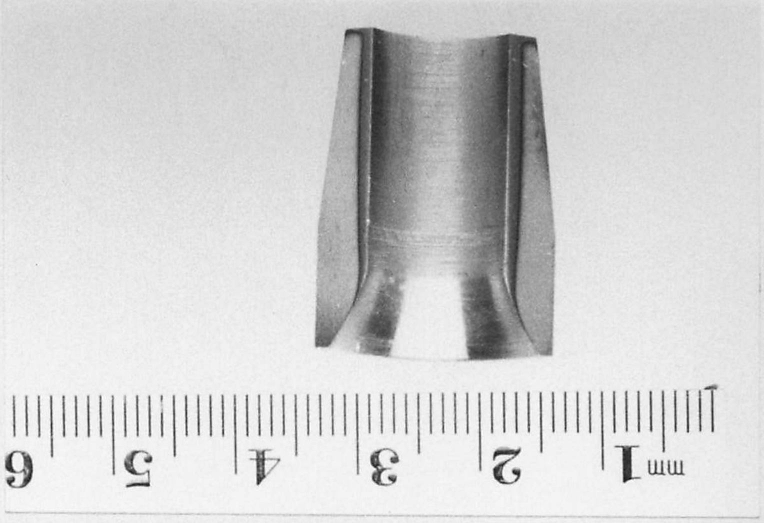

Fig. 6.29. The top view of the split vent sample, sputtered with $Fe_{80}P_{13}C_7$ alloy.

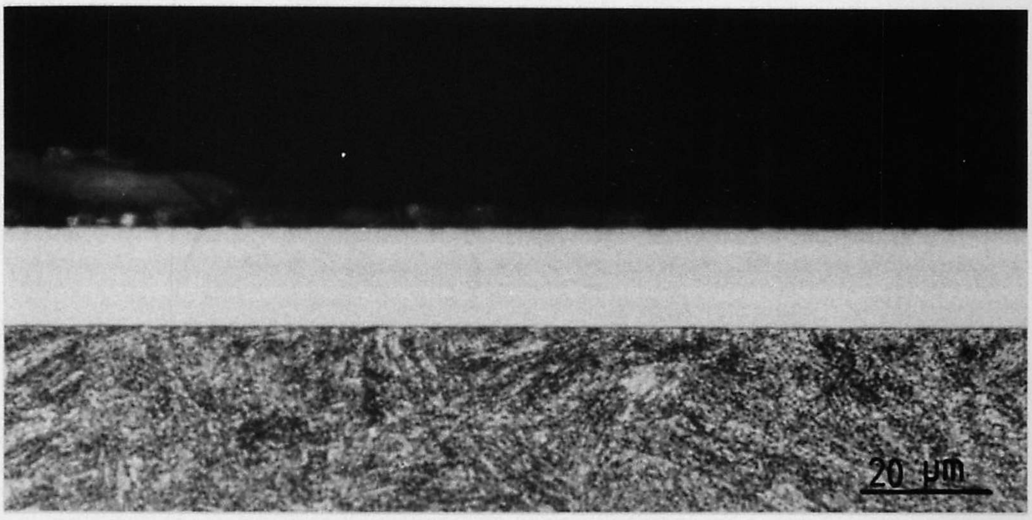

Fig. 6.30. $Fe_{80}P_{13}C_7$ layer which was sputtered on a steel substrate, simultaneously with the split vent sample. (Optical micrograph)

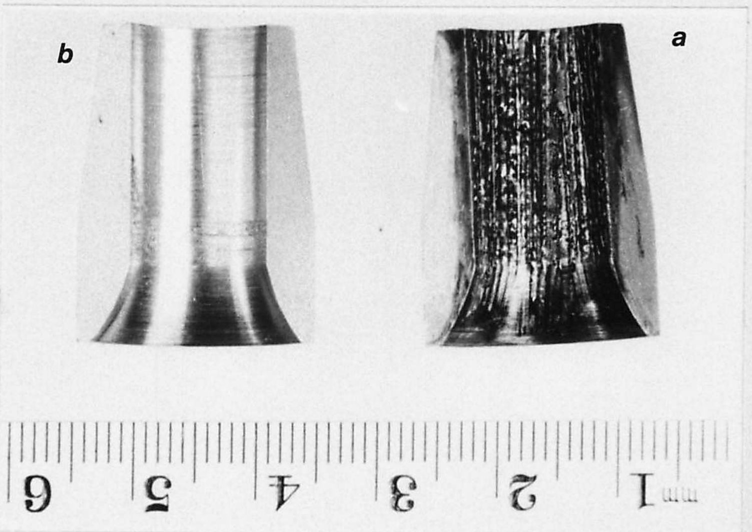

Fig. 6.31. The top views of the split vent samples.
(a) with the electron beam clad $Fe_{80}P_{13}C_7$ layer.
(b) untreated, control sample

faint lines on the layer. EDX analysis of this layer (not analysing carbon but normalizing other elements to 100%wt.) indicated 7.52%wt. (∿12%at.) phosphorous and ∿1%wt. of Ti, Mn and other trace elements while the balance was iron.

Sample 2. - The $Fe_{80}P_{13}C_7$ powder layer was applied on the second split vent sample using Collodion solution as the binder. Due to the curved nature of the specimen, it was not possible to apply a coating with an accurate thickness. The layer was approximately 0.3 - 0.5mm thick. When the layer was dry, a 100W electron beam with a traverse speed of 4.4 cm s^{-1} was used to clad it onto the substrate surface. A channelled but apparently well adhered layer was obtained by this method. However it was not possible to cut and mount the specimen prior to erosion experiment. Therefore the nature of the clad coating was not determined. Fig. 6.31a shows the top view of the specimen.

Reliable EPMA results are obtainable only on the flat polished samples but an attempt was made at RARDE to analyse the P, and Fe content of the coating. The average phosphorous content was found to be ∿9.4%wt. (∿ 14.8 at%). However the accuracy of the results of this analysis is questionable.

Sample 3. - Third split vent sample was untreated and was used as the control specimen. Top view of the specimen is shown in fig. 6.31b.

The surface layers of split vent samples were investigated after subjecting them to the erosion wear test. The mass loss of each sample during the experiment was as follows.

Sample	mass loss (g)
1. With sputtered layer	0.1158
2. With clad layer	0.1250
3. Control specimen	0.0585

Sample 1

In most areas, the coating had come off the substrate and where it remained, the thickness had been reduced to 4µm (from 15µm). Figures 6.32a and b show some of the remaining coating. The structure of the remaining layer indicated that it had become crystalline. The adherence of the sputtered layer to the substrate was probably not good enough to withstand the gas erosion. Although no porosity was observed, it was possible that some gases remained in very small pores in the layer. The expulsion of these gases may also have enhanced the removal of the layer. Some of the remaining layer consisted of partly separated two or three thin layers (fig. 6.32b). This is purely a weakness caused by the slightly discontinuous nature of the sputtered layer prior to the erosion test (as shown in fig. 6.30).

It may well be that metallographic preparation of these specimens enhanced the removal of already loosened parts of the layer. The observation of loose parts of the layer in mounted specimens (fig. 6.33) demonstrates this effect.

Sample 2.

The electron beam clad $Fe_{80}P_{13}C_7$ alloy powder layer on the second split vent sample had been almost completely removed during the erosion wear test. It is however, difficult to assess the quality of the coating, since it was not known how well the layer was clad on to the surface prior to the erosion experiment.

EPMA analysis carried out at RARDE showed a depletion of phosphorous in both sample 1 and sample 2. After the erosion wear test the amount of phosphorous left seemed to be very low and varied from 0.5 - 1.3%wt. EDX analysis was also carried out on the remains of sputtered coatings. Results indicated that the amount of phosphorous left was about 1%wt.

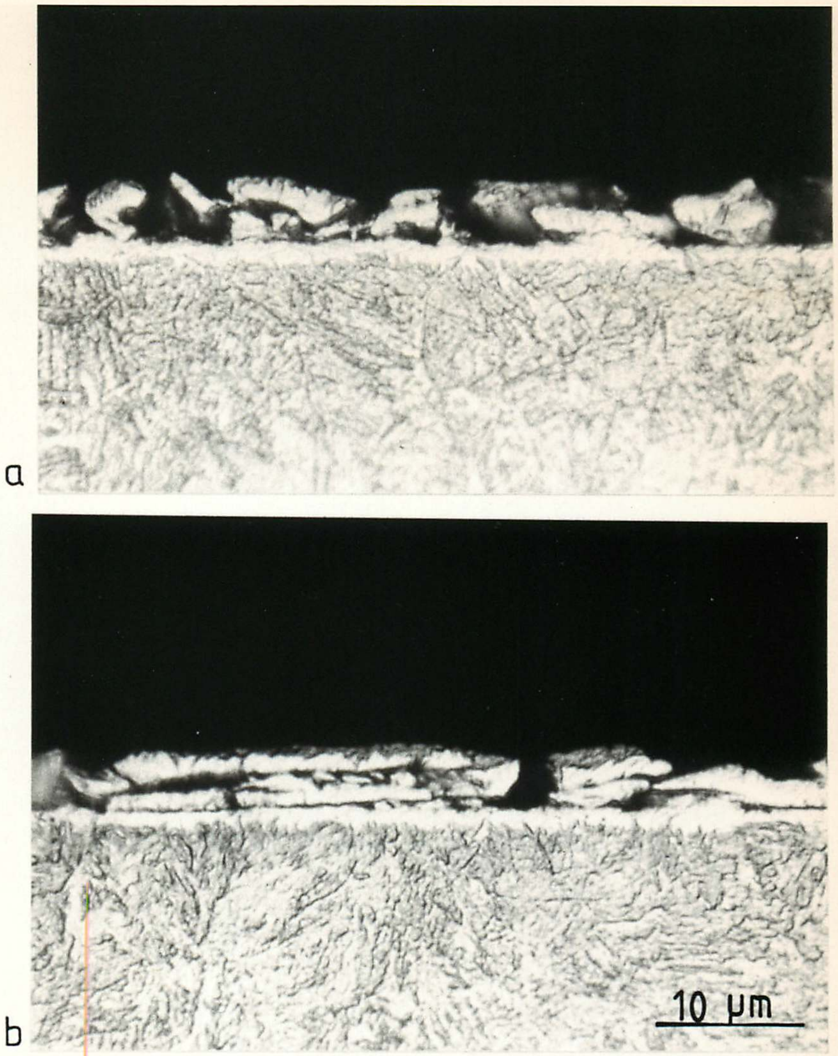

Fig. 6.32a. and 6.32 b.
The remains of the sputtered coatings after gas erosion wear test. (optical micrograph)

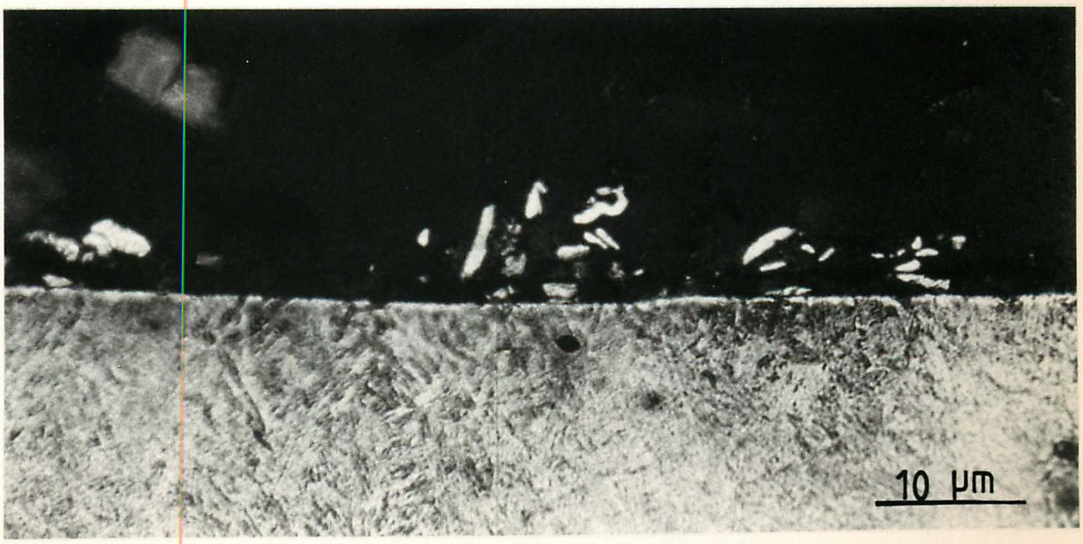

Fig. 6.33. The loose parts of the sputtered layer (after the gas erosion wear test), observed in a mounted specimen (Optical micrograph)

From these results, it is clear that there had been a considerable loss of phosphorous during the erosion wear experiment. Since phosphorous was expected to be in a stable form in the layer, such a significant loss was not expected. The temperature increase of the surface layer, may have caused phosphorous to evaporate or probably the gses such as oxygen and carbon dioxide may have reacted with phosphorous to produce oxides of phosphorous.

This depletion of phosphorous concentration changes, the glass forming compositions of the Fe-P-C system, resulting in a crystalline alloy. These results show that the phosphorous depletion and the removal of the coatings, are two great disadvantages in retaining the amorphous Fe-P-C layers on steels, subjected to erosion wear environments of hot gases.

Due to the high cost involved in each firing experiment, it was decided to use 2 x 2 cm flat samples simultaneously with the curved split vent samples. Since the flat samples could not be fixed in the cylindrical bomb chamber of the testing equipment, they were kept in the firing chamber. The following specimens were prepared and were subjected to erosion tests.

1. Plasma sprayed Fe-P-C layer on a steel substrate.
2. Similar to specimen 1, but after electron beam surface treatment.

Fig. 6.34a and b are scanning electron micrographs of the surface of specimen 1, before and after the wear test respectively and figures 6.35a and b are those of specimen 2. Since the propellant occupied some 25% of the chamber volume, samples were buried in the propellant during firing. The specimen surfaces contained some combustion debri. Some of the debri were adhered so strongly to the specimen surface, that attempts to clean the surfaces even by ultrasonic methods were

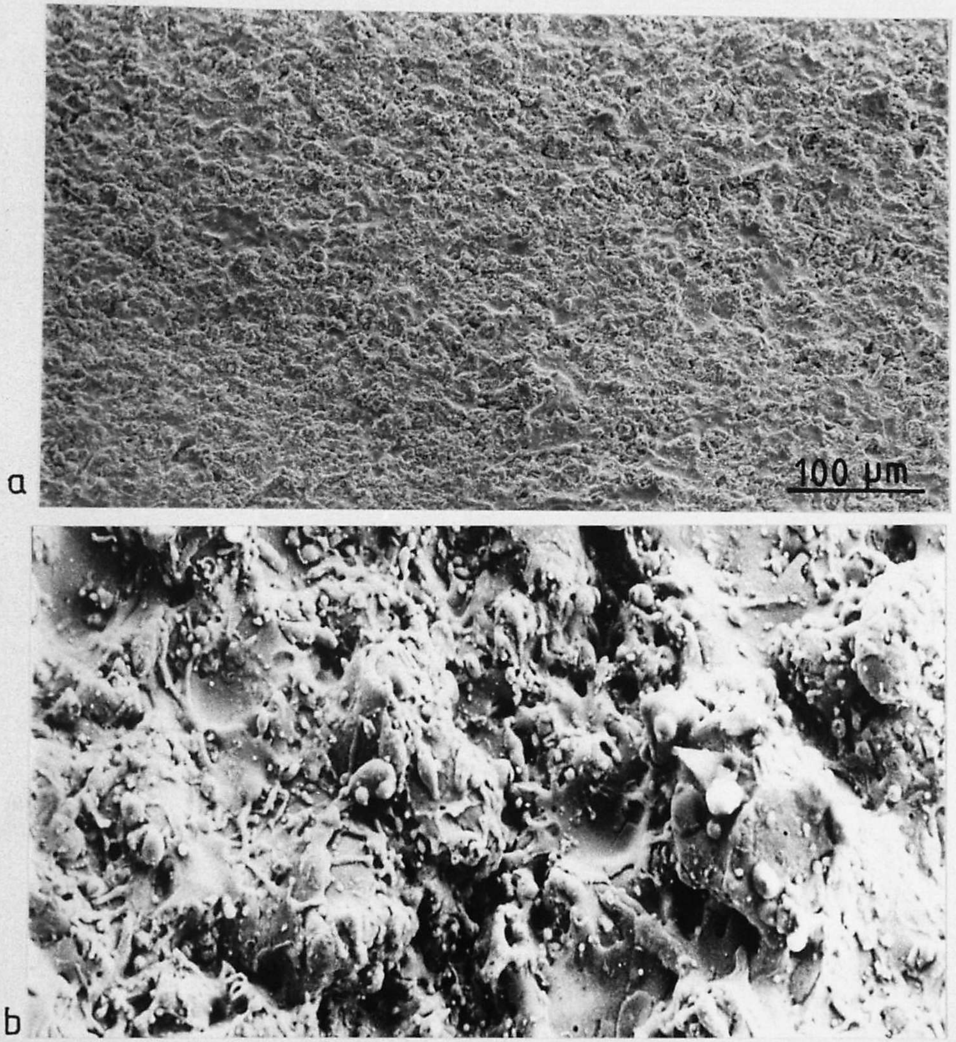

Fig. 6.34
(a) The surface of the Fe-P-C plasma sprayed layer (SEM)
(b) The same surface after the gas erosion wear test (SEM)

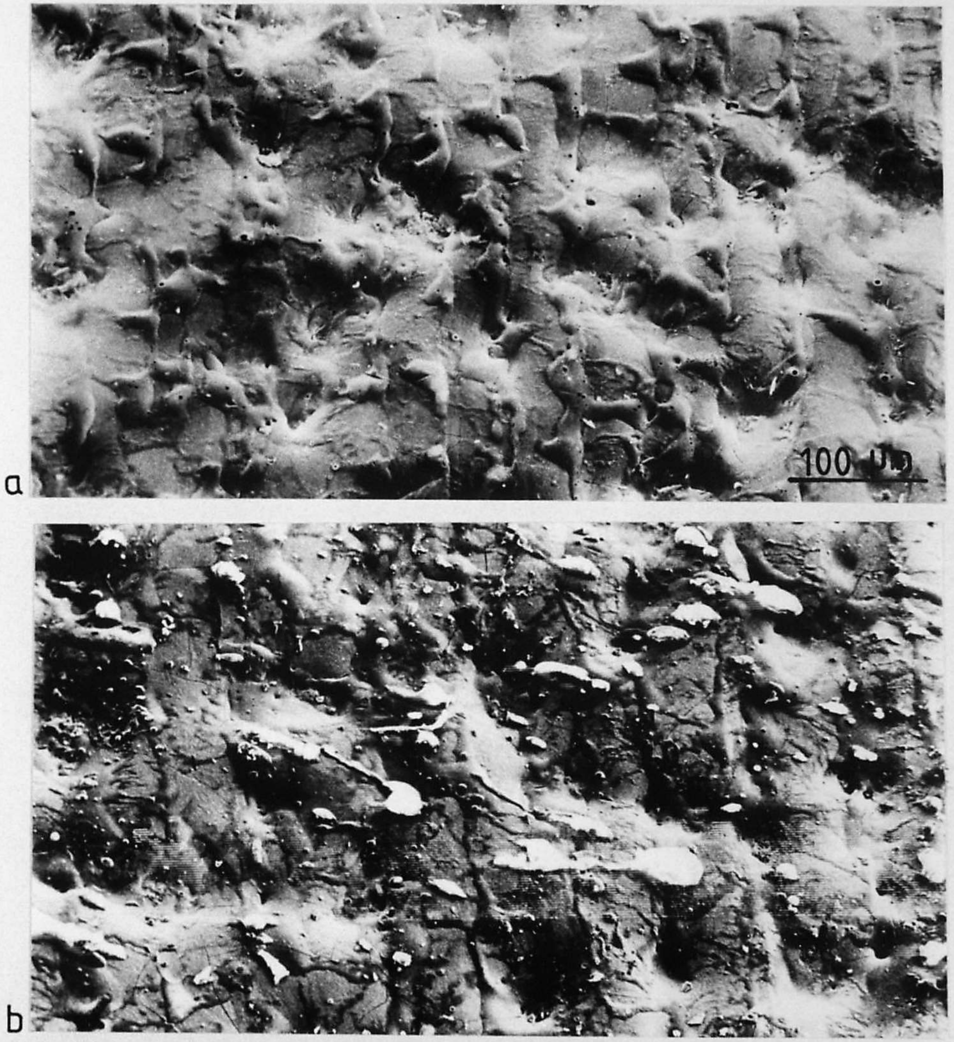

Fig. 6.35.
(a) The same surface shown in fig.6.34a, but after electron beam rapid quenching. (SEM)
(b) The same surface shown in fig.6.35a after the gas erosion wear test. (SEM)

unsuccessful. White particles in fig. 6.34 and 6.35b show the debri present on the surfaces. EDX analysis showed that particles did not contain iron but they were rich in calcium, potassium and silicon. Thus accurate results could not be obtained by the examination of these surfaces and further detailed investigations were not performed.

The plasma sprayed layer showed a certain amount of surface degradation, (fig. 6.34b) after the gas erosion. Some of the protrusions at the surface, due to open pores had been removed. The plasma sprayed and electron beam rapidly quenched layer showed lesser degradation (fig. 6.35b). The consolidation of the plasma sprayed layer by rapid surface quenching reduce the amount of protrusions by sealing off most of the pores, resulting in lesser surface degradation, than that of ordinary plasma sprayed layers.

6.7. Conclusions

1. When the process parameters were optimised, the application of $Fe_{80}P_{13}C_7$ alloy powder, with the use of a binder, on steel substrates followed by electron beam rapid quenching, yielded metallic glass layers on the surface. Due to surface tension effects of the liquid metal, the rapidly quenched layers were approximately semi-cylindrical in shape.
2. These metallic glass layers retained a glassy nature even when they were subjected to electron beam rapid quenching again.
3. With an optimum beam power and traverse speed, it was possible to produce metallic glass layers at steel surfaces, with dilution occurring only at an extremely thin area at the interface.

4. The electron beam rapid quenching of plasma sprayed $Fe_{80}P_{13}C_7$ alloy layers did not yield a metallic glass, mainly because of the poor heat transfer properties due to the large amount of porosity present in the layer. Plasma spraying in vacuum or in a controlled atmosphere may lead to layers with better qualities. Further investigations in this field are necessary.

6. Thin films of amorphous $Fe_{80}P_{13}C_7$ alloy were prepared by a direct current sputtering process. The sputtered layers were apparently well adhered to the substrate but some growth instabilities, caused by impurities were present.

7. Erosion wear experiments on powder clad layer and sputtered layer caused a removal of these layers off the substrate. There was also a reduction in phosphorous concentration. Further investigations have to be carried out to find out means of improving the adherence of these layers to the substrate and to modify the composition to make them more stable at high temperatures.

8. Erosion tests on a $Fe_{80}P_{13}C_7$ plasma sprayed layer and on an identical layer, which in addition was subjected to electron beam rapid quenching showed that the surface degradation of the latter was comparatively low, due to the consolidation of the original layer.

CHAPTER 7.

7. Conclusions and Suggestions for Further Work

This chapter outlines the main overall conclusions. Suggestions are also made for further interesting work that should significantly contribute in this area of research.

Theoretical heat flow analysis was carried out to obtain a better understanding of electron beam quenching process, and to optimise the processing conditions. Rosenthal's theory of three dimensional heat flow in materials subjected to a moving point heat source, originally developed for use in the field of welding was suitable for the present study. It was demonstrated that this theory could be successfully applied to electron beam rapid quenching of surfaces, over the range of process parameters used in the present experiments. Theoretical results indicated that at a constant beam power input and a traverse speed, cooling rate decreased with increasing depth below the surface. For the same traverse speed, the cooling rate at a point in the melted region, increased as the power input decreased.

As predicted theoretically, when low power beams were used, the effects of higher cooling rates were experimentally observed in regions near the surface. Higher quenching rates led to the formation of metallic glass at the surfaces of alloys of glass forming compositions. Rosenthal's theory is based on assumptions such as constant thermal characteristics of the materials and the neglect of latent heat of melting. Further work could be usefully carried out to examine the significance of these assumptions by extending the theory to include those parameters.

Rapid quenching of ultra high-strength steel led to a considerable grain refinement in the rapidly quenched structure. Since grain refinement is an important strengthening mechanism in the heat treatment of metals, this effect would yield better mechanical properties in the steel. Rapid quenching also increased the solid solubility of alloying elements. The stabilization of austenite due to the prevention of the growth of martensite by closely spaced boundaries led to this increase in retained austenite. The retention of alloying elements in the solid solution was another reason for the increase in retained austenite. The amount of twinning in martensites, also increased by rapid quenching since twinning was the preferred mode of transformation at lowered M_s temperatures as a result of the high cooling rate.

The mainly martensitic structure, the grain refinement and the increased solid solubility led to a large increase in microhardness of the rapidly quenched regions, compared with that of conventionally solid state quenched steel of the same composition. Melt spun ultra high-strength steel was also found to have a similar microstructure and a microhardness to the electron beam rapidly quenched material, showing that whatever the method used, the effects of high cooling rates were similar.

Surface morphology studies revealed that surface tension gradients, counteracted by the force of gravity, led to the formation of surface ripples on rapid solidification. Surface roughness was reduced by an increase in traverse speed. The surface ripples can probably be completely avoided by the use of higher traverse speeds. Large surface areas can be rapidly quenched by the use of overlapping passes. The microhardness of rapidly quenched areas was not greatly reduced by heat effects from neighbouring passes, but the mechanical properties could well have been improved due to stress relaxation effects.

One of the main aims of the project; the study of electron beam induced formation of metallic glass layers at the surface of an alloy (with a glass forming composition), was accomplished using a $Fe_{80}P_{13}C_7$ alloy. Although experiments were carried out mainly on

$Fe_{80}P_{13}C_7$ alloy it was shown that metallic glass layers could be made at the surfaces of other alloys as well.

Amorphous layers of $Fe_{80}P_{13}C_7$ alloy were clad to the steel substrates successfully by the application of the alloy powder followed by electron beam rapid quenching. The dilution of the alloy with the substrate at the interface can be restricted to only a very thin region by the control of process parameters. This shows that the electron beam rapid quenching process can be successfully used to apply coatings with different surface properties or a structure to the surfaces of other substrates without changing or sacrificing the bulk characteristics of the substrates.

Although the clad layer had a semi-circular morphology due to the surface tension effects in the liquid state, this problem could probably be avoided by rapid oscillation of the beam in one direction, while moving the specimen in a perpendicular direction. These movements would result in rapidly quenching a wider surface simultaneously, thus avoiding the semi-circular bead shape of the re-solidified region. Further improvements to the electron beam quenching apparatus are necessary to achieve this aim. Further work should also be carried out on the feasibility of obtaining large surface areas of metallic glass. Simultaneous oscillation and the movement of the beam in two orthogonal directions probably would avoid the crystallisation of metallic glass caused by the heat effects of neighbouring passes.

Plasma spraying is a good process to obtain flat, uniform coatings but further investigations should be carried out in vacuum or controlled atmospheres in order to obtain pore free layers. Further rapid quenching experiments are also required to investigate the feasibility of producing amorphous layers by electron beam quenching pore free plasma sprayed layers. However, the amount of surface degradation which occurs in plasma sprayed Fe-P-C layers, when subjected to erosion wear tests was reduced by the consolidation of those layers using electron beams.

Sputtering seems to be the best coating method used in this work to produce uniform amorphous layers on different substrates but it would be desirable to improve the adherence of sputtered layers to the substrate. The variables such as gas pressure and substrate temperature, on which the quality of the sputtered layer depends should be systematically examined.

It is clear that metallic glass layers of other alloys can be formed on ultra high-strength steel substrates by an electron beam rapid quenching process, and by sputtering. Electron beam rapid quenching is a good method to clad metallic glass layers on other crystalline substrates, without excessive dilution occurring at the interface. Therefore this coating process can advantageously be used in applications where a change of composition or property of the substrate is not expected.
It would be of interest to prepare a range of different metallic glass layers by electron beam rapid quenching and sputtering and carry out erosion wear tests to investigate which would be the most durable in retaining the amorphous nature and wear resistance.

APPENDIX 1

HEAT 1

```
C     COMPUTES AND PLOTS TEMP VS TIME
C     COMPUTES AND PLOTS APPROXIMATE QUENCH RATE VS TIME
C     COMPUTES 4 DEPTHS .PLOTS 3 DEPTHS.
      WRITE(6,20)
      WRITE(6,11)
      WRITE(6,7)
      WRITE(6,11)
C     VERSION 5
C     T=TEMPERATURE
C     X,Y,Z,P=CO-ORDINATES
C     R=FUNCTION OF CO-ORDINATES
C     M=DENSITY, KG/CUBIC METER
C     Q=HEAT INPUT, JOULES/SECOND
C     S=TIME, SECONDS
C     C=SPECIFIC HEAT, JOULES/KG/K
C     V=BEAM VELOCITY, METERS PER SECOND
C     K=HEAT CONDUCTIVITY, JOULES/SECOND/METER/DEGREE
      REAL M,F,X,Y,Z,P,R,K,V,C,T,S,TEST1,TEST2,Q,SEC(100),
     1TEMP(100,4),ZED(4)
      INTEGER S1,C98,C97
C     *****************************************************
      V=0.044
      K=42.0
      Q=300.0
      C=691.0
      Y=0
      X=0.005
      M=7874.0
C     *****************************************************
30    FORMAT(23H CO-ORDINATES X Y      ,E10.2,E10.2)
      WRITE(6,15) V
      WRITE(6,12) K
12    FORMAT(19H HEAT CONDUCTIVITY=,F8.2,8H J/S/M/K)
15    FORMAT(15H BEAM VELOCITY=,F8.4,19H  METRES PER SECOND)
      WRITE(6,13) M
13    FORMAT(9H DENSITY=,F8.0,16H  KG/CUBIC METRE)
      WRITE(6,11)
      WRITE(6,20)
      WRITE(6,11)
```

```
        ZED(4)=0.0005
        ZED(3)=0.0004
        ZED(2)=0.0002002
        ZED(1)=0.0002
        WRITE(6,16) Q
   16   FORMAT(12H HEAT INPUT=,F6.1,15H  JOULES/SECOND)
        WRITE(6,30)X,Y
        WRITE(6,18)
        DO 6 C98=1,4
        Z=ZED(C98)
   18   FORMAT(10H    TIME/S,7H  TEMP )
        F=0.5*C*M/K
        DO 4 S1=1,60,1
        S=S1
        S=S/100.0
        SEC(S1)=S
        P=X-V*S
        R=SQRT(P*P+Y*Y+Z*Z)
        TEST1=ABS(F*V*P)
        TEST2=ABS(F*V*R)
        IF (TEST1 .GT. 170) GOTO 4
        IF (TEST2 .GT. 170) GOTO 4
        T=((EXP(-F*V*P))*(EXP(-F*V*R))/R)*(Q/(12.57*K))+25
        TEMP(S1,C98)=T
    4   CONTINUE
    6   CONTINUE
        WRITE(6,11)
   11   FORMAT(1H )
    7   FORMAT (38H HEAT FLOW PROGRAM VERSION 5 20-9-1982)
   20   FORMAT(50H ********* ********* ********* ********* *********)
        DIMENSION X1(60),X2(60),X3(60),X4(60),Y1(60),Y2(60)
       1,Y3(60),Y4(60),Y5(60),X5(60),Y6(60),Y7(60),Y8(60)
        DO 40 C97=1,50
        X1(C97)=SEC(C97)
        X2(C97)=SEC(C97)
        X3(C97)=SEC(C97)
        X4(C97)=SEC(C97)
        Y1(C97)=TEMP(C97,1)
        Y2(C97)=TEMP(C97,2)
        Y3(C97)=TEMP(C97,3)
        Y4(C97)=TEMP(C97,4)
        IF (C97 .EQ. 1) GOTO 505
        X5(C97)=SEC(C97)
```

```
      Y5(C97)=(Y1(C97)-Y1(C97-1))/(SEC(C97)-SEC(C97-1))
      Y6(C97)=(Y2(C97)-Y2(C97-1))/(SEC(C97)-SEC(C97-1))
      Y7(C97)=(Y3(C97)-Y3(C97-1))/(SEC(C97)-SEC(C97-1))
      Y8(C97)=(Y4(C97)-Y4(C97-1))/(SEC(C97)-SEC(C97-1))
      GOTO 506
505   X5(C97)=0.0
      Y6(C97)=0.0
      Y7(C97)=0.0
      Y8(C97)=0.0
      Y5(C97)=0.0
506   WRITE(6,5555)SEC(C97),Y1(C97),Y2(C97),Y3(C97),Y4(C97)
     &,Y5(C97),Y6(C97),Y7(C97),Y8(C97)
5555  FORMAT(1H ,F8.3,4F9.0,4E12.4)
40    CONTINUE
      CALL GRLM2S(40.,200.,40.,200.)
      CALL GRLM3S(0.0,0.50,0.0,3000.0)
      CALL GRFT3S(3.0,0.0,0,0,0.1,6)
      CALL GRTY5S(1,'*')
      CALL GRGR6S(X1,Y1,50)
      CALL GRPN4S(2)
      CALL GRTY5S(1,220)
      CALL GRGR6S(X2,Y2,50)
      CALL GRPN4S(3)
      CALL GRTY5S(1,203)
      CALL GRGR6S(X3,Y3,50)
      CALL GRAN6S('HEAT FLOW ANALYSIS',18,'TIME / SECONDS',14,
     1'TEMPERATURE / CENTIGRADE',24)
      CALL GRMS5S(500.0)
      CALL GRLM2S(60.,220.,40.,200.)
      CALL GRLM3S(0.0,0.50,-120000.0,140000.0)
      CALL GRFT3S(3.0,0.0,0,0,0.1,6)
      CALL GRTY5S(1,220)
      CALL GRGR6S(X5,Y5,50)
      CALL GRTY5S(1,'*')
      CALL GRPN4S(2)
      CALL GRGR6S(X5,Y6,50)
      CALL GRPN4S(3)
      CALL GRTY5S(1,203)
      CALL GRGR6S(X5,Y7,50)
      CALL GRAN6S('GRADIENT ANALYSIS',17,'TIME / SECONDS',14,
     &'DT/DT  /  CENTIGRADE PER SEC',28)
      STOP
      END
```

HEAT 2

```
C  CALCULATION OF QUENCH RATE AT THE MELT DEPTH,ZED SET AT THE
C  VALUE OF THE MELT DEPTH, SEC AT A TIME THAT IS ON THE COOLING
C  PART OF THE HEAT CYCLE, BUT NEAR TH TEMPERATURE(J1) AT WHICH
C  THE QUENCH RATE TO BE DETERMINED. ALSO SET THE HEAT INPUT 'Q1'
C  AT THE CORRECT VALUE. 07.04.1981.
      WRITE(6,20)
      WRITE(6,11)
      WRITE(6,7)
      WRITE(6,11)
C  T=TEMPERATURE
C  X,Y,Z,P=CO-ORDINATES
C  R=FUNCTION OF CO-ORDINATES
C  M=DENSITY, KG/CUBIC METER
C  Q= HEAT INPUT, JOULES/SEC
C  S=TIME, SEC
C  C= SPECIFIC HEAT, JOULES /KG/K
C  V=BEAM VELOCITY , M /SEC
C  K= HEAT CONDUCTIVITY, JOULES/SEC/METER/DEG
      DOUBLE PRECISION M,F,X,Y,Z,P,R,K,V,C,T,S,ALPHA,BETA,Q,
     1ZED(8),J1,SEC(10,8),TEMP(10,8),HEAT(10),QUENCH(10,8)
      INTEGER S1,Q1,C98,C97
C  *******************************************************
      V=0.044
      K=42.0
      C=691.0
      Y=0
      X=0.005
      M=7874.0
C  *******************************************************
C  SET THE VALUE OF J1 TO THE TEMP AT WHICH QUENCH RATE IS DETERMINED
      J1=1390.0D+00
      WRITE(6,15) V
      WRITE(6,12) K
 12   FORMAT(19H HEAT CONDUCTIVITY=,F8.2,8H J/S/M/K)
 15   FORMAT(15H BEAM VELOCITY=,F8.4,19H  METERS PER SECOND)
      WRITE(6,13) M
      WRITE(6,999) X,Y
```

```
999   FORMAT(20H X & Y CO-ORDINATES=,2F10.4)
13    FORMAT(9H DENSITY=,F8.0,16H  KG/CUBIC METER)
      WRITE(6,11)
      WRITE(6,20)
      WRITE(6,11)
      ZED(1)=0.0004D+00
      Q1=300
      SEC(1,1)=0.120D+00
931   S=SEC(1,1)
      IF (S .EQ. 0.0D+00)  GOTO 905
      Z=ZED(1)
      Q=Q1
      F=0.5*C*M/K
      P=X-V*S
      R=DSQRT(P*P+Y*Y+Z*Z)
      ALPHA=DEXP(-F*V*P)
      BETA=((DEXP(-F*V*R))/R)
      QUENCH(1,1)=(Q/(12.57*K))*ALPHA*BETA*((P*V/(R**2))+F*P*V*V/R
     &+V*V*F)
      TEMP(1,1)=ALPHA*BETA*(Q/(12.57*K)) +25.0D+00
      IF (DABS(TEMP(1,1)-J1) .GT. 0.1D+00) GOTO 930
      GOTO 902
930   SEC(1,1)=S-(TEMP(1,1)-J1)/QUENCH(1,1)
      GOTO 931
905   QUENCH(1,1)=0.0D+00
902   WRITE(6,903) ZED(1),Q,SEC(1,1),TEMP(1,1),QUENCH(1,1)
903   FORMAT(5D12.4)
      WRITE(6,20)
11    FORMAT(1H )
7     FORMAT (40H HEAT FLOW PROGRAM VERSION 301 07-4-1981)
20    FORMAT(50H-*********_*********_*********_*********_*********,
     &10H-*********)
      STOP
      END
```

HEAT 3

```
C  CALCULATION OF QUENCH RATE AT THE MELT WIDTH,WHY SET AT THE
C  VALUE OF THE MELT WIDTH, SEC AT A TIME THAT IS ON THE COOLING
C  PART OF THE HEAT CYCLE, BUT NEAR THE TEMPERATURE(J1) AT WHICH
C  THE QUENCH RATE TO BE DETERMINED. ALSO SET THE HEAT INPUT 'Q1'
C  AT THE CORRECT VALUE. 11.06.1981.
      WRITE(6,20)
      WRITE(6,11)
      WRITE(6,7)
      WRITE(6,11)
C  T=TEMPERATURE
C  X,Y,Z,P=CO-ORDINATES
C  R=FUNCTION OF CO-ORDINATES
C  M=DENSITY, KG/CUBIC METER
C  Q= HEAT INPUT, JOULES/SEC
C  S=TIME, SEC
C  C= SPECIFIC HEAT, JOULES /KG/K
C  V=BEAM VELOCITY , M /SEC
C  K= HEAT CONDUCTIVITY, JOULES/SEC/METER/DEG
      DOUBLE PRECISION M,F,X,Y,Z,P,R,K,V,C,T,S,ALPHA,BETA,Q,
     1WHY(8),J1,SEC(10,8),TEMP(10,8),HEAT(10),QUENCH(10,8)
      INTEGER S1,Q1,C98,C97
C  ***************************************************************
      V=0.0436
      K=42.0
      C=691.0
      Z=0
      X=0.002
      M=7874.0
C  ***************************************************************
C  SET THE VALUE OF J1 TO THE TEMP AT WHICH QUENCH RATE IS DETERMINED
      J1=1390.0D+00
      WRITE(6,15) V
      WRITE(6,12) K
12    FORMAT(19H HEAT CONDUCTIVITY=,F8.2,8H J/S/M/K)
15    FORMAT(15H BEAM VELOCITY=,F8.4,19H  METERS PER SECOND)
      WRITE(6,13) M
      WRITE(6,999) X,Z
999   FORMAT(20H X & Z CO-ORDINATES=,2F10.4)
```

```
 13    FORMAT(9H DENSITY=,F8.0,16H  KG/CUBIC METER)
       WRITE(6,11)
       WRITE(6,20)
       WRITE(6,11)
       WHY(1)=0.0004D+00
       Q1=300
       SEC(1,1)=0.12D+00
 931   S=SEC(1,1)
       IF (S .EQ. 0.0D+00)  GOTO 905
       Y=WHY(1)
       Q=Q1
       F=0.5*C*M/K
       P=X-V*S
       R=DSQRT(P*P+Y*Y+Z*Z)
       ALPHA=DEXP(-F*V*P)
       BETA=((DEXP(-F*V*R))/R)
       QUENCH(1,1)=(Q/(12.57*K))*ALPHA*BETA*((P*V/(R**2))+F*P*V*V/R
      &+V*V*F)
       TEMP(1,1)=ALPHA*BETA*(Q/(12.57*K)) +25.0D+00
       IF (DABS(TEMP(1,1)-J1) .GT. 0.1D+00) GOTO 930
       GOTO 902
 930   SEC(1,1)=S-(TEMP(1,1)-J1)/QUENCH(1,1)
       GOTO 931
 905   QUENCH(1,1)=0.0D+00
 902   WRITE(6,903) WHY(1),Q,SEC(1,1),TEMP(1,1),QUENCH(1,1)
 903   FORMAT(5D12.4)
       WRITE(6,20)
 11    FORMAT(1H )
 7     FORMAT (39H HEAT FLOW PROGRAM VERSION 12 11-6-1981)
 20    FORMAT(50H-*********_*********_*********_*********_*********,
      &10H-*********)
       STOP
       END
```

APPENDIX 2

Electron Probe Micro Analysis

Electron probe micro analysis of iron, phosphorous and carbon was carried out at RARDE, Fort Halstead, to determine the composition and the homogeneity of alloy coatings.

Quantitative analysis for this particular combination was difficult without close comparison standards. However the following methods were used.

a) Iron and phosphorous were analysed using standards of pure Fe and GaP. The computer correction program (ZAF correction) was run to give carbon by difference. This method gave reasonable figures for iron and phosphorous. The carbon content was affected by the variations of phosphorous and iron content and it also included the contents of any other elements present.

b) Carbon was analysed by the use of a standard calibration curve. In this method, a range of accurately known carbon compositions were measured and a curve was obtained for the variation of X-ray intensity with the carbon concentration. By measuring the X-ray intensity of the unknown specimen, the concentration of carbon was found from the standard curve. this is an approximate method and the accuracy of results are less certain.

References

Following abbreviations are used.

ALMP - Proceedings of the Conference on Applications of Lasers in Materials Processing, Washington DC 1979. Ed. E.A. Metzbower. (American Society for Metals, Metals Park, Ohio, 1979).

LSI & LP - Proceedings of the Conference on Laser-Solid Interactions and Laser Processing, Boston, USA, 1978. Ed. S.D. Ferris, H.J. Leamy and J.M. Poate (American Institute of Physics,1979)

RQM 2 - Proceedings of the 2nd International Conference on Rapidly Quenched Metals, Massachusetts, USA. 1975. Ed. N.J. Grant and B.C. Giessen (MIT Press 1976)

RQM 3 - Proceedings of the 3rd International Conference on Rapidly Quenched Metals. Brighton, England, 1978. Ed. B. Cantor (Metals Society, 1978)

RQM 4 - Proceedings of the 4th International Conference on Rapidly Quenched Metals, Sendai, Japan, 1981. Ed. T. Masumoto and K. Suzuki (Japan Institute of Metals, 1982).

RSP I - Proceedings of the International Conference on Rapid Solidification Processing; Principles and Technologies. Reston, Virginia, USA, 1977. Ed. R. Mehrabian, B.H. Kear and M. Cohen (Claitor's Publishing Division, Baton Rouge,1977)

RSP II - Proceedings of the International Conference on Rapid Solidification Processing: Principles and Technologies. Reston, Virginia, USA, 1980. Ed. R. Mehrabian, B.H. Kear and M. Cohen. (Claitor's Publishing Division, Baton Rouge,1980)

1. R.P. Allen, S.D. Dahlgren and M.D. Merz, 1976, RQM 2. Pg.37.

2. J.K.A. Amuzu, J. Phys (D). App. Phys. 13 (1980) L127

3. G.S. Ansell and E.M. Breinan, Trans. ASM 58 (1965) 110

4. T.R. Anthony and H.E. Cline, J. App. Phys. 48 (1977) 3888

5. T.R. Anthony and H.E. Cline, in 'Laser Applications in Materials Processing' 1979, Society of Photo Instrumentation Engineers, Vol. 198 Bellingham, WA, USA. Pg.82.

6. J.D. Ayers and R.J. Schaefer, 1979. Ibid. Pg.57.

7. J.D. Ayers, R.J. Schaefer and W.P. Robey, J. of Met. Aug,1981.Pg.19.

8. J.D. Ayers, T.R. Tucker and R.C. Bowers, Script. Met. 14 (1980) 549.

9. J.D. Ayers, T.R. Tucker and R.J. Schaefer, RSP II, 1980, Pg. 212.

10. T.I. Barry, R.K. Bayliss and L.A. Lay, J. Mat. Sci. 3 (1968) 229.

11. R.A. Baxter in 'Thermal Analysis', Ed. R.F. Schwenker and P.D. Garn, 1969 (Academic Press, NY 1969) Pg.65.

12. D. Beck, S.M. Copley, M. Bass and E. Van Stryland, RSP I, 1977. Pg.104.

13. R. Beker, G. Sepold and P.L. Ryder, Script. Met. 14(1980) 1283.

14. J.R. Bedell, US Patent No. 3, 862, 658 (1975)

15. J.V. Bee, P.R. Howell and R.W.K. Honeycombe Met. Trans. A, 10 (1979) 1213.

16. T. Bell in 'Surface Treatments for Protection', Inst. of Metals, 1978

17. H.W. Bergmann and B.L. Mordike. Proc. Conf. Metallic Glasses; Science and Technology, Budapest, 1980. Ed. C. Hargitai, I. Bakonyi and T. Kemeny.

18. H.W. Bergmann and B.L. Mordike, J. Mat. Sci. 16 (1981) 863

19. H.K.D.H. Bhadeshia and D.V. Edmonds, Proc. ICOMAT Conf. 1979, Massachusetts, USA. (MIT Press) Pg. 28.

20. H. Bornfield, Techniche Zentrablatt für Praktische Metalbearbeitung 43 (1933) 14

21. P.G. Boswell, J. Mat. Sci. 14 (1979) 1505

22. P.G. Boswell and G.A. Chadwick, Script. Met. 11 (1977) 459

23. E.M. Breinan and G.S. Ansell, Met. Trans 1(1970) 1513

24. E.M. Breinan and B.H. Kear, RSP I, 1977. Pg.87

25. E.M. Breinan, B.H. Kear, C.M. Banas and L.E. Greenwald in "Super Alloys; Metallurgy and Manufacture."Proc.3rd Int. Symp. Seven Springs, PA.1975, Pg. 436.

26. E.M. Breinan, B.H. Kear and C.M. Banas, Phys. Today, Nov. 1976, Pg. 44.

27. V.F. Brekhovskikh, A.A. Zhukov, A.N. Kokora and A.A. Uglov, Fiz. i Khimiya Obrabotki Materialov 4(1968) 35

28. W.J. Bryant, J. Electrochem. Soc. 125 (1978) 1534

29. R.W. Cahn, RSP I, 1977. Pg. 129.

30. B. Cantor and R.W. Cahn, RQM 3, 1978. Pg. 59.

31. H.S. Chen, Mat. Sci. Eng. 26 (1976) 79.

32. J.M. Chilton and P.M. Kelly, Acta Met. 16 (1968) 637.

33. C.P. Chou, L.A. Davies and M.C. Narasimhan, Script. Met. 11 (1977) 417.

34. M.H. Cohen and D. Turnbull, J. Chem. Phys. 31 (1959) 1164

35. M.I. Cohen, J. Franklin Inst. 283 (1967) 271

36. E.W. Collings, C.E. Mobley, R.E. Maringer and H.L. Gegel, RQM 3, 1978. Pg. 285

37. S.M. Copley, M. Bass, E.W. Van Stryland and O. Esquivel, RQM 3, 1978. Pg. 147.

38. S.M. Copley, D. Beck, O. Esquivel and M. Bass. LSI & LP, 1978, Pg. 161

39. S.D. Dahlgren, RQM 3, 1978. Pg. 36.

40. L.A. Davies, Script. Met. 9 (1975) 431.

41. L.A. Davies, in 'Metallic Glasses' 1978. Ed. J.J. Gilman and H.J. Leamy (ASM, Metals Park, Ohio)

42. L.A. Davies and S.J. Kavesh, J. Mat. Sci. 10 (1975) 453.

43. W.A. Dean and R.E. Spear. Proc. 12th Conf. Army Mat. Research, 1966. Syracause NY. (Syracause University Press) Ed. J. Burke, W.L. Reed and V. Weiss Pg. 268

44. S.J. Donachie and G.S. Ansell, Metall. Trans. A, 6(1975) 1863

45. F. Duflos and B. Cantor, RQM 3, 1978. Pg. 110

46. R.A. Dugdale, Trans. Inst. Met. Finishing 54 (1976) 67

47. P. Duwez, Trans. ASM 60 (1967) 607

48. P. Duwez, Annu. Rev. Mater. Sci. 6(1976) 86

49. P. Duwez and S.C.H. Lin, J. App. Phys. 38 (1967) 4096

50. P. Duwez and R.H. Willens. Trans. Met. Soc. AIME. 227 (1963) 362

51. P. Duwez, R.H. Willens and W. Klement Jr. (1960a) J. App. Phys. 31 (1960) 1136

52. P. Duwez, R.H. Willens and W. Klement, Jr. (1960b) J. App. Phys. 31 (1960) 1137

53. W.A. Elliott, F.P. Gagliano and G. Krauss. Appl. Phys. Lett. 21 (1972) 23.

54. W.A. Elliott, F.P. Gagliano and G. Krauss, Met. Trans. 4 (1973) 2031

55. G. Falkanhagen and W. Hoffmann, Z. Metallkunde, 43 (1952) 69.

56. M.C. Flemings. Proc. Conf. 12th Army Materials Research, 1966, Sycracause, NY. Ed. N.L. Reed and V. Weiss (Syracause University Press) Pg. 235

57. T.G. Fox and P.G. Flory, J. App. Phys. 21 (1950) 581

58. I.P. Gibson, Thin Solid films 83 (1981) 27

59. B.C. Giessen, N.M. Mahadewa, R.J. Murphy and R. Ray, Met. Trans. 8A (1977) 364

59. D.R. Glue, J.A. Sheward, W.J. Young and I.P. Gibson, RARDE Technical Report 1/81

61. D.S. Gnanamuthu, ALMP 1979, Pg.177

62. V.P. Greco, Plating and Surface finishing, March 1981, Pg.56.

63. L.E. Greenwald, United Technologies Research Centre report R75-111321-1 (1975)

64. L.E. Greenwald, United Technologies Research Centre report R77-111321-1 (1977)

65. L.E. Greenwald, E.M. Breinan and B.H. Kear, LSI & LP 1978 Pg.189

66. A.L. Greer, Ph.D. Thesis, University of Cambridge (1979)

67. O.E. Hall, Proc. Phys. Soc. London 64B (1951) 747

68. D.R. Harbur, J.W. Anderson and W.J. Maraman (1966) Report No. LA 3584. Los Alamos Scientific Laboratory. University of California

69. D.R. Harbur, J.W. Anderson and W.J. Maraman. Trans. Met. Soc. of the AIME 245 (1969) 1055

70. G.H. Harth, W.C. Leslie, V.G. Gregson and B.A. Sanders, J. of Met. April 1976, Pg.5.

71. R. Hill, in The Mathematical Theory of Plasticity, Oxford Univ. Press 1967 Pg.213

72. P.B. Hirsch, A. Howie, R.B. Nicholson, D.W. Pashley and M.J. Whelan in 'Electron Microscopy of Thin Crystals' (1965) Butterworth, London.

73. D.W. Hoffmann and J.A. Thornton, Thin Solid films 40 (1977) 355.

74. R.W.K. Honeycombe, RQM 3, 1978 Pg.73

75. R.W.K. Honeycombe in 'Steels' (1981) (Edwin Arnold, London).

76. Y. Inokuti and B. Cantor, Script. Met. 10 (1976) 655

77. Y. Inokuti and B. Cantor, J. Mat. Sci. 12 (1977) 946

78. W.L. Johnson and A.R. Williams, Phys. Rev. B. 20 (1979) 1640

79. H. Jones. Mat. Sci. Eng. 5 (1969) 1

80. G.O. Jones in 'Glass' (1971) (Methuen & Co. Ltd. London)

81. S. Kavesh in 'Metallic Glasses' ASM, Metals Park Ohio (1978) Pg. 36.

82. Y.W. Kim, P.R. Strutt and H. Nowotony, Met. Trans. 10A (1979) 881.

83. W. Klement Jr., J. of Inst. Met. 90 (1961) 1137

84. W. Klement Jr., R.H. Willens and P. Duwez, Nature 187 (1960) 869

85. U. Köster and H.G. Hillenbrand, Proc. Conf. 'Metallic Glasses; Science and Technology', Budapest (1980) Pg.91 Ed. C. Hargitai, I. Bakonyi and T. Kemeny

86. G.V. Kurdjumov and G. Sacchs, Z. Phys. 64 (1930) 325

87. M. Laridjani, P. Ramachandrarao and R.W. Cahn, J. Mat. Sci. 7 (1972) 627

88. N.C. Law, P.R. Howell and D.V. Edmonds, Met. Sci. 13 (1979) 507

89. H.J. Leamy, H.S. Chen and T.T. Wang, Metall. Trans. 3 (1972) 69

90. W.C. Leslie and R.L. Miller, Trans. of ASM 57 (1964) 972

91. B.C. Lewis and H.A. Davies, Proc. Symp. structure of Non-Cryst. Materials, London 1977. Ed. P.H. Gaskell. Pg. 89

92. T. Masumoto and R. Maddin, Acta. Met. 19 (1971) 725

93. T. Masumoto and R. Maddin, Mat. Sci. Eng. 19 (1975) 1

94. H. Matyja, B.C. Giessen and N.J. Grant, J. Inst. Met. 96 (1968) 30

95. J. Mazumdar and W.M. Steen, J. App. Phys. 51 (1980) 941

96. R. McPherson, J. Mat. Sci. 8 (1973) 851

97. R.W. Messler, G.S. Ansell and V.I. Lizunov, Trans. of the ASM, 62 (1969) 362

98. P.A. Molian, Mat. Sci. Eng. 51 (1981) 253

99. R.S. Montgomery, Wear 56 (1979) 155

100. P.G. Moore and L.S. Weinmann in 'Laser Applications in Materials Processing' (1979) SPIE Vol. 198, Bellingham, WA, USA. Pg.120

101. P. Moore, C. Kim and L.S. Weinmann (1979a) ALMP. Pg.259

102. P. Moore, C. Kim and L.S. Weinmann (1979b) LSI & LP. Pg. 221

103. T. Mori, T.Y. Nakajima and T. Sacki, Tesu-to-Hagne 51 (1965) 2031

104. M. Moss, Acta. Met. 16 (1968) 321

105. M. Moss, and D.M. Schuster. Trans. ASM 62 (1969) 201

106. M. Moss, D.L. Smith and R.A. Lefever. App. Phys. Lett 5 (1964) 120.

107. M. Moss and W.I. Young, Powder Met. 7 (1964) 261

108. A. Munitz. Met. Trans B. 11(1980) 563

109. M. Naka, S. Tomizawa, T. Masumoto and T. Watanabe RQM 2. 1975, Pg. 273

110. S.L. Narasimhan, S.M. Copley, E.M. van Stryland and M. Bass Met. Trans. A 10 (1979) 654

111. N.J. Petch. JISI (Lond) 174 (1953) 25

112. P. Pietrokowasky. Rev. Sci. Instr. 34 (1963) 445

113. R.B. Pond, U.S. Patent No. 2976590 (1961)

114. P. Predecki, A.W. Mullendore and N.J. Grant Trans. Met. Soc. AIME 233 (1965) 1581

115. C.M. Preece and C.W. Draper. Wear 67 (1981) 321

116. P.K. Rastogi and P. Duwez, J. Non-Cryst. Sol. 5 (1970) 1

117. R. Ray, R. Hasegawa, C.P. Chou and L.A. Davies Script. Met. 11 (1977) 973

118. R. Ray and L.E. Tanner, Mat. Sci. Eng. 45 (1980) 195

119. D. Rosenthal, Trans. ASME Nov. 1946 Pg. 849

120. A.W. Ruff and L.K. Ives, Wear 75 (1982) 285

121. R.C. Ruhl, Mat. Sci. Eng. 1 (1967) 313

122. R.C. Ruhl and M. Cohen. Trans. Met. Soc. AIME. 245 (1969) 253

123. I.R. Sare and R.W.K. Honeycombe, RQM 2 1975, Pg. 179

124. I.R, Sare and R.W.K. Honeycombe, J. Mat. Sci. 13 (1978) 1991

125. R.S. Sethi, Proc. Conf. on Advances in Surface Coating Technology 1978 (The Weld. Inst. London)

126. S. Shankar, D.E. Koenig and L.E. Darde, J. of Met. Oct. 1981 Pg.13

127. S.A. Snavely and C.L. Faust, Trans. Electrochem. Soc. 97 (1950) 99

128. D.B. Snow and E.M. Breinan, ALMP 1979 Pg. 229

129. W.M. Steen and C. Courtney, Metals Tech. 6 (1979) 456

130. W.M. Steen and C.G.H. Courtney, Metals Tech. 7 (1980)232

131. E.H. Strange and C.A. Pim, U.S. Patent No. 905758, (1908)

132. P.R. Strutt. Mat. Sci. Eng. 44 (1980) 239

133. P.R. Strutt. Mat. Sci. Eng. 49 (1981) 87

134. P.R. Strutt, D.A. Gilbert, H. Nowotony and Y.W. Kim, LSI & LP 1979 Pg. 232

135. A.H. Sully and E.A. Brandes in 'Chromium' 2nd Ed (1967) Pg. 252 (Plenum Press, NY.)

136. D.G. Teer, Proc. Conf. on Advances in Surface Coating Technologies 1978 (The Weld. Inst, London)

137. G. Thomas, Metall. Trans. 2 (1971) 2373

138. G. Thomas, Met. Trans. 9 (1978) 439

139. T.R. Tucker and J.D. Ayers, Met. Trans. A 12 (1981) 1801

140. M. Tuli, P.R. Strutt, H. Nowotony and B.H. Kear, RSP I, 1977. Pg.112

141. D. Turnbull, Contemp. Phys. 10 (1969) 473

142. D.Webster, Trans. ASM 61 (1968) 816

143. L.S. Weinmann, J.N. De Vault and P. Moore, LSI & LP, 1979. Pg.245

144. L.S. Weinmann and C. Kim, RSP I, 1977, Pg. 117.

145. S. Yatsuya and T.B. Massalaski, RQM 4, 1982 Pg. 169

146. K.K. Yee, Int. Met. Rev. 1 (1978) 19

147. H.L. Yeh and R. Maddin Met. Trans. A. 10 (1979) 771

148. J.N. Zemel, Editor, Proc. Int. Conf. on Metallurgical Coatings, San Diego CA 1980.